Simulation of a Ring Imaging Cerenkov Detector to Identify Relativistic Heavy Ions

Manuel Fernández Ordóñez

Marzo 2002

Contents

Introducción **3**

Introduction **7**

Introduction **1**

1 Reaction studies with Relativistic Radioactive Beams **3**
1.1 The R^3B project. 4
1.2 Detectors requirements for the R^3B. 7

2 Primary Interactions of Heavy Ions with Matter **11**
2.1 Energy Losses 12
2.1.1 Simulation Codes 14
2.1.2 Results 17
2.2 Energy Straggling 19
2.2.1 Simulation Codes 20
2.2.2 Results 22
2.3 Angular Straggling 23
2.3.1 Simulation Codes 24
2.3.2 Results 26
2.4 Reactions rates 27

3 Simulation of the Cerenkov detector **31**
3.1 Description of the Vavilov-Cerenkov radiation. 31
3.1.1 Characteristics of the radiation 32
3.2 RICH and HIRICH concepts 33
3.2.1 Radiator materials 34
3.2.2 Theoretical estimations of the β-resolution 34
3.3 Simulation of the Cerenkov detector with GEANT 3.21 40
3.3.1 Description of the Cerenkov detector. 40
3.3.2 Velocity determination from the Cerenkov photon rings. . . . 41
3.3.3 Simulation results for several radiators: liquid C_6F_{14}, solid MgF_2 and solid SiO_2 45

4 Simulation of key experiments and further improvements. 51
4.1 Fission reactions in inverse kinematics 52
4.2 Fragmentation reactions in inverse kinematics. 59
4.2.1 Spallation reaction ^{208}Pb (600 MeV/u) + p 60
4.2.2 Spallation reaction ^{208}Pb (1 GeV/u) + p 61
4.2.3 Spallation reaction ^{56}Fe (600 MeV/u) + p 64
4.2.4 Fragmentation reaction of medium-mass exotic nuclei ^{132}Sn (600 MeV/u) + Pb 66
4.3 Total Internal Reflection Mode 68
4.4 Alternative RICH photon detectors 70

Conclusions 73

A Algorithm for energy-loss calculations used in the code AMADEUS 77

B Energy Losses Tables 81

C Deduction of the geometrical factor Γ. 85

D Simulation of Cerenkov photons with GEANT 3.21 87

E Velocity determination in total internal reflection mode. 89

Bibliography 93

Resumen

" El Agnosticismo no es un credo, sino un método basado en la aplicación de un sólo principio: sigue tu razón donde quiera que te lleve, sin tener en cuenta cualquier otra consideración, sin admitir como cierta cualquier conclusión que no haya sido o no pueda ser demostrada."

Thomas H. Huxley, 1860.

La producción y el estudio de núcleos exóticos ha sido reconocido mundialmente como una novedosa y potente técnica experimental para investigar la naturaleza de la interacción nuclear. Estos son núcleos no estables que nos permiten cubrir un gran rango de isótopos con diferente número de protones y neutrones. Estos núcleos brindan una oportunidad excepcional para estudiar la estructura nuclear lejos de la estabilidad, producir materia nuclear rica en neutrones con una densidad y temperatura altas, así como reproducir en el laboratorio las reacciones nucleares responsables de los procesos de nucleosíntesis estelar. Además, con esta técnica se pueden producir núcleos que presentan modos exóticos de desintegración que pueden ser empleados en la investigación de propiedades fundamentales del modelo standard, o isótopos cuya importancia radica en aplicaciones médicas o industriales.

Recientemente ha sido aprobado un nuevo proyecto europeo denominado R^3B (estudios de reacción con haces radiactivos reslativistas) relacionado con la investigación con núcleos exóticos. Los objetivos de este proyecto son diseñar e implementar parcialmente un dispositivo experimental avanzado para el estudio de núcleos exóticos en el *Gesellschaft für Schwerionenforschung* (GSI) Darmstadt, Alemania. R^3B proporcionará unas condiciones experimentales únicas para realizar investigaciones con haces secundarios para el beneficio de investigadores en los campos de la estructura nuclear, la física de reacciones nucleares, la astrofísica nuclear y la física nuclear aplicada.

El logro técnico de estos experimentos es detectar e identificar completamente en número másico y atómico, así como determinar la energía de todos los productos que

provienen de las reacciones inducidas por núcleos exóticos. Para lograr este objetivo se ha propuesto un complejo sistema de varios detectores. La medida de la pérdida de energía de los productos de reacción por cámaras de ionización permite determinar su número atómico. Además, el empleo de campos magnéticos de gran intensidad permite la determiación de la rigidez magnética de los productos de reacción la cual, conjuntamente con la medida de sus velocidades, permite conocer su número másico.

Uno de los detectores clave de este dispositivo experimental es un detector Cerenkov que será empleado para la medida de las velocidades de los fragmentos provenientes de las reacciones en el blanco. El objetivo de este trabajo es simular un detector Cerenkov de imagen de anillos (RICH) que será implementado en el dispositivo R^3B. Esta simulación será utilizada con el propósito de optimizar el diseño de dicho detector. Para llevar a cabo este proyecto hemos dividido el trabajo en cuatro partes diferenciadas:

- En el primer capítulo se hace un primer acercamiento al projecto R^3B. Se describen el dispositivo experimental y los detectores empleados en él, así como la técnica experimental utilizada para identificación de partículas. Se discute la resolución requerida para los distintos detectores y se justifica la utilización de un RICH para medir las velocidades de los iones bajo estudio.

- En el segundo capítulo se discuten las interacciones primarias de los iones pesados con la materia: pérdidas de energía, dispersión en energía, dispersión angular e interacciones nucleares. Varios códigos standard en el cálculo de estas interacciones serán comparados con el propósito de elegir aquél que proporcione un descripción más cercana a los datos experimentales para ser posteriormente implementado en la simulación. Estos códigos son ATIMA, AMADEUS, GEANT 3.21 y SRIM 2000. De estas comparaciones se concluye que los códigos SRIM 2000 y GEANT 3.21 no están optimizados para calcular la pérdida y dispersión en energía para iones pesados en el rango de energías en el que trabajamos. Sin embargo, GEANT 3.21 es un potente código Monte-Carlo que permite la simulación completa de un determinado dispositivo experimental, efectuando el "tracking" de cualquier partícula a través de él. El interés en el uso de este código está entonces justificado, consecuentemente tendrá que ser modificado con funciones externas para adecuar la precisión en el cálculo de los anteriores parámetros a nuestros requerimientos.

- En el tercer capítulo se discuten las principales características de la radiación de Vavilov-Cerenkov, así como la descripción de la simulación del detector Cerenkov. Se efectuarán sistemáticamente varias simulaciones con el propósito de investigar la resolución en velocidad obtenida para diferentes diseños técnicos del detector teniendo en cuenta diferentes radiadores, espesores del mismo, la granularidad del detector de fotones...buscando siempre una resolución en

velocidad adecuada y tratando de minimizar las interacciones atómicas y nucleares de los iones en el Cerenkov, las cuales influirán negativamente en la posterior identifiación de éstos. Estos estudios sistemáticos fueron realizados para los siguientes radiadores: radiador líquido de C_6F_14, radiador sólido de MgF_2 y radiador sólido de SiO_2. Se observará que la resolución en velocidad mejora a medida que aumenta la carga del núcleo que atraviesa el radiador debido al mayor número de fotones generados, sin embargo, a partir de la carga 25-30 el papel de la pérdida de energía en el radiador toma importancia y compensa la generación de fotones, manteniéndose la resolución en un valor casi constante. La resolución en velocidad también mejorará al aumentar la energía cinética del núcleo incidente debido a dos factores, en primer lugar al aumento en el número de fotones generados y, segundo, a la menor pérdida de energía. También fue estudiada la variación de la resolución en velocidad con los cambios en el espesor del radiador, se verá que, al aumentar el radiador, la resolución disminuye, demostrando que el efecto de la pérdida de energía domina a la generación de fotones. Por último la variación de la resolución en velocidad como función de la granularidad del detector será también estudiada, demostrando que dicha granularidad no es un factor determinante en la resolución en velocidad.

- El cuarto capítulo se concentra en la simulación de varios experimentos con el propósito de elegir el mejor diseño del detector para el estudio de cada uno de ellos. Se estudiarán varios casos representativos como son: la fisión del $^{238}U + Pb$ a 600 MeV/u, las espalaciones del $^{56}Fe + p$ a 600 MeV/u y del $^{208}Pb + p$ a 1 GeV/u, así como la fragmentación del $^{132}Sn + Pb$ a 600 MeV/u.

  En el caso de la fisión se obtendrán señales con dos anillos en el detector de fotones debido a la emisión simulatánea de ambos fragmentos de fisión. Se discutirá el proceso mediante el cual se obtiene el radio de ambos anillos a partir de esas señales. Del estudio de las interacciones primarias de varios residuos típicos de la fisión con los materiales que componen el detector Cerenkov, junto con el estudio de los diferentes rangos en energía cubiertos por cada uno de los radiadores se propondrá el radiador para el estudio de estos experimentos. Finalmente se propuso un radiador sólido de SiO_2 de 2 mm de espesor para el estudio de reacciones de fisión. Posteriormente a la elección del radiador se estudiará como influye la materia que constituye el detector Cerenkov en la resolución de la medida de la energía cinética para los distintos residuos de fisión. Se verá que el papel más importante en dicha resolución lo juega la dispersión angular en el blanco de plomo, con lo cual la elección del radiador no es determinante para esas medidas.

  En los sucesos de espalación se han simulado los mismos aspectos que en el caso de la fisión. La elección del radiador se ha hecho teniendo en cuenta los mismos argumentos que en aquél. En estos casos las propuestas han sido un radiador sólido de SiO_2 de 5 mm de espesor para el caso de la fragmentación

del ^{56}Fe y de 2 mm de espesor en el caso de la espalación del ^{208}Pb a bajas energías (inferiores a 750 MeV/u). En el caso de energías superiores se verá que el SiO_2 no puede ser empleado debido a efectos de reflexion total interna, si bien se discutirá un nuevo modo de operación de los radiadores basado en ese efecto. En el caso de la espalación a alta energía del ^{208}Pb se propondrá utilizar un radiador sólido de 2 mm de espesor de MgF_2 o bien 2 mm de SiO_2 pero trabajando en el modo de reflexion total interna. Posteriormente a la elección del radiador se estudiará, como en el caso de la fisión, la influencia de la materia que compone el detector Cerenkov en la resolución de la medida de la energía cinética. En este caso se demostrará que las resolusiones en dichas medidas vienen principalmente determinadas por la dispersión en velocidad que los residuos de espalación sufren en el radiador del detector.

En el caso de la fragmentación del ^{132}Sn el radiador propuesto fueron 3 mm de espesor de SiO_2. Este espesor fue elegido con el propósito de obtener una buena resolución en velocidad incluso para los fragmentos más ligeros. Como en los casos anteriores, la incertidumbre en la medida de la energía cinética debida a la materia que forma parte del detector Cerenkov fue estudiada. En este caso la mayor influencia en esta incertidumbre viene dada por la dispersión en velocidad sufrida por los fragmentos en el blanco de plomo, con lo cual, la elección del radiador no es determinante para la medida de la energía cinética.

Finalizaremos este trabajo con una discusión sobre la implementación de detectores de fotones de reciente desarrollo con el fin de aumentar la eficiencia cuántica de dicho detector y mejorar así la resolución en velocidad obtenida con el RICH.

Introduction

" It is better for a man to be lacking in wisdom and to have no understanding of science but to be fearful of God, than to have much understanding but transgress the Law of the Almighty."

Eclesiástico, XIX-21.

The production and study of exotic nuclei has been recognized worldwide as a novel and powerful experimental technique to investigate the nature of the nuclear interaction. This technique allows to produce nuclei with widely varying proton-to-neutron ratios, which cannot be found in nature. These nuclei give us a unique oportunity to investigate nuclear structure far from stability, to produce hot and dense neutron rich nuclear matter or to reproduce in the laboratory the nuclear reactions responsible of the stelar nuclesynthesis processes. In addition we can produce nuclei which present exotic desintegration modes that can be used to investigate fundamental properties of the standard model, or nuclei which have importance because of their applications in medicine or industry.

Recently was aproved a new project called R^3B (Reaction studies with Relativistic Radioactive ion Beams) related to the investigations with exotic nuclei. The aim of this project is to design and partly implement an advanced experimental facility for studies with exotic nuclei at the *Gesellschaft für Schwerionenforschung* laboratory (GSI) in Darmstadt, Germany. R3B will provide unique experimental conditions worldwide for experiments with relativistic secondary beams to the benefit of researchers in the fields of nuclear structure, nuclear reactions physics, nuclear astrophysics and applied nuclear physics.

The technical challenge of this facility is to detect and fully identify in atomic and mass number and to determine the energies of all the products outcoming from reactions induced by exotic nuclei. To achieve this goal a complex system of different detectors has been proposed. The measurement of the energy loss of the reaction products by ionization chambers allows to determine their atomic number. In addition, the use of strong magnetic fields allows the determination of the mag-

netic rigidities of the reaction products that, together with a measurement of their velocity, will provide their mass number.

One of the key detectors of this setup is a Cerenkov detector which will be used to measure the velocity of the fragments outcoming the target. The goal of this work is to simulate a Ring Imaging Cerenkov Detector to be implement into the R^3B experimental setup. This simulation will be used to optimize the design of such a detector. In order to simulate and optimize this detector we will divide the work into four different chapters:

- In the first chapter, an overview to the R^3B project is presented, the experimental setup and the detectors are described, as well as the experimental technique used for particle identification.
- In the second chapter, we discuss the primary interactions of heavy ions with matter: energy-loss, energy straggling, angular straggling and nuclear interactions. Some standard computational codes in this field will be compared and, in addition to the theoretical descriptions, several simulations will be made with these codes in order to chose the "closest to the reality" description to be incorporated in our simulation.
- In the third chapter, we present the basic priciples of Vavilov-Cerenkov radiation, as well as the description of the simulated Cerenkov detector. Several simulations will be systematically made in order to investigate the velocity resolution obtained for different designs of the detector considering different radiators, thicknesses, photon detector resolution, etc.
- In the fourth chapter, some key experiments are simulated in order to define the optimum design of the detector for any of them. The effect of total internal reflexion is applied to the radiators and, then, a new photon detection operation mode will be described. In addition, further improvements on the photon detector are discussed whithin the frame of the implementation of new photon detectors recently developed.

Introduction

" It is better for a man to be lacking in wisdom and to have no understanding of science but to be fearful of God, than to have much understanding but transgress the Law of the Almighty."

Eclesiástico, XIX-21.

The production and study of exotic nuclei has been recognized worldwide as a novel and powerful experimental technique to investigate the nature of the nuclear interaction. This technique allows to produce nuclei with widely varying proton-to-neutron ratios, which cannot be found in nature. These nuclei give us a unique oportunity to investigate nuclear structure far from stability, to produce hot and dense neutron rich nuclear matter or to reproduce in the laboratory the nuclear reactions responsible of the stelar nuclesynthesis processes. In addition we can produce nuclei which present exotic desintegration modes that can be used to investigate fundamental properties of the standard model, or nuclei which have importance because of their applications in medicine or industry.

Recently was aproved a new project called R^3B (Reaction studies with Relativistic Radioactive ion Beams) related to the investigations with exotic nuclei. The aim of this project is to design and partly implement an advanced experimental facility for studies with exotic nuclei at the *Gesellschaft für Schwerionenforschung* laboratory (GSI) in Darmstadt, Germany. R3B will provide unique experimental conditions worldwide for experiments with relativistic secondary beams to the benefit of researchers in the fields of nuclear structure, nuclear reactions physics, nuclear astrophysics and applied nuclear physics.

The technical challenge of this facility is to detect and fully identify in atomic and mass number and to determine the energies of all the products outcoming from reactions induced by exotic nuclei. To achieve this goal a complex system of different detectors has been proposed. The measurement of the energy loss of the reaction products by ionization chambers allows to determine their atomic number. In addition, the use of strong magnetic fields allows the determination of the mag-

netic rigidities of the reaction products that, together with a measurement of their velocity, will provide their mass number.

One of the key detectors of this setup is a Cerenkov detector which will be used to measure the velocity of the fragments outcoming the target. The goal of this work is to simulate a Ring Imaging Cerenkov Detector to be implement into the R^3B experimental setup. This simulation will be used to optimize the design of such a detector. In order to simulate and optimize this detector we will divide the work into four different chapters:

- In the first chapter, an overview to the R^3B project is presented, the experimental setup and the detectors are described, as well as the experimental technique used for particle identification.
- In the second chapter, we discuss the primary interactions of heavy ions with matter: energy-loss, energy straggling, angular straggling and nuclear interactions. Some standard computational codes in this field will be compared and, in addition to the theoretical descriptions, several simulations will be made with these codes in order to chose the "closest to the reality" description to be incorporated in our simulation.
- In the third chapter, we present the basic priciples of Vavilov-Cerenkov radiation, as well as the description of the simulated Cerenkov detector. Several simulations will be systematically made in order to investigate the velocity resolution obtained for different designs of the detector considering different radiators, thicknesses, photon detector resolution, etc.
- In the fourth chapter, some key experiments are simulated in order to define the optimum design of the detector for any of them. The effect of total internal reflexion is applied to the radiators and, then, a new photon detection operation mode will be described. In addition, further improvements on the photon detector are discussed whithin the frame of the implementation of new photon detectors recently developed.

Chapter 1

Reaction studies with Relativistic Radioactive Beams

" Agnosticism is not a creed but rather a method based on applying on sole principle: follow your reason wherever it takes you, giving in to no other consideration, admiting no conclusion as correct that has not or cannot be demonstrated."

Thomas H. Huxley, 1860.

The importance of the Physics made with energetic beams of exotic nuclei has been recognized worldwide and presents an important challenge for nuclear physics. New nuclear phenomena have been observed and then, the nuclear models have to be radically improved in order to explain these new phenomena. For this goal nuclei far from beta stability are thought to play a decisive role. The secondary beam technique (consisting on accelerate radioactive nuclei previously created in another reaction) allows to produce nuclei with widely varying proton-to-neutron ratios, which cannot be found in nature. The isotopes created with this method can be studied in several ways: they could be stopped and studied with spectroscopy methods, alternatively, they can undergo high-energy nuclear reactions in a secondary target. The nuclear structure and reaction dynamics can thus be explored and the results of these studies could be be used in other fields than nuclear physics. The main guidelines behind studies of exotic nuclei with high-energy reactions are:

- Halos: This effect appears when approaching to the neutron drip line. It has been observed for ^{11}Li, ^{11}Be, ^{14}Be, ^{17}B and ^{19}C.
- Skins: For a large neutron excess, the bulk of the neutron density is predicted to extend beyond the proton density creating a sort of "neutron skin". This

could be helpful for understanding the properties of neutron stars.

- Vanishing of shell closures: Theory end experiment are now indicating that shell closures may change far from stability. A well-known example is the disappearance of N=20 as a neutron magic number in Neon, Magnesium and Sodium isotopes.

- To provide solid nuclear structure input for astrophysical purposes or other applications, either directly by measurements or, indirectly, by the improvement of theoretical concepts on the basis of accumulated experimental information.

- To measure production cross sections in fission or fragmentation reactions relevant in technical applications like the constructions of accelerator-driven fission reactors or the incineration of nuclear waste.

Major breakthroughs on these topics require detailed nuclear reaction studies and optimized experimental conditions. This requires high-quality secondary radioactive beams together with the most advanced experimental equipment.

1.1 The R^3B project.

The objectives of the R^3B project are to design and partly implement an advanced experimental setup for Reaction studies with Relativistic Radioactive ion Beams (R^3B). The experiments will take place in the cave B at the *Gesellschaft für Schwerionenforschung* laboratory (GSI) in Darmstadt, Germany (see fig.1.1). R^3B will provide unique experimental conditions worldwide for experiments with relativistic secondary beams to the benefit of researchers in the fields of applied nuclear physics, nuclear reaction physics and nuclear astrophysics.

The R^3B experimental setup is described in the following with the help of figure 1.2. For a complete kinematic measurement, every particle out-coming from the reaction has to be identified in mass, charge and, in addition, its momentum has to be measured. The R^3B proposal includes the measurement of the emitted γ rays with a NaI detector covering a 4π geometry around the secondary target. Neutrons will be detected with the Large Area Neutron Detector (LAND). For the charged particles, the measurement of the magnetic rigidity, $B\rho$, together with the velocity, β, allow the identification of the particle, according to:

$$B\rho[Tm] = 3.107 \cdot \frac{A}{q}\gamma\beta \tag{1.1}$$

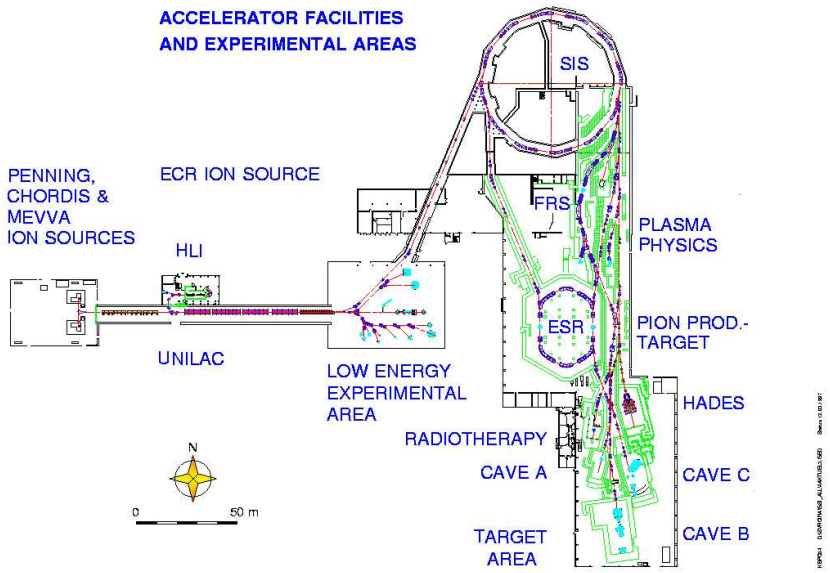

Figure 1.1: *Gesellschaft für Schwerionenforschung (GSI) facilities at Darmstadt (Germany). The R^3B project experiments will take place in the Cave B (down-right in the picture).*

where $B\rho$ is the magnetic rigidity, A is the nuclei mass number, q is the atomic charge, γ is the Lorentz factor and β is the nuclei velocity. For the measurement of the $B\rho$ a large acceptance dipole and three position detectors are needed. For the measurement of the particle velocities several methods as a Time-of-Flight (ToF) or a Ring Imaging Cerenkov (RICH) detector could be used. From equation 1.1 once measured $B\rho$ and β, the ratio A/q can be determined. With a later measurement of the nuclei charge z effectuated with the Multi-Sample Ionization Chamber (MUSIC), and assuming that the ions are bare, the mass can be unambiguously determined.

One of the important topics to be studied is the reaction mechanism. For this achievement the excitation energy, $E^\star$, of the nuclei before undergoing any reaction has to be known precisely. This information can be obtained from the measurement of all the masses and energies of the particles produced in the reaction according to expression 1.2:

$$E^\star = \sum_i m_i + \sum_i T_i + \sum_i \gamma_i - m_A \tag{1.2}$$

where $E^\star$ is the projectile-like residue excitation energy, m_A is the projectile-like resiude mass, T_i and m_i are the kinetic energy and mass, respectively, of all the

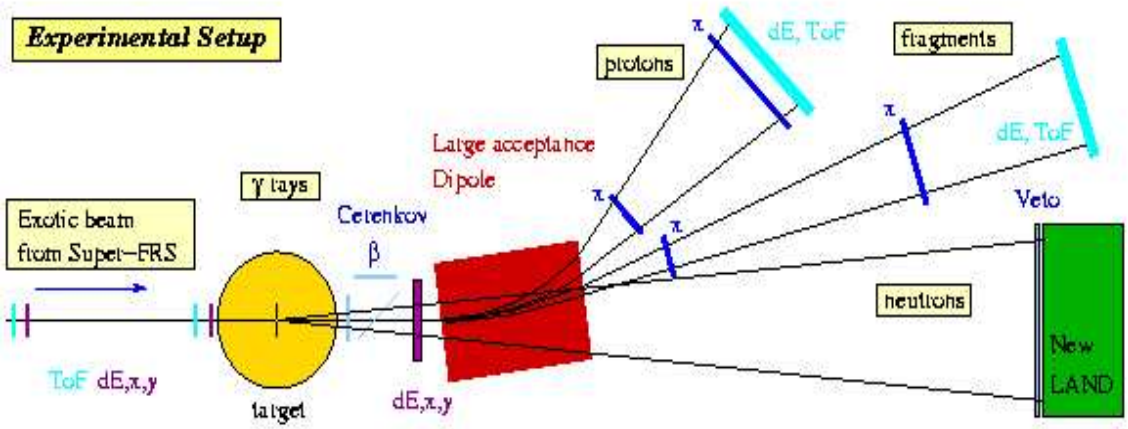

Figure 1.2: *Schematic picture of the R^B experimental setup at cave B (see figure 1.1). From left to right we can observe the secondary target, the photon detector, the Ring Imaging Cerenkov Detector (RICH), a position detector, the large acceptance supra-conductor dipole, another position detector, the last position detector, the Large Area Neutron Detector (LAND) and a ToF for light particle identification.*

particles after the reaction (fragments, evaporated protons, neutrons, etc) and γ_i is the energy of the photons emitted by the excited projectile. We will describe in the following the detectors used in this setup:

- **γ-rays Detector:** This detector could be either a ball with 160 NaI detectors arranged in a 4π geometry or a compact CsI detector with 144 segments in the forward direction.
- **Dipole Magnet:** Two important characteristics are required for the magnet: high bending power and large acceptance. The first one is required in order to separate two heavy neighboring nuclei according to the expression 1.1 and the second one is needed in order to identify any particle produced in the reaction. To fulfill this goal a supra-conductor dipole is under design. The field integral of this dipole will be 4.8 Tm with a bending angle of 18 degrees for a rigidity of 15 Tm and a geometrical acceptance of $\pm$ 80 mrad in vertical and horizontal directions. The dipole magnet will be filled with He to minimize the angular straggling of the ions.
- **Position Detectors:** Three position detectors are needed in order to reconstruct the track of the particle to determine the bending angle in the dipole. One of these detectors will be situated in front of the dipole, and the two others behind the dipole. These detectors will provide a position resolution of 200 μm.

- **MUSIC Detector:** The Multi Sample Ionization Chamber is used to identify the charge of the particles passing through it according to the Z^2 dependence on their energy loss. The charge is measured with an accuracy of 0.30 charge units for charges below Z=80. This chamber could also be used as a horizontal position detector based on a drift time measurement with an accuracy of 2 mm [1].
- **LAND Detector:** The large area neutron detector was designed for the detection of high energy neutrons. This detector must allow to resolve multiple hits. The energy resolution of the neutron kinetic energy is about 5% and the detection efficiency at 1 GeV is close to 100% [2].
- **RICH Detector:** This detector is used to measure the ion velocities rather than a ToF, the justification will be given in the next section.

1.2 Detectors requirements for the R^3B.

As we mentioned, to perform studies based on complete kinematic measurements, all the particles generated in the reaction have to be identified in charge, mass and momentum. In this section we will describe the requirements of the different detectors used in this experimental setup to achieve this aim.

In order to identify the charge of the particles, a resolution $\frac{\Delta Z}{Z} \approx 0.5$ is needed. This accuracy is fairly given by the Multi Sample Ionization Chamber (MUSIC), which provides an accuracy in the charge determination of 0.3 charge units for nuclei below Z=80..

In order to identify the mass of the particles and to separate two neighboring nuclei, a resolution $\frac{\Delta(A/q)}{(A/q)} \approx \frac{0.5}{170}$ is needed. From equation 1.1 we obtain:

$$\left(\frac{\Delta(A/q)}{(A/q)}\right)^2 = \left(\frac{\Delta(B\rho)}{B\rho}\right)^2 + \frac{1}{(1-\beta^2)^2} \cdot \left(\frac{\Delta\beta}{\beta}\right)^2 \tag{1.3}$$

The factor $\Delta(B\rho)/B\rho$ is given by the accuracy in the measurement of the bending angle (given by the accuracy of the position detectors) and the dipole bending power. In order to achieve the required accuracy in the mass identification, a velocity resolution $\Delta\beta/\beta \sim 10^{-3}$ and a position resolution of 200 μm are required.

The dipole was chosen to provide a bending angle of 18 degrees for a magnetic rigidity of 15 T·m. Taking the resolution of the position detectors as 200 μm we can

estimate the uncertainty in the measurement of the bending angle, and from these the accuracy of the measurement of the $B\rho$ introduced by the angular straggling in the detectors, in the gas of the MUSIC and by the distance between the detectors as follows:

$$\Delta\theta = \frac{\sqrt{\Delta x_1^2 + \Delta x_2'^2 + \Delta x_3'^2}}{l} \tag{1.4}$$

where l is the distance between the position detectors, $\Delta x_2'$ takes into account the position resolution of the second detector, the angular straggling in the first position detector and the angular straggling in the helium atmosphere inside the dipole, $\Delta x_3'$ takes into account the position resolution in the third detector, the angular straggling suffered by the particle in the second detector and in the gas inside the MUSIC. The angular straggling in the position detectors is taken to be 0.19 mrad and the angular straggling in the MUSIC 0.38 mrad. The angular straggling inside the dipole can be neglected. A position resolution of 200 μm and a distance between the detectors l=1.2 m is taken. We conclude that the uncertainty in the measurement of the $B\rho$ of the particle is given by:

$$\Delta\theta = 0.67 \qquad mrad \tag{1.5}$$

With these results we can estimate the required velocity resolution in order to separate the nuclei $^{238}U_{92}$ at 600 MeV/u ($B\rho$=10.5 T·m) from its neighbor $^{239}U_{92}$. The bending angle within the dipole will be $\theta \approx 450$ mrad. This gives a $\Delta(B\rho)/B\rho$ of 1.5×10^{-3}. From expression 1.3 we need a velocity accuracy of $\Delta\beta/\beta = 1.3\times10^{-3}$. Consequently, in order to provide a good mass separation for reaction research with relativistic heavy ions, the R^3B setup should provide a velocity resolution around $\Delta\beta/\beta \sim 10^{-3}$

This resolution cannot be achieved with a ToF system due to the limited space in the cave B. The uncertainty of a ToF measurement is given by:

$$\left(\frac{\Delta(ToF)}{ToF}\right)^2 = \left(\frac{\Delta L}{L}\right)^2 + \left(\frac{\Delta\beta}{\beta}\right)^2 \tag{1.6}$$

Where a typical value for $\Delta(ToF)$ can be taken as 150 ps, L is the ToF distance and β is the nuclei velocity. According to this expression, a simple estimation of the dimensions for a ToF system can be made. If we take a fissioning nuclei flying at 1 GeV/u the flight path needed to obtain a velocity resolution of 10^{-3} for heavy

fragments is about 40 m. Additionally, the maximum emerging angle for a fission fragment is about 30-40 mrads, this means that we would need a stop detector with a surface of 3.5x3.5 m^2. A promising alternative is the use of a RICH detector. The advantages of using a Cerenkov detector are that it provides the required velocity precision and a large acceptance as compared with the required dimensions for a stop detector of ToF system. The disadvantage is that a considerable amount of matter is placed in the beam line, this would make that the atomic interactions of the particles with matter would influence their later identifications. The Cerenkov detector will be used for the identification of heavy ions created in fission and fragmentation reactions, for light ions techniques as ToF could be used for their identification

The optimization of the design of the Cerenkov detector justifies the present work where we performed a detailed simulation of such detector.

Chapter 2

Primary Interactions of Heavy Ions with Matter

The velocity measurements made with a RICH detector are affected by the primary interactions of heavy ions in matter, i.e. energy-loss, energy loss straggling and angular straggling. Simultaneously, these interactions will affect the later ion identification due to changes that the detector induces in the particle velocity and trajectory. For these reasons, accurated descriptions of these interactions have to be implemented in the simulation codes. This chapter will be dedicated to the comparison of different codes commonly used to describe these interactions in order to choose the best option for our simulation work. These codes are:

- GEANT 3.21 [3] code is able to simulate the dominant processes governing the interaction of particle and ions with matter in the energy range from 10 keV to 10 TeV. It is a Monte-Carlo code able to simulate a complete experimental setup with all the detectors and follow the particle tracking within it.

- ATIMA [4] code, developed at GSI, Darmstadt, calculates heavy-ion interactions with matter for kinetic energies ranging from 1 keV/u to 500 GeV/u. This code follows closely the Lindhard and Sørensen (LS) theory that take into account the deviation from the first order quantum perturbation theory of the different expressions used to analize the primary interaction within matter.

- SRIM 2000 [5] code is described in 'The Stopping and Range of Ions in Solids' [6]. It is a package of programs which calculates the stopping power and range of ions (10 eV - 2 GeV) into matter using a quantum-mechanical treatment of ion-atom collision.

- AMADEUS [7] code also allows to simulate the interaction of heavy-ions with matter for kinetic energies in the range between 100 MeV/u and 2 GeV/u. This code has an analytical formulation.

In this chapter we will introduce the main interactions of heavy-ions with matter: energy loss, energy straggling and angular straggling and nuclear and electromagnetic interactions. The comparison of the different existing codes to estimate these interactions with experimental data will allow to choose the optimum models to be used in our simulations of the Cerenkoc detector.

2.1 Energy Losses

Many of the finest physicists of this century have occupied their thoughts in various aspects of the penetration of charged particles in matter, like Thomson, Rutherford, Bohr, Bethe, Mott, Bloch, Fermi, Landau, etc. Many review articles have been written on this subject being based on either semi-classical or first-order quantum-mechanical approaches, see for example [8].

Bloch bridged the gap between the quantum approach and the classical one developed by Bethe and Bohr, respectively, few years before. This lead to the well known Bethe-Bloch expression for the stopping power of heavy particles:

$$S = \frac{4\pi N Z^2 e^4}{m\beta^2 c^2}\left(ln\frac{2m\beta^2c^2}{I} - ln(1-\beta^2) - \beta^2\right) \tag{2.1}$$

where N is the number of electrons per volume unit, Z and m are the charge and mass of the projectile, respectively, and I is the mean ionization potencial of the target.

Recently, danish physicists Linhard and Sørensen developed a new theory [9] of the sttoping power for relativistic heavy ions. The achievement of this theory is the calculation of the deviation of the precise theory from first-order quantum perturbation. The size of the nuclei is also taken into account.

In order to know precisely the stopping power for heavy ions, the familiar Bethe expression 2.1 [10] [11] becomes invalid when dealing with particles of high atomic charge because of the failure on the first Born approximation. Ahlen [8] [12] presented a formalism that takes into account additional terms in the energy loss expression that become important when the charge of the projectile increases. In

particular he introduced terms to account for the exact Mott cross section for scattering, and for the electron binding energy during close collisions, Bloch scattering and relativistic Bloch scattering. He shosed that these terms he showed could be described as a series of terms of higher power of the charge of the projectile. Following Ahlen we can rewrite the energy loss as:

$$-\frac{dE}{dx} = \frac{4\pi N e^4}{mc^2}\frac{Z_{pe}^2}{\beta^2}\left[ln\left(\frac{2mc^2}{I}\frac{\beta^2}{(1-\beta^2)}\right) - \beta^2 - S - D - M - B\right] \tag{2.2}$$

where N is the number of atoms per unit volume in the medium with mean atomic number Z_m and mean ionization potential I, β is the projectile velocity and Z_{pe} differs from the true atomic number of the projectile Z_p due to the effects of electron pickup and stripping. There are few expressions to estimate Z_{pe}[1], for example the semiempirical one derived by Pierce and Blann [13] :

$$Z_{pe} = Z_p\left[1 - exp\left(\frac{-130\beta}{Z_p^{2/3}}\right)\right] \tag{2.3}$$

This expression has been found to be a reasonable fit to a wide range of experimental results. The corrections that appear in the equation 2.2 are:

- **S** is the correction for shell effects introduced by Barkas and Berger [14]. It takes into account that at projectile velocities comparable or even smaller than the orbital velocities of the bound target electrons the energy transfer is less effective. This contribution decreases with $1/\beta^2$ and thus, for relativistic ions even the contribution to the stopping power from the interaction with the target K-shell electrons is affected very little and shell corrections can safely be ignored.

- **D** is the relativistic density correction introduced by Fermi [15]. If the target medium is not a dilute gas but the density of atoms is high, the projectile charge is screened by dielectric polarization of the medium and the energy transfer in large impact parameter collisions is less effective. This contribution is not significant to the stopping power calculation if $\beta \leq 0.88$.

[1] The problem of charge-states of a heavy ione passing through matter is a difficult one without solution yet. Several expressions of different sofistication levels exist. This one derived by Pierce and Blann is used by the codes we are going to analize.

- **M** is the correction for Mott scattering. For the expression 2.1 first-order Born approximation was used. However, for large nuclear charges the scattering cross section in Born approximation differs significantly from the exact cross section. An exact solution of the Dirac equation for the scattering of a relativistic electron in the central field of a point nucleus was first given by Mott [16][17].

- **B** is a correction derived by Bloch[18] for the electron binding during close collisions. He showed that independent of the magnitude of the projectil charge, a first-order perturbation treatment is sufficient for the distant collisions. However, he noticed that for small impact parameter collisions the exact scattering amplitudes for a Coulomb field must be used rather than those of the Born approximation

In 1994 C.Scheidenberger et al.[19] measured for the first time direct stopping powers with high precission, demonstrating the importance of the Bloch and Mott higher-order-correction terms to the relativistic Bethe formula for heavy ions.

2.1.1 Simulation Codes

Motivated by the need of precise energy-loss predictions several computer codes to calculate de energy loss of high-energetic heavy ions are tested.

- **GEANT 3.21** This code evaluates the stopping power by cuadratic interpolation of tabulated stopping powers of protons in different materials. In the case of heavy-ions a scaling law is applied. Then the mean energy lost of a charged particle in a given material is calculated as follows:

$$\Delta E = \frac{dE}{dx} \times s \tag{2.4}$$

  where s is the step size within the layer of matter and it is calculated automatically by the code taking into account different properties of the material as density, atomic number, mass, etc.

  The used ionization potential values (I in expression 2.1) are given in ref. [20]. Then, the calculation of the energy loss is done in the following steps:

  1. - Evaluate the stopping range for the threshold energy, only once at the beginning of each new particle tracking. The stopping range is calculated

with the following expression

$$R = -\int_0^{E_0} \frac{dx}{dE} dE \tag{2.5}$$

2. - From the energy of the particle derive the stopping range by a quadratic interpolation of the range table as follows

$$R_0 = -B_I + \frac{A_I}{\mid A_I \mid}\sqrt{B_I^2 - \left(C_I - \frac{E_0}{A_I}\right)} \tag{2.6}$$

where A_I, B_I and C_I are constants for the quadratic interpolation.

3. - Evaluate the stopping range for the particle after a given step: $R_0' = R_0 - s$. If this is smaller than the stopping range of the particle of threshold energy, the tracking is stopped because it is below the energy cut. Otherwise, the final energy is computed as

$$E_0' = A_I(C_I + R_0'(2B_I + R_0')) \tag{2.7}$$

4. - The energy loss is computed as

$$\Delta E = E_0 - E_0' \tag{2.8}$$

GEANT takes into account also the charge-states of the projectile passing through matter. The code has implemented the Pierce and Blann equation 2.3 and the probability of pickup and loss of electrons is computed on each step.

- **ATIMA** is a code based on theoretical evaluations. It computes energy losses following closely the Linhard and Sørensen theory which takes into account higher orders in quantum perturbation theory. The Dirac, Mott, Bloch and Relativistic Bloch correctios given in expresion 2.2 are also taken. The only experimental data used in the code are the mean ionitation potentials (I in expression 2.1).

  For each calculation the code fills some tables with the energy-loss values for all the possible projectile-target combinations. When the user wants to compute a particular value for the energy loss, ATIMA makes an interpolation within the tabulated data. The the charge-states in ATIMA are treated using the Pierce and Blann expression (eq. 2.3).

- **SRIM 2000** consistis of a package of programs to calculate the stopping powers and ranges of ions in matter in an energy range between 10 eV and 2 GeV using a quantum-mechanical treatment of the ion-atom collision. The code uses statistical algorithms which allow the ion to jump between calculated

collisions and then to average the collision results over the considered interval. During the collisions, the ion and the target atoms interact by screened Coulomb collision, including exchange and correlations interactions between the overlaping electron shells. It computes the energy losses using tables which were originally derived in 1984 using this methods described in [6]. These values were completely revised and improved in 1988, and again in 1995. Due to the comercial character of this code is difficult to find more information about the way to compute the physical quantities.

- The code **AMADEUS** is based on a semiempirical algorithm to evaluate energy losses in thick layers following a fast and efficient procedure described in Appendix A. The basic idea is to parameterised the range of ions in any material by using an analytical function that can be inverted. Then, the energy loss in a layer of matter with thickness x can be obtained as

$$\Delta E(x) = E_i - E_f \tag{2.9}$$

where E_i is the initial energy of the ion and E_f is the remaining energy of the ion after traversing the layer of matter that can easily be calculated from the residual ranges before and behind the layer, $r(E_i)$ and $r(E_f)$, since

$$r(E_f) = r(E_i) - x \tag{2.10}$$

and the function $r(E)$ can be inverted.

To determine the function $r(E)$ the range of a number of different projectile-stopper combinations by numerical integration of the stopping-power expressions presented in the appendix of [21] was calculated. Then the values were fit with the least-squares method, in an energy range between 100 A MeV and 2 A GeV, to the function

$$r(Z_p, A_p, E/A_p) = k\frac{A_p}{Z_p^2}10^{\kappa} \qquad mg/cm^2 \tag{2.11}$$

with A_p and Z_p the mass and atomic number of the ion, respectively and E/A_p its energy in A MeV. The parameter κ is polinomial and logarithm combination of different powers in Z_p and E/A_p (see Appendix A).

The expression 2.11 can be inverted to get the energy as a function of the residual range of the ion, that is $E(Z_p, A_p, r)$. Using this method, AMADEUS code computes energy losses in one step and it does not need to integrate any stopping power expression. The computing time is then shorter than in other codes.

2.1.2 Results

In this section we compare the results obtained using these codes with a set of available experimental measurements on energy losses [22], which are shown in Appendix B. The same projectile-target combinations were simulated with all the codes under study in order to compare the results. The whole data collection is also printed in Appendix B

From this comparison we can deduce that ATIMA seems to provide a better description of the experimental data. AMADEUS provides also a description of the experimental data within a few percent accuracy. However, this good agreement does not exist in the cases of GEANT 3.21 and SRIM 2000, at least, for heavy projectiles. For light projectiles the predictions of both codes are in quite good agreement with the measured data. In contrast, for mass numbers beyond A=86 the relative differences are systematically larger than the experimental errors. This behaviour is specially notable in the uranium region, where the relative differences are close to 10% and even larger when we consider heavy target materials.

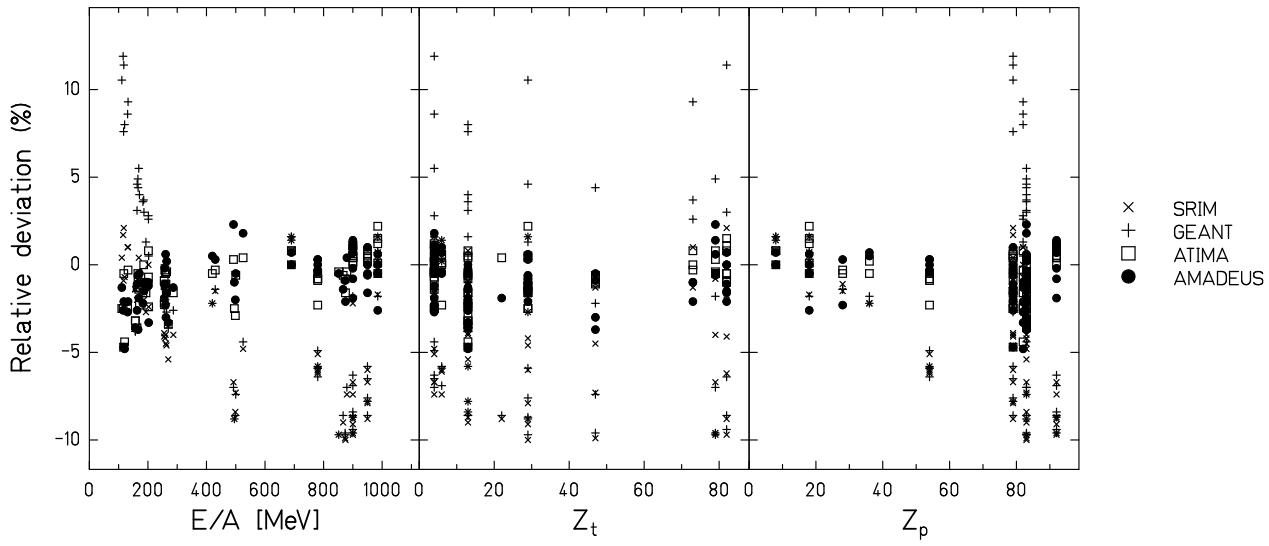

Figure 2.1: *Relative deviations (see text below) of the different model descriptions from the measured energy-loss values as a function of energy E, target element Z_t and projectile element Z_p.*

To quantify the predictive power of the different codes we have used the sum of quadratic deviations, normalised by the number of data points as given by the following expresion:

$$M = \frac{\sum \left(\frac{E^i_{data} - E^i_{sim}}{Err^i_{data}}\right)^2}{n} \tag{2.12}$$

where E_{data} and E_{sim} represent the measured and simulated energy losses, respectively, and Err_{data} is the uncertainty of the measured energy losses, n represents the number of experimental measurements considered to evaluate M.

The results were M=3.5 for ATIMA, M=4.2 for AMADEUS, M=57.6 for GEANT 3.21 and M=48.7 for SRIM 2000. As already mentioned, the best agreement to the data is obtained with the code ATIMA. AMADEUS provides very similar results. However, the predictions of GEANT 3.21 and SRIM 2000 are quite far from an overall good description of the measured energy losses. Consequently, we can conclude that these two codes are not suitable to compute energy losses of high-energetic heavy ions with the accuracy needed to our intentions.

The deviations of the model descriptions from the experimental data can be analysed in more detail on the basis of the graphical presentation as a function of the energy, target and projectile shown in figure 2.1. The deviation of the values given by the codes from the experimental values are shown in the figure. This deviation is given in relative values, corresponding to the difference between the two values and divided by the experimental one. Looking at this figure, a clear tendency of GEANT 3.21(vertical crosses) to overpredict the energy loss of heavy ions at energies below 200 A MeV is observed. Moreover, the values for energies above 400 A MeV are underpredicted by both, GEANT 3.21 and SRIM 2000(diagonal crosses). These deviations seem predominantly to occur for the most heavy projectiles. It is also important to note that the deviations of ATIMA(squares) and AMADEUS(solid circles) do not exceed the values expected from the uncertainties of the experimental data, as can be seen in tables of Appendix B.

We deduce from the last discussion that GEANT 3.21 and SRIM 2000 are not suitable to compute energy losses with high accuracy within the scope of our simulations. However, GEANT 3.21 is a powerful tool for Monte-Carlo methods to track the particles through an experimental setup and a good tool to additionally describe the production of Cerenkov radiation. The proposed solution is to introduce ATIMA or AMADEUS into GEANT 3.21 to compute energy losses. While ATIMA is standing alone code is not suitable to be implemented in a Monte-Carlo structure, AMADEUS is rather simple and suitable for our proposes. We decide, then, to implement AMADEUS into GEANT 3.21 Monte-Carlo code.

2.2 Energy Straggling

When ions penetrate matter, the statistical fluctuations of the impact parameters as well as the variation of the transferred momenta in the scattering events cause a fluctuation in the energy-loss distribution. An initially monoenergetic beam, after passing through a thickness of material, will show a distribution in energy rather than a delta-function peak shifted down by the mean energy-loss.

From a theoretical point of view, the calculation of the distribution of energy losses for a given thickness of absorber is a difficult mathematical problem and, for simplicity, is generally divided into two cases: thick absorbers and thin absorbers.

Thick Absorbers: The Gaussian Limit

For relatively thick absorbers, such that the number of collisions is large, it can be easily shown that the energy-loss distribution has a Gaussian shape. This follows directly from the Central Limit Theorem in statistics which states that the sum of N random variables approaches that of a Gaussian-distributed variable in the limit $N \rightarrow \infty$. If we take our random variable to be dE, the energy lost in a single atomic collision and assuming there are a sufficient number of collisions N, then the total energy lost will approach the Gaussian form

$$f(x,\Delta) \propto exp(\frac{-(\Delta-\overline{\Delta})^2}{2\Omega^2}) \tag{2.13}$$

with x being the thickness of the absorber, Δ the energy loss in the absorber, $\overline{\Delta}$ the mean energy loss and Ω the standard deviation of the distribution.

For non relativistic heavy particles the spread Ω of this Gaussian was calculated by Bohr to be [26]:

$$\Omega^2_{Bohr} = 4\pi z^2 N_a Z \Delta x \quad [MeV^2] \tag{2.14}$$

where $N_a \cdot Z \cdot \Delta x$ is the target number of electrons per unit area. This formula can be extended to relativistic particles using the expression [27]:

$$\Omega^2 = (\frac{1-\frac{1}{2}\beta^2}{1-\beta^2})\Omega^2_{Bohr} \tag{2.15}$$

where β is the velocity of the particle and Ω_{Bohr} is the Bohr deviation given by expression 2.14.

We have to mention that this would be our case, since we are going to work with thick materials and with relativistic heavy ion projectiles.

Thin Absorbers: The Landau and Vavilov Theories

This case is important when the absorber is, for example, a gas. In contrast to the thick absorber case the number of collisions N is too small to apply the Central Limit Theorem and then is extremely complicated to calculate. This is due to the possibility of large energy transfers in a single collision. The maximun energy transfer is induced in a knock-on collision case, kinematically is fixed to [28]:

$$W_{max} = \frac{2m_e c^2 \beta^2 \gamma^2}{1 + 2(\frac{m_e}{M})\sqrt{1+\beta^2\gamma^2} + (\frac{m_e}{M})^2} \tag{2.16}$$

If the incident particle is much more massive than the electron this expression could be simplified to $W_{max} \approx 2m_e c^2 \beta^2 \gamma^2$. These events have small probability but add a long tail to the high energy side of the energy-loss probability distribution producing an assymetric shape, a Landau distribution. Assuming this distribution, the position of the peak now defines the most probable energy-loss but not the mean energy-loss.

Theoretically, basic calculations of this distribution have been carried out by Landau[29], Symon and Vavilov[30]. The principal difference between these theories is the cocient between the mean energy-loss and the maximun transfer energy W_{max}.

2.2.1 Simulation Codes

ATIMA

At relativistic energies the energy straggling is mainly determined by close collisions of the heavy ions with the target electrons. It was shown by C.Scheidenberger et al.[23, 48, 25] that the energy straggling deviates from the well-known theoretical descriptions based on first order perturbation [26, 27], which predict a gaussian width given by expression 2.15. Those experimental results, however, were in good agreement with the predictions from Linhard and Sørensen theory, which takes into

account the deviations from the first order quantum perturbation theory. To get the gaussian distribution predicted in the L-S theory the following expression derived in Ref. [9] has to be used:

$$\Omega_{LS}^2 = \frac{\Omega_{Bohr}^2}{(1-\beta^2)}\chi \tag{2.17}$$

where χ is a function calculated with a program developed by Allan Sørensen[9].

ATIMA code computes energy straggling for all kind of projectiles with $1 \leq Z \leq 92$ from 10 MeV/u up to 450 GeV/u. It uses the Lindhard-Sørensen theory (expression 2.17) to compute energy stragglings for energies larger than 30 MeV/u. For energies below this quantity uses the Bohr expression 2.14 and a linear interpolation in between.

AMADEUS

Amadeus assumes a thick absorber approximation to calculate energy-loss straggling. The number of collisions is considered large enough, the Central Limit Theorem can be then applied and the width of the obtained gaussian is given by [31]:

$$\Omega = 8.79 \times 10^{-3}(\frac{E_{in}}{E_{out}})^{1/3}\frac{Z_p}{A_p}\sqrt{\frac{Z_t}{A_t}d(mg/cm^2)(\delta^2+1)} \quad [MeV/u] \tag{2.18}$$

where Z_p, Z_t, A_p, A_t are the charges and masses of the projectile and target, respectively, d is the target thickness and where

$$\delta = 1 + \frac{E_{in}+E_{out}}{1863MeV/u} \tag{2.19}$$

where E_{in} and E_{out} are the kinetic energies per nucleon of the projectile before and after traversing the absorber material.

GEANT 3.21

This code uses both the Landau theory, Vavilov theory, and the Gaussian theory, according to the thickness of the matreial. In addition includes specific models needed for very thin layers which can not be treated by the Landau model. These models take into account the atomic structure of the target. For thick absorbers, the energy straggling can be approximated by a gaussian:

$$f(\epsilon) = \frac{1}{\xi\sqrt{\frac{2\pi}{\kappa}(1-\beta^2/2)}} exp\left(\frac{(\epsilon-\overline{\epsilon})^2}{2}\frac{\kappa}{\xi^2(1-\beta^2/2)}\right) \tag{2.20}$$

where ξ comes from the Rutherford scattering cross section and is defined as $\xi = \frac{2\pi z^2 e^4 N_a Z\rho x}{m_e\beta^2 c^2 A} = 153.4\frac{z^2}{\beta^2}\frac{Z}{A}\rho x \quad [keV]$ and $\kappa = \xi/W_{max}$. W_{max} is the maximum energy transfer in a knock-on collision event as printed in expression 2.16. The gaussian dispersion is given then by:

$$\Omega^2 = 153.4\frac{z}{\beta^2}\frac{Z}{A}\rho \cdot x \cdot (1-\beta^2/2) \cdot W_{max} \tag{2.21}$$

where z is the charge of the projectile, Z and A are the target charge and mass, respectively, ρ is the target density, x is the target thickness, β is the projectile velocity and W_{max} was defined above.

2.2.2 Results

In figure 2.2 we show the comparison between the different codes under study. We can observe that the results obtained with ATIMA and AMADEUS are different, but the behaviour of the energy straggling as a funtcion of the projectile velocity is similar. However, we oberve also that GEANT 3.21 code deviates strongly from AMADEUS at low energies (up to 75 %), while at higher energies these differences become shorter.

Only a few experimental measurements on energy straggling are available [23, 25, 48]. From the comparison of this measurements with the figure 2.2 it follows that, in some cases, the measured values deviate from the Bohr prediction (used by AMADEUS) by a factor up to more than 2. These deviations are predicted by the Linhard and Sørensen theory, which is implemented in ATIMA code. We can conclude from the figure 2.2 that GEANT 3.21 code predictions are not useful

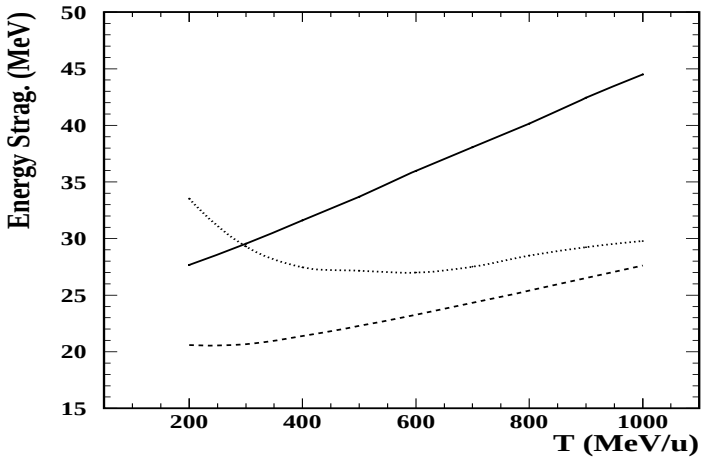

Figure 2.2: *Energy straggling values obtained with the different codes under study as a function of the projectile energy: ATIMA (solid line), AMADEUS (Dashed line) and GEANT 3.21 (dot line). The simulations were made for a $^{208}Pb_{82}$ projectile, choosing the same nuclide as target. The thickness of the target was chosen to be 10% of the range.*

because these predictions do not follow a regular behaviour, that is, it is well known that the energy straggling grows as projectile energy does and this behaviour is not reproduced with GEANT 3.21 code The solution is to implement inside the GEANT 3.21 code external subroutines to compute the energy straggling. Once again, for simplicty, we decided to insert the AMADEUS formula into the GEANT code despite of the fact that ATIMA code is closer to the Lindhard and Sørensen theory.

2.3 Angular Straggling

In addition to inelastic collisions with the atomic electrons of the target, charged particles passing through matter also suffer elastic Coulomb scatterings from nuclei, although with smaller probability. Ignoring spin effects and screaning, these collisions can be described by the well known Rutherford formula:

$$\frac{d\sigma}{d\Omega} = z^2 Z^2 r_e^2 \frac{mc/\beta p}{4sin^4(\theta/2)} \tag{2.22}$$

where z is the charge of the projectile, Z is the charge of the target, r_e is the

Bohr radius, m, p and β are the mass, momentum and velocity of the projectile, respectively and θ is the deflection angle from the initial trajectory.

Because of its angular dependence, the majority of these collisions result in a small angular deflection of the particle. The particle follows a random path inside the matter and the cumulative effect of these small angle scattering results in a net deflection from the original particle direction. We can say that the particle has suffered **multiple scattering** if the average number of independent scattering events is large and the energy-loss on each collision is small or negligible. The problem, then, can be treated statistically to obtain a probability distribution for the net angle of deflection as a function of the thickness and properties of the traversed material. Rigurous calculations of multiple scattering are extremely complicated and there exist several formulations with different sofistication levels. The most commonly used is the small-angle approximation of Moliere [32]. This has been demonstrated to be generally valid for all particles up to angles of 30^o with exception of slow electrons ($\beta < 0.05$) and electrons traversing heavy elements.

We will see tha we have to deal with small net angle deflections. In this case we can use the multiple scattering gaussian approximation, ignoring the small probability of large-angle single scattering. According to this, a very good estimation of the gaussian width is obtained using an empirical formula proposed by Highland [33]:

$$\sqrt{\langle\theta^2\rangle} = \frac{20[MeV/c]}{p\beta} z \sqrt{\frac{x}{X_0}} \left(1 + \frac{1}{9} log_{10}\left(\frac{x}{X_0}\right)\right) \tag{2.23}$$

where z is the charge of the projectile, p and β its momentum and velocity respectively, x(cm) is the thickness of traversed material and X_0 is the radiation length, a variable characteristic for each material.

2.3.1 Simulation Codes

ATIMA

The code ATIMA computes the angular straggling using a modified version of the Highland expression [33]:

$$\sqrt{\langle\theta^2\rangle} = \frac{14.1[MeV/c]}{p\beta} z \sqrt{\frac{x}{X_0}} \left(1 + 0.038 ln\left(\frac{x}{X_0}\right)\right) \tag{2.24}$$

where the radiation length X_0, is computed as follows:

$$\frac{1}{X_0} = 4\alpha r_e^2 \frac{N_a}{A}\left(Z^2\left[L_{rad} - f(Z)\right] + ZL'_{rad}\right) \tag{2.25}$$

where α is the fine structure constant, r_e is the electron radius, N_a is the Avogadrus number, Z is the medium charge, $L_{rad} = ln\left(184.15Z^{-1/3}\right)$, $L'_{rad} = ln\left(1194Z^{-2/3}\right)$ and f(Z) is a function of the medium charge given by:

$$f(Z) = a^2\left[(1+a^2)^{-1} + 0.20206 - 0.0369a^2 + 0.0083a^4 - 0.002a^6\right]; a = \alpha Z \tag{2.26}$$

AMADEUS

The code AMADEUS computes the angular straggling also with the Highland expression [33], but modified as follows:

$$\sqrt{\langle\theta^2\rangle} = \frac{14.1[MeV/c]}{\sqrt{\beta_0 p_0 \beta_1 p_1}} z\sqrt{\frac{x}{X_0}}\left(1 + \frac{1}{9}log_{10}\left(\frac{x}{X_0}\right)\right) \tag{2.27}$$

where $\beta_0, p_0, \beta_1, p_1$ are the velocity and momentum before and after traversing the material, respectively. The radiation lenght is computed as follows:

$$X_0 = \frac{716.405A}{Z^2}\left[ln\left(\frac{184.15}{Z^{1/3}}\right) - 1.202\alpha^2Z^2 + 1.0369Z^4 - \frac{1.008\alpha^6Z^6}{1+\alpha^2Z^2}\right] \tag{2.28}$$

We can observe that not only the expression to compute the angular straggling is different in both codes, ATIMA and AMADEUS, but also the expressions to calculate the radiation length X_0.

GEANT 3.21

The Highland expressions (2.23, 2.24 and 2.27) can introduce errors if they are used in each integration step because the angle $\theta(x+\Delta x) \neq \sqrt{\theta^2(x) + \theta^2(x+\Delta x)}$

, limiting their use in a Monte-Carlo method like GEANT 3.21. To avoid this limitation GEANT 3.21 uses the following expression proposed by Lynch [36]:

$$\langle\theta^2\rangle = 2\frac{\chi_c^2}{1+F^2}\left(\frac{1+\nu}{\nu}ln(1+\nu)-1\right) \tag{2.29}$$

where

$$\nu = \frac{\Omega_0}{2(1-F)} \qquad\qquad \Omega_0 = \frac{\chi_c^2}{1.167\chi_a^2}$$

$$\chi_c^2 = 0.157z\left(\frac{Z(Z+1)}{A}\right)\frac{x}{p^2\beta^2} \qquad \chi_a^2 = 2.007\times10^{-5}Z^{2/3}\left(1+3.34\left(\frac{Zz\alpha}{\beta}\right)^2\right)/p^2$$

The variable p is the incident particle momentum, x is the target thickness in mg/cm^2, z is the charge of the particle, Z and A are the charge and mass of the target, respectively and α is the fine structure constant. Tha parameter Ω_0 may be interpreted as the mean number of scatters. The factor F represents the fraction of the Moliere distribution to be taken into consideration, a value lower than 1 is necessary since, taking the entire distribution into account results in an infinite value for $\langle\theta^2\rangle$. The parameter χ_c takes into account the characteristics of the material and the energy of the projectile, while χ_a takes into account the electron screening for the nuclei electromagnetic field. The code GEANT adopts the values F=0.98 and Ω_0=40000 scatters and then, the expression 2.29 yields results better than 2 %.

2.3.2 Results

Despite of the different ways to compute the angular straggling, in figure 2.3 we can observe that the results are quite approximated for all the codes under study. In that figure we show the results obtained from the three codes for a combination of a heavy projectile ($^{208}Pb_{82}$) on a light target ($^{27}Al_{13}$). We can observe that the results obtained for all of the codes are very similar. This fact can be also observed in figure 2.4, where the calculation is done for a heavy projectile ($^{238}U_{92}$) passing trough a heavy target ($^{208}Pb_{82}$). All the simulations made for different projectile-target

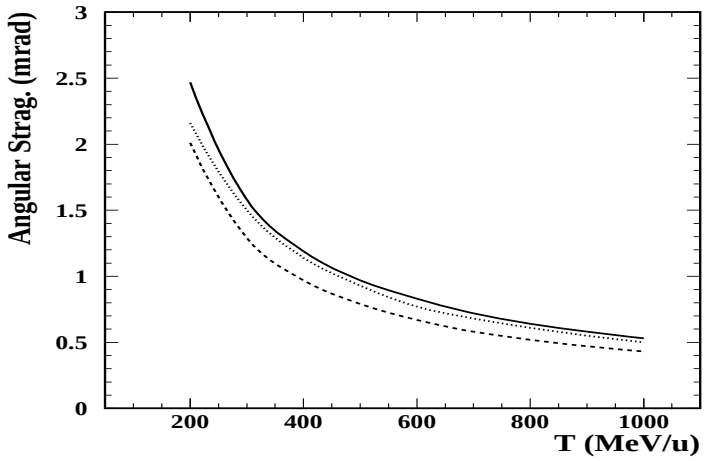

Figure 2.3: *Angular straggling values obtained with ATIMA (solid line), AMADEUS (dashed line) and GEANT 3.21 (dot line) for a* $^{208}Pb_{82}$ *projectile passing trough a* $^{27}Al_{13}$ *target as a function of the projectile energy. The target thickness was chosen to be 10% of the projectile range.*

combinatios gave the same good agreement. We can conclude from this statement that the formulation in GEANT 3.21 code is valid to evaluate the angular straggling.

For a complete analysis of the code, we compare in figure 2.5 the results given by the code GEANT 3.21 code with experimental data of angular straggling measured by Iwasa et al.[34]. In this plot we can observe the results obtained for a heavy projectile, $^{238}U_{92}$, passing through two target combinations, $^{238}Ti_{92}$ and $^{238}Au_{92}$. As can be seen, the agreement between the experimental data and the simulations is quite good. We do not need then to include in the GEANT 3.21 code any external subroutine to compute the angular straggling.

2.4 Reactions rates

As we mentioned in Chapter 1, a Cerenkov detector is needed to measure ion velocities whithin the frame of the R^3B experimental setup. This Cerenkov detector is composed by several layers of matter: radiator, quartz mirror and a purified Nitrogen atmosphere. Taking into account all these matter foils more than $2g/cm^2$ of matter is situated in the beam line. This can be considered as an additional target for the relativistic beam. Then it is necessary to analyse and estimate the reaction rates for the nuclides whithin the Cerenkov setup and compare them with those

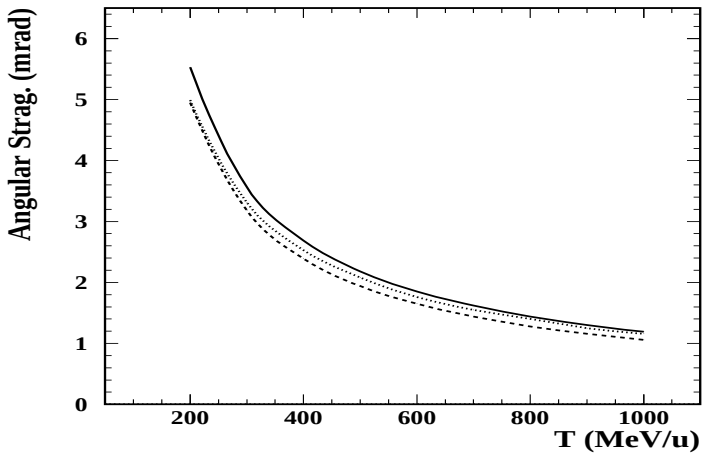

Figure 2.4: *Angular straggling values obtained with ATIMA (solid line), AMADEUS (dashed line) and GEANT 3.21 (dot line) for a $^{238}U_{92}$ projectile passing trough a $^{208}Pb_{82}$ target as a function of the projectile energy. The target thickness was chosen to be 10% of the projectile range.*

given by the target. We will calculate the cross sections for both electromagnetic disotiation (E.M.D.) and nuclear interaction processes with the nuclei which form the Cerenkov materials (Carbon, Fluor, Silicon, Oxigen and Magnesium). From these cross sections the reaction probabilities can be calculated as:

$$P = 1 - e^{-\frac{N_a}{A}\sigma_T \rho x} \tag{2.30}$$

where N_a is the Avogadrus number, A and ρ are the mass number and density of the target nuclei, x is the target thickness and σ_T is the total cross section (nuclear + EMD).

In this expression we have to separate the ifluence of the different nuclei which compound a material. We have to calculate it weight porcentage and take into account the different mass number for the nuclei. We will compute this, as an example, for the C_6F_{14} radiator we get:

$$P = 1 - e^{-N_a \rho x \left[\frac{\sigma_T^C}{A_C} W_C(C_6F_{14}) + \frac{\sigma_T^F}{A_F} W_F(C_6F_{14})\right]} \tag{2.31}$$

where W_C and W_F are the weight porcentages of Carbon and Fluor, respectively, in C_6F_{14}. On the other hand σ_T^C and σ_T^F are the cross sections for any given projectile

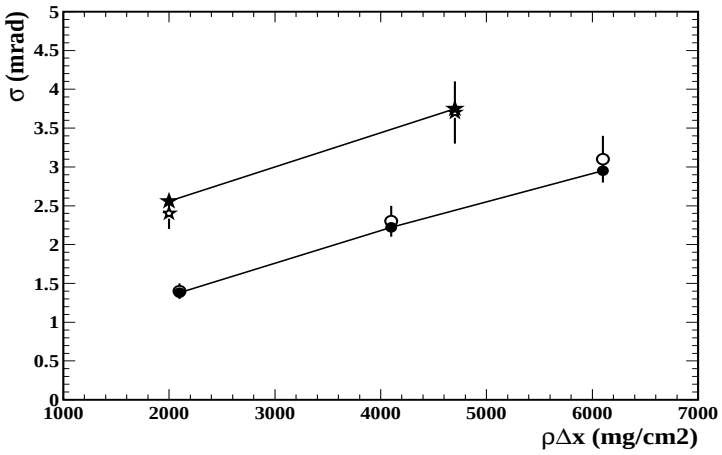

Figure 2.5: *Comparison between GEANT 3.21 simulated values (open symbols) and experimental data (solid symbols) measured by Iwasa et al.[34]. Two target-projectile combinations are plotted. A 943 MeV/u* $^{238}U_{92}$ *projectile passing trough a* $^{48}Ti_{22}$ *target (circles) and through a* $^{197}Au_{79}$ *target (stars).*

on Carbon and Fluor, respectively.

To evaluate the total nuclear cross section, we have used the microscopic description of Karol [37], and modified by Brhom [38]. Karol showed using a Glauber type calculation, that the main contribution to the total reaction cross section is given by the tail of the nuclear matter distribution. Additionally, he proposed to use a simplified description of these distributions by using Gaussian instead of Fermi-like functions. Brhom used an alternative statistical description of the nucleon-nucleon interaction, demostrated equivalent to that from Karol. In his model, realistic nuclear distributions were introduced, as well as the neutron and proton diffuseness. This model gives rather realistic results, with an accuracy within 10%. We can compare similar reactions as those studied in this work, in table 2.1.

Additional components to the total reaction cross sections as could be *electromagnetic dissociation processes* E.M.D., are only relevant for collisions between heavy ions. The procedures described in [39] and [40] allows to evaluate accurately this cross section. In table 2.1 we can see some measured values of the total cross section (nuclear + E.M.D.) compared with the code. As can be observed, the simulated values are in a quite good agreement with the measured data.

The interaction probability of any nucleus passing trough the whole cerenkov setup can be evaluated with the total cross section (Nuclear + E.M.D.) and the characteristic thicknesses. This reaction probability for the whole Cerenkov system

Projectile	Target	Energy (MeV/u)	σ_T^{exp}(mb)	σ_T^{sim}
$^{197}_{79}Au$	p	800	1780 ± 400	1727 ± 173
$^{208}_{82}Pb$	p	1000	1837 ± 220	1799 ± 180
$^{208}_{82}Pb$	d	1000	2079 ± 240	2321 ± 232

Table 2.1: *Comparison between the experimental measured total cross sections (σ_T^{exp}) and the simulated ones (σ_T^{sim}) for several target-projectile combinations.*

will be evaluated as follows:

$$P = P_{radiator} \cdot P_{N_2} \cdot P_{SiO_2^{Mirr}} \tag{2.32}$$

Chapter 3

Simulation of the Cerenkov detector

Once of the key detectors in the setup proposed for the R^3B project is the Cerenkov detector. This detector will provide an accurate measurement of the velocity of the reaction products. The intention of this work is to simulate, study and optimize a Heavy Ion Ring Imaging Cerenkov detector (HIRICH). The chapter starts with a brief introduction to the Vavilov-Cerenkov radiation, then we will make a description of the different radiator materials that can be used is such a detector, finally we will make a complete description of the simulation of the detector. In order to evaluate the validity of the simulations, two features will be taken into account, from one hand, theoretical estimations of the velocity resolution will be made in order to compare the results with the simulated ones. From another hand, data obtained with the HIRICH built at the Munich Technical University [41] will be taken as a comparison reference for our simulations.

3.1 Description of the Vavilov-Cerenkov radiation.

Vavilov-Cerenkov radiation is an electromagnetic shock-wave phenomenon appearing whenever a charged particle travels with a velocity v=cβ in an dielectric optical medium of refractive index n faster than the velocity of light in the medium c/n (i.e. v >c/n or β>1/n). The Cerenkov polar emission angle Θ_C relative to the particle direction is given by the relation

$$cos\Theta_C = \frac{1}{n\beta} \tag{3.1}$$

however, the azimuthal emission angle ϕ has a flat distribution between 0 and 2π. The intensity and spectrum of the radiation is given by the Frank-Tamm relation

$$\frac{dN_{ph}}{dE} = \left(\frac{\alpha}{\hbar c}\right) Z^2 d sin^2\Theta_C \tag{3.2}$$

where N_{ph} is the number of photons with energy between E and $E + dE$, α is the electromagnetic fine structure constant, d is the particle path length in the medium and Z is the charge of the particle. Combining, we obtain the (β,n) spectral dependence

$$\frac{dN_{ph}}{dE} = \left(\frac{\alpha}{\hbar c}\right) Z^2 L[1 - (1/n\beta)^2] \tag{3.3}$$

The dispersion of an optical medium is expressed by a function n=n(λ). This functional dependence must be included when integrating equation 3.3 to obtain the number of produced Cerenkov photons, N_{ph}. Note from equation 3.3 that the Cerenkov photon spectrum is flat for a constant value of n, but for real media $n(\lambda)$ increases with E causing an enhancement of the Ultra-Violet spectrum.

3.1.1 Characteristics of the radiation

From the previous relations we can deduce some characteristics of the Vavilov-Cerenkov radiation:

- **Threshold value for the radiation**. For a given refractive index n there is a velocity β_{th} , below which no Vavilov-Cerenkov radiation is observed: $\beta_{th} = 1/n$.

- **Saturation angle**. There exists a maximum radiation angle, corresponding to a ultra-relativistic particle with $\beta \approx 1$:

$$\Theta^{\infty} = cos^{-1}(1/n) \tag{3.4}$$

- **Radiation spectrum**. To derive the Frank-Tamm relations (expressions 3.2 and 3.3) we have assumed that the refractive index of the radiator medium is constant. To be rigorous, every medium is dispersive, therefore, the refractive index depends on the wavelength. The condition $n(\lambda) > 1/\beta$ is only valid if the wavelength is larger than the ultraviolet. Apart from this, the number of photons emitted scales with λ^2, consequently, the photon emission with wavelengths larger than the visible (infrared, radio) is strongly inhibited, and consequently mainly radiation in the visible and ultra-violet is observed.

- **Intensity of the radiation** increases with the charge and velocity of the particle: From equation 3.3, the number of photons scale with Z^2 and $(1 - (\beta n)^{-2})$.

3.2 RICH and HIRICH concepts

The development of Ring Imaging Cerenkov counters started about 20 years ago with the publication by Seguinot and Ypsilantis [42]. Recently, a novel device for velocity measurement of relativistic ions was developed based on Vavilov-Cerenkov radiation, the Heavy-Ion Ring Imaging Cerenkov detector (HIRICH) [41]. The HIRICH is characterized by a thin liquid or solid state radiator and a proximity focusing geometry (see figure 3.1). The photons emitted by the radiator are reflected by the mirror onto the photon detector, where a ring pattern appears.

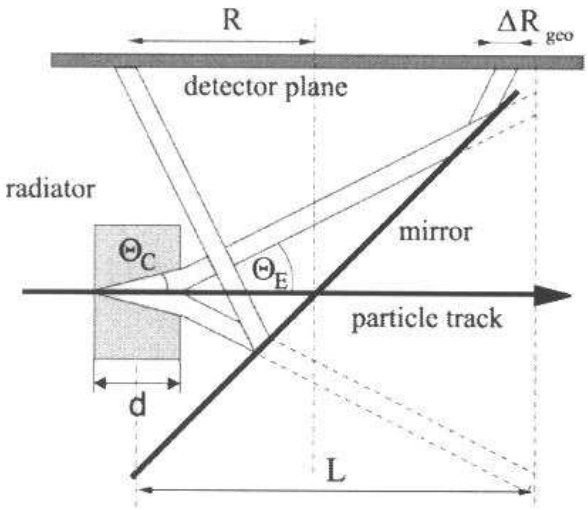

Figure 3.1: *Example of a Cerenkov detector with a proximity focusing geometry [41].*

3.2.1 Radiator materials

The refractive index of the radiator will determine the minimum velocity to generate Vavilov-Cerenkov radiation. Given a certain radiator medium, the measurement of the velocity β can be made above the Cerenkov threshold $\beta_{th} = 1/n$. At threshold the amount of light is zero, but grows quickly with β just above the threshold (see expression 3.3).

We can choose between different kinds of radiators: solids, liquids, gaseous and aerogel materials. Liquids and solids are much denser than gases. Therefore, the charged particle track length required to generate a sufficient number of photons in such media is comparatively shorter.

Traditional gas, solid and liquid radiators have refractive indexes smaller than 1.0018 (gaseous C_6F_{14}) or larger than 1.27 (liquid C_6F_{14}). The only possible way to partially close the gap in refractive indexes is represented by silica aerogel that can be produced in a fairly wide range from n=1.004 to n=1.1. Aerogel is a laboratory sintetized material that could have a density as low as three times that of the air. It essentially consists on grains of amorphous SiO_2 with sizes ranging from 1 to 10 nm linked together in a three-dimensional structure filled by trapped air. It exists a simple relationship between the resultant refractive index and the aerogel density ρ in g/cm^3 given by $n = 1 + 0.21\rho$ [43].

In the table 3.1 we show the different refractive index ranges covered by different radiators. In this work we will deal with heavy ions with energies of about several hundred MeV/u. From the values given in table 3.1 we conclude that we must rule out the possibility of working with gaseous or aerogel radiators due to the energy thresholds of these materials. We can only use liquid or solid radiators.

3.2.2 Theoretical estimations of the β-resolution

The aim of a RICH or a HIRICH detector is to determine the velocity of a particle, β, from the measurement of the ring radii of the induced Vavilov-Cerenkov radiation. The velocity resolution can be obtained from equation 3.1 as:

$$\frac{\Delta\beta}{\beta} = \frac{1}{\sqrt{N}} tan\Theta_C \Delta\Theta_C \tag{3.5}$$

where N is the number of detected photons and Θ_C is the Cerenkov angle. This expression can be manipulated to give the velocity resolution as a function of the

Radiator Nature	Material	$\bar{n}$	Threshold Energy
Gaseous	He	1.000035	$>$ 110 (GeV/u)
	C_5F_{12}	1.0018	$>$ 14 (GeV/u)
Aerogel		1.004	$>$ 9 (GeV/u)
		1.1	1.3 (GeV/u)
Liquid	C_6F_{14}	1.28	550 (MeV/u)
Solid	MgF_2	1.426	375 (MeV/u)
	SiO_2	1.557	280-750* (MeV/u)

Table 3.1: *Refractive index ranges covered by the different radiators. The projectile energy thresholds (calculated according to expression for the different materials are also shown.*The solid SiO_2 radiator, beyond 750 MeV/u can only work in total internal reflection (see chapter 4).*

directly measured quantity, the ring radius, as follows (see appendix C):

$$\frac{\Delta\beta}{\beta} = \frac{1}{\sqrt{N}}\frac{\Delta R}{R}\Gamma \tag{3.6}$$

where R is the ring radius. The factor Γ in the previous expression, is named ***geometrical factor***. It comes from the fact that photons are refracted at the boundary of two media with different refractive indexes (Snellius law).

The intention of this section is to discuss and estimate numerically the different contributions to the radius dispersion, and thus to the velocity resolution, for a further comparison with the simulated values. The uncertainty ΔR in the measured ring radii and thus the uncertainty $\Delta\Theta_C$ in the Cerenkov angle is affected by several optical and geometrical factors: the energy loss of heavy ions on their path through the radiator, the chromatic aberration of the radiator material and the geometrical broadening by the finite thickness of the radiator, in addition to the number of detected photons and the pixel size of the photon detector. In the following we will present some theoretical calculations. These results will be compared later with full simulations of the RICH detector.

Optical dispersion or chromatic aberration

The refractive index of a medium depends on the wavelength of the considered photons, $n{=}n(\,\lambda\,)$. Consequently, each photon is emitted with a different Cerenkov

angle. The angular spread produced by the optical dispersion leads to an uncertainty in the determination of the Cerenkov angle $\Delta\Theta_C$. From equation 3.1 we can derive:

$$\frac{\Delta\Theta_C}{\Delta\lambda} = \frac{1}{\sqrt{n^2\beta^2 - 1}} \frac{1}{n} \frac{\Delta n}{\Delta\lambda} \tag{3.7}$$

being λ the wavelength of the photon, n the refractive index of the medium, Θ_C the Cerenkov angle and β the velocity of the beam particle in units of the velocity of light.

In order to estimate the contribution of this effect to the velocity resolution we take two limit cases: a heavy ion with a low kinetic energy, 600 A MeV, and a heavy ion with 1 A GeV. We will choose a liquid C_6F_{14} radiator in order to compare these results with those obtained with the HIRICH of R.Gernhauser [41]. We are going to work in a wavelength range from 193.75 nm to 196.83 nm (energies of 6.4 eV and 6.3 eV respectively)[1]. For the calculations we will use the mean refractive index in this range, that is n=1.28622. The results using expression 3.7 are shown in table 3.2.

Energy (MeV/u)	β	Θ_C	$\Delta\Theta_C$	$\Delta\beta/\beta$
600	0.7938	11.4	0.065	0.13%
1000	0.8760	27.3	0.026	0.133%

Table 3.2: *Effect of the dispersion law on the velocity resolution. Limit cases of 600 MeV/u and 1000 MeV/u are studied. The projectile is a $^{96}Ru_{44}$. The radiator is an 8 mm thickness C_6F_{14}. The Cerenkov ring radii were measured at 200 mm from the radiator. The photon statistics is not considered.*

Paradoxically, the velocity resolution is better at lower energy (if we do not take into account the number of detected photons). This is because we are working in a narrow wavelength range, where the refractive index almost does not change. From equation 3.6 the factor $tan\Theta_C$ dominates the velocity resolution and this factor becomes larger as increasing the velocity.

Radiator thickness

The different emission points of the photons along the particle trajectory inside the radiator induce an additional dispersion proportional to the radiator thickness

[1] We are working in the UV region of the spectrum and due to transmission and efficiency effects these numbers are representatives for our simulations

$\Delta R = d \cdot tan\Theta_C$. The corresponding uncertainty in the measurement of the radii will be given by the relation [45]:

$$\frac{\Delta R}{R} = \frac{d}{L}\frac{\sqrt{1 - n^2 sin^2\Theta_C}}{ncos\Theta_C} \tag{3.8}$$

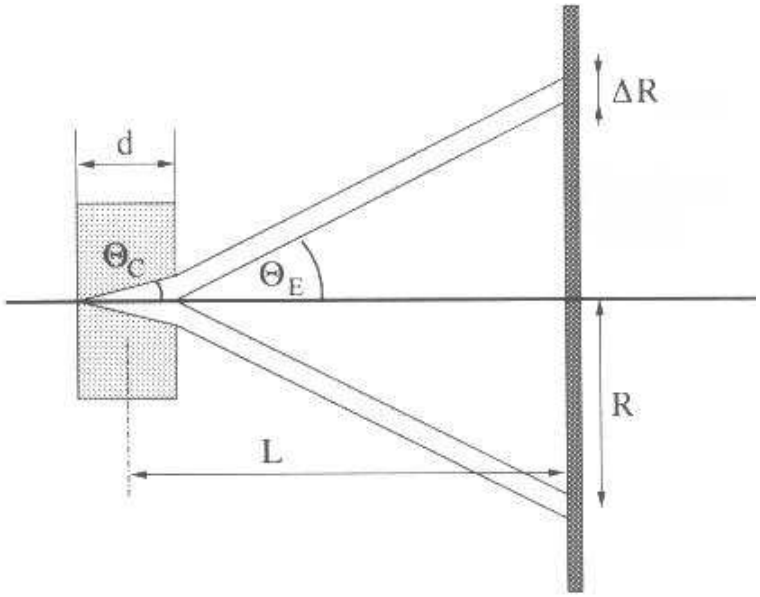

Figure 3.2: *The results with this geometry are identical to the 90 degrees rotated geometry showed in figure 3.1* [41] .

We can estimate this quantity for the two limit cases mentioned before. The results are given in the table 3.3

Energy (MeV/u)	β	Θ_C	$\Delta R/R$	$\Delta\beta/\beta$
600	0.7938	11.4	3%	0.11%
1000	0.8760	27.3	2.8%	0.48%

Table 3.3: *Effect of the radiator thickness on the velocity resolution. Limit cases of 600 MeV/u and 1000 MeV/u are studied. The projectile is a* $^{96}Ru_{44}$. *The radiator is an 8 mm thickness* C_6F_{14}. *The Cerenkov ring radii were measured at 200 mm from the radiator. The photon statistics is not considered.*

From the table 3.3we conclude that both limit cases give similar values of $\Delta R/R$, but the velocity resolution is better in the lower energy case. This is due only to

the difference in the geometrical factor because of the different Cerenkov emission angles. This factor increases with the ion velocity.

Energy-loss within the radiator

Particles traversing the radiator suffer a continuous energy loss due to electromagnetic interactions. This energy loss affects the velocity resolution by a gradual decrease of the Cerenkov angle and a reduction of the photon yield. The variation of Cerenkov angle is related to the energy-loss by [46]:

$$\Delta\Theta_C = \frac{(n^2 cos^2\Theta_C - 1)^{3/2}}{n sin\Theta_C} \frac{1}{Mc^2}\Delta E \tag{3.9}$$

where Mc^2 is the mass of the projectile, n is the refractive index of the medium and Θ_C is the Cerenkov emission angle. Once more, we estimate some limit cases, not only in energy but also in projectile charge because of the dependence on Z^2 for the stopping power. We fixed to 8 mm the thickness of the radiator (C_6F_{14}) and we measured the ring radii at 200 mm from the radiator. The table 3.4 summarizes the results.

Projectile	Energy (MeV/u)	β	Θ_C	ΔE (MeV/u)	$\Delta\Theta_C$	$\Delta\beta/\beta$
$^{10}B_5$	600	0.7938	11.4	8	0.014	0.28%
$^{10}B_5$	1000	0.8760	27.3	6	0.002	0.1%
$^{96}Ru_{44}$	600	0.7938	11.4	66	0.116	2.3%
$^{96}Ru_{44}$	1000	0.8760	27.3	59	0.017	0.9%
$^{238}U_{92}$	600	0.7938	11.4	120	0.211	4.2%
$^{238}U_{92}$	1000	0.8760	27.3	105	0.028	1.45%

Table 3.4: *Velocity resolution for several projectiles at the limit cases of 600 MeV/u and 1000 MeV/u calculated from expression 3.5.* $\Delta\Theta_C$ *is given by expression 3.9. The radiator is an 8 mm thickness* C_6F_{14}*. The ring radii were measured at 200 mm from the radiator. The photon statistics is not considered.*

We observe in table 3.4 how the energy-loss plays the most important role in the velocity resolution (whenever the photon statistics is not taken into account), dominating over other effects as the radiator thickness and the optical dispersion. This last effect could compete with the energy loss if we were working in a broad wavelength range, where the refractive index could play a more dramatical role.

Photon statistics

Up to now we have not taken into account the statistics of detected photons. The number of expected photons can be estimated directly by integration of the Frank-Tamm relation (equation 3.2). The number of emitted photons will not be the number of detected ones due to transmission effects and quantum detection efficiencies (see figure 3.3). In order to estimate the final velocity resolution we should consider the statistic of detected photons according to expression:

$$\frac{\Delta\beta}{\beta} = \frac{1}{\sqrt{N_{ph}}}\sqrt{\left(\frac{\Delta\beta}{\beta}\right)^2_{rad} + \left(\frac{\Delta\beta}{\beta}\right)^2_{n(\lambda)} + \left(\frac{\Delta\beta}{\beta}\right)^2_{dE}} \tag{3.10}$$

where N_{ph} is the number of detected photons, rad, $n(\lambda)$ and dE means the velocity resolution due to the radiator thickness, the optical dispersion and the energy-loss.

We will concentrate now in a particular case, for example, a ^{96}Ru nuclei. For this ion, a typical number of detected photons is larger than a thousand, keeping this in mind, the obtained results are given in table 3.5. This table contains the numerical quantity for each effect.

Energy (MeV/u)	$(\frac{\Delta\beta}{\beta})_{rad}$	$(\frac{\Delta\beta}{\beta})_{n(\lambda)}$	$(\frac{\Delta\beta}{\beta})_{dE}$	$(\frac{\Delta\beta}{\beta})_{theor}$	$\Delta\beta/\beta$
600	0.11%	0.13%	2.3%	2.5%	0.15%
1000	0.48%	0.13%	0.88%	1.0%	0.03%

Table 3.5: *Estimated values for final velocity resolution weighted by the number of detected photons. The projectile is a $^{96}Ru_{44}$. The radiator is an 8mm thickness C_6F_{14} The ring radii were measured at 200 mm from the radiator.*

In the next section, we will return over these results and the data obtained from the simulations will be compared with them, keeping in mind that these theoretical estimations were made only to have a first approach to the velocity resolution values.

3.3 Simulation of the Cerenkov detector with GEANT 3.21

In this section we present the results obtained with the full simulations of the Cerenkov detector. We will make a systematic analysis of the different factors which contributes to the velocity resolution. Factors as the energy of the ions, their charge, the thickness of the radiator, the distance between the radiator and the detector, etc, will be systematically discussed.

For the simulation, study and optimization of the HIRICH we will use the code GEANT 3.21. This is a Monte-Carlo code which allows to simulate the whole experimental setup and it is able to make the particle tracking within the setup taking into account the primary interactions of these particles with matter. GEANT 3.21 has implemented some packages for the treatment of Cerenkov effect, the generation, tracking and absortion of the photons through the experimental setup. For a detailed description of the GEANT 3.21 operation with Cerenkov photons see appendix D.

In our simulations we have modified some of the default options of GEANT to calculate the primary interactions of relativistic heavy ions in matter. As explained in chapter 2, the energy loss and anergy straggling are calculated using the subroutine AMADEUS. The angular straggling is computed using the default options expressions by GEANT explained in chapter 2. We also include and empirical parametrization of the absortion of Cerenkov photons in the radiator.

3.3.1 Description of the Cerenkov detector.

The simulated detector is based on a proximity focusing geometry [47] (see figure 3.1). It consists basically on a thick liquid or solid radiator (for liquid radiators two fused quartz windows containing the liquid are sonsidered), a thin VUV-mirror[2] and the photon detector with another fused quartz window at the entrance. Cerenkov light produced by the ions traversing the radiator is reflected by a planar thin VUV-mirror onto the photon detector. Due a tilt angle of 45^o images are not modified and the photon detector is protected from the direct interaction with the beam particles (see figure 3.1). In the following we will make a detailed description of the different components:

[2]In order to compare the simulations with measured data we will simulate the Cerenkov detector build at the Munich Technik Universitet [41]. This detector works on the VUV region of the spectrum but, actually, due to transmission effects, the effective wavelength range is extremely narrow.

- **Radiators:** We will investigate the results obtained with three different radiators: Liquid Perfluorhexan (C_6F_{14}), solid Magnesium Fluoride (MgF_2), solid Fused Quartz (SiO_2).

  The emission photon spectrum for the liquid C_6F_{14} and for the sold SiO_2 radiators are shown in figure 3.3. This figure illustrates the dependence of the photon spectrum with the energy of the incoming particle and the nature of the radiator. As can be observed the intensity of emitted photons in the SiO_2 radiator is higher than in the liquid C_6F_{14} due to the refractive index of the material. In the same way, the intensity also increases with the energy of the projectile. This behavior is explained by the Frank-Tamm relation (3.3).

  The transmission probabilities of the photons inside the radiator has been measured for the liquid C_6F_{14} radiator [48]. For simplicity, the transmission for the solid MgF_2 and SiO_2 radiators was supposed to be the same than the C_6F_{14} one. The transmission used in the simulations is shown in figure 3.3.

- **Fused Quartz windows (SiO_2):** In addition to its use as a radiator, this material is used as windows in the case of liquid radiator.

- **VUV - wirror :** Consists of a 400 μm thickness aluminum foil rotated 45 degrees.

- **Photon detector :** We have just simulated the quantum efficiency of the detector and the pixel size since it plays an important role in the velocity determination. The quantum efficiency is shown in figure 3.3 as given by [48]. At can be observed, the photon detector has an adecuated quantum efficiency only for the ultra-violet range of the spectrum.

- **Purified nitrogen (N_2) atmosphere:** The whole setup is placed in a Nitrogen atmosphere with a mean refractive index n=1.205 in our wavelength range. This nitrogen atmosphere was introduced because it is difficult to manage vacuum inside the radiator box due to the the detector structure.

3.3.2 Velocity determination from the Cerenkov photon rings.

The Cerenkov radiator produces ring imagines in the photon detector as the ones shown in figure 3.4. From these images we can determine the mean radius and the width of the rings. At this point the pixel size of the detector has an essential role. Although the photon distribution for a section of the rings is expected to be Gaussian [48], the pixel size of the detector leads to discrete distributions as shown in figure 3.5. The uncertainty of the radius, ΔR, is calculated as the root mean square (R.M.S) of the data set.

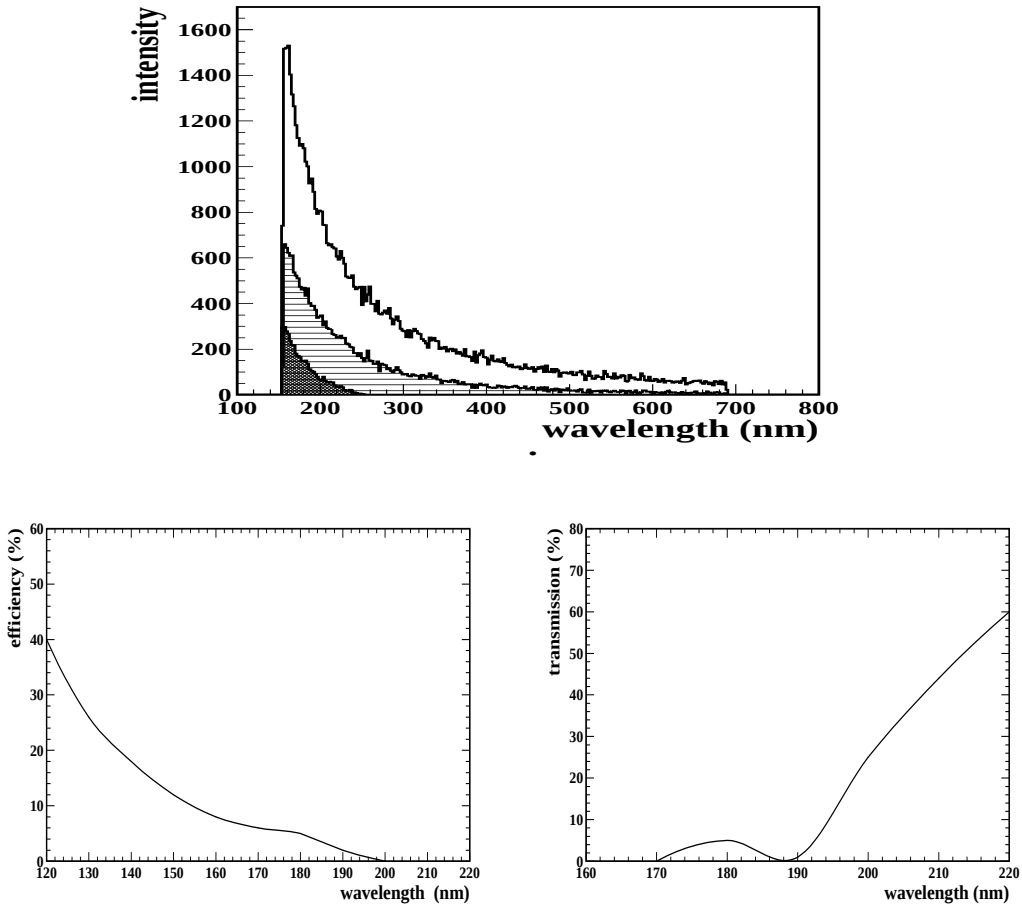

Figure 3.3: ***Upper part:*** *Cerenkov emission spectrum for a* $^{45}_{21}Sc$ *nuclei traversing a solid* SiO_2 *radiator at 600 MeV/u (white histogram), a liquid* C_6F_{14} *radiator at 600 MeV/u (grey histogram) and a liquid* C_6F_{14} *radiator at 800 MeV/u (horizontal hatched histogram) (thicknesses 2 mm).* ***Bottom part:*** *Detection quantum efficiency of the photon detector (left) and transmission probability for the photons through the radiators (right). The same transmission was selected for the three radiators.*

From figure 3.2 we can derive an expression which relates the radius of the photon ring with the velocity β of the ion passing through the radiator. This expression is:

$$R = \frac{d}{2} \cdot tan \left[acos \left(\frac{1}{n_1 \beta} \right) \right] + L \cdot tan \left[asin \left[\frac{n_1}{n_2} sin \left(acos \left(\frac{1}{n_1 \beta} \right) \right) \right] \right] \qquad (3.11)$$

where n_1 and n_2 are the refractive index of the radiator and the expansion gap

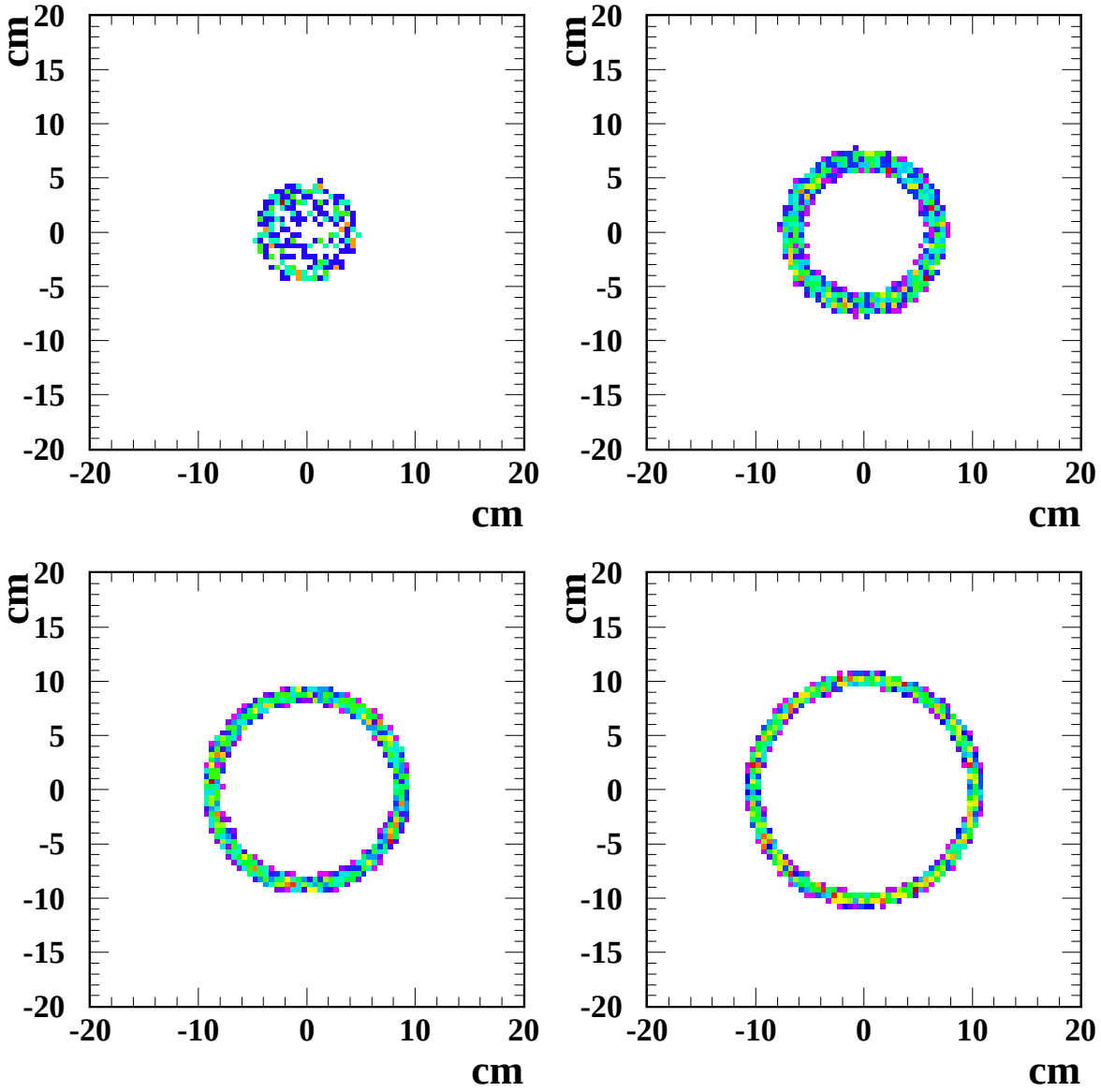

Figure 3.4: *Typical ring patterns produced by the Cerenkov radiation in the photon detector as a function of the energy of the projectile. From up to down and from left to right 600, 700, 800 and 900 MeV/u respectively. The projectile was a* ^{96}Ru *nucleus traversing an 8 mm thickness* C_6F_{14} *radiator and the photon detector was situated 200 mm away from the radiator.*

medium respectively, d is the radiator thickness and L is the distance between the

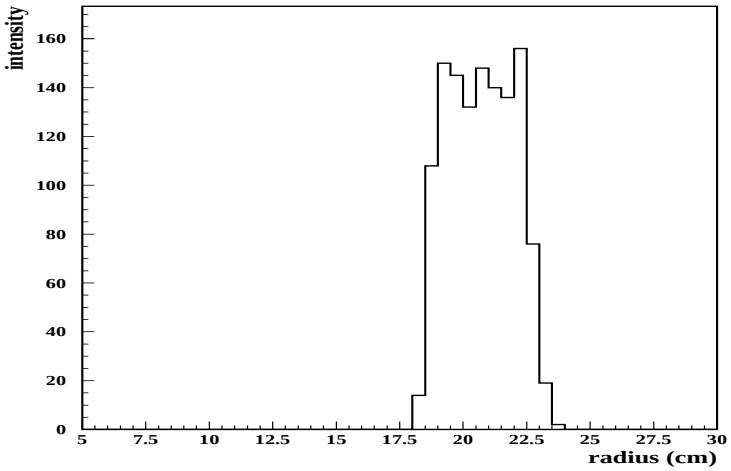

Figure 3.5: *Transversal cut of a ring image produced by the Cerenkov radiation induced by a $^{96}Ru_{44}$ nuclei traversing 4 mm of solid SiO_2 radiator. Due to the pixel size, the shape of the distribution is hidden.*

radiator and the detector. This expression can be manipulated to give:

$$R = \frac{d}{2}\sqrt{n_1^2\beta^2 - 1} + \frac{L}{\beta}\sqrt{\frac{n_1^2\beta^2 - 1}{(n_2^2 - n_1^2) + 1}} \tag{3.12}$$

This expression leads to a 4^{th} degree polynomial solution for β. We have solved this expression by numerical methods chosing an optimized Newton-Raphson method to find the roots of the equation. Only one of the solutions is real and in between 0 and 1.

Two assumptions have been made to find the solution of expression 3.12. On the one hand the refractive indexes were taken as the mean refractive index in the wavelenght range we are working in. On the other hand the emission point was fixed at the middle of the radiator. These assumptions lead to an implicit error in the algorithm. The influence of this effect is shown in figure 3.6. This influence is completely negligible for low energies. At higher energies this effect should be taken into account and added quadratically to the velocity resolution.

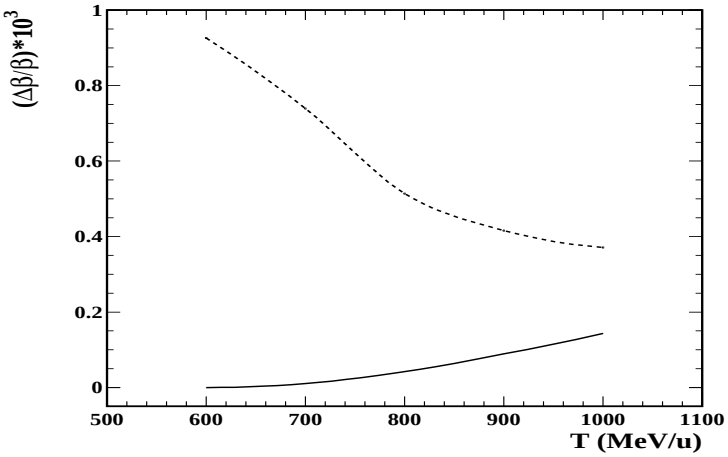

Figure 3.6: *Algorithm error for β resolution calculation (solid line) as a function of the energy of the projectile. The dashed line shown the simulated β resolution for an 8 mm thickness C_6F_{14} radiator. The photon detector was situated 200 mm away from the radiator. The projectile was a $^{96}Ru_{44}$.*

3.3.3 Simulation results for several radiators: liquid C_6F_{14}, solid MgF_2 and solid SiO_2

In this section we want to investigate systematically the velocity resolution that we obtain with different cerenkov radiators. This investigation will allow to optimize the choice of the radiator and to define their thicknesses. In order to check the validity of our simulations, first we will compare them with the estimated velocity resolutions we obtained in section 3.2. In that section we estimated the velocity resolution for a $^{96}Ru_{44}$ nuclei traversing an 8 mm thickness liquid C_6F_{14} radiator at two different energies, taking the same cases we obtain:

- **1.0 GeV/u:** In this case, the velocity resolution obtained from the simulations was $\Delta\beta/\beta \approx 0.04$ %, which is in good agreement with the $\Delta\beta/\beta \approx 0.03$ % estimated in the last section.
- **600 MeV/u:** In this case, the velocity resolution obtained from the simulations was $\Delta\beta/\beta \approx 0.11$ %, which is in also in quite good agreement with the $\Delta\beta/\beta \approx 0.15$ % estimated in the last section.

Second, we will compare our simulation with available measured velocity resolutions [41] obtained with a Cerenkov detector similar to the one we are simulating.

The velocity resolution for the $^{96}Ru_{44}$ nuclei has been experimentally measured for an energy close to 1 GeV/u [41]. The result obtained was $\Delta\beta/\beta \approx 0.08\,\%$ (FWHM). Due to the operation of the photon detector used by this Cerenkov, or simulation has to be multiplied by a factor 1.9 to be realistic. This is due to the fact that when a photon is detected, not only one pixel of the detector is fired, at lest 3 neighbor pixels are also activated, while in the simulations this does not accur. Multipliying the result of our simulation by the factor 1.9 we obtain a velocity resolution $\Delta\beta/\beta \approx 0.07\,\%$ (FWHM), which in good agreement with the measured values.

We conclude from here that the simulated values are in a quite good agreement with the estimated values from the last section and with the experimental measured data. In the following we will systematically simulate the different contributions to this velocity resolution. For the solid SiO_2 radiator, the distance between the photon detector and the radiator will be fixed at 100 mm beacuse otherway the photon rings are too large to be detected.

Atomic number of the incoming ions.

In the expressions we have derived above for the velocity resolution (3.5 and 3.6), the charge of the projectile does not appear explicitly. This dependence is hidden in the statistical factor $1/\sqrt{N}$. From the Frank and Tamm relations 3.2 and 3.3 we notice that the number of generated photons N depends on the square of the projectile charge. Several simulations were made for different radiators in order to study the dependence of the velocity resolution with the charge of the particle crossing the radiator. The results are shown in figure 3.7.

As we observe, we obtain the worst resolution with the smallest charges is in the liquid C_6F_{14}. This result can be explained in termos of the short number of generated photons within the radiator. The best resolution for the low charges is obtained with the solid MgF_2 radiator rather than the solid SiO_2 one, due to the chromatic aberration, larger in the last radiator. In spite of the larger number of generated photons within the SiO_2 this number is not enough to compensate the chromatic dispersion.

However, at high charges (beyond Z=25) it can be observed that the velocity resolution obtained with the solid SiO_2 is better than the one given by the MgF_2 radiator, overcoming the dominant effect of the chromatic aberration due to the large number of generated photons. In addition it can be also observed how the best resolution at high charges is obtained with the liquid C_6F_{14} because in the solid radiators, as we mentioned, the most important factor affecting the resolution is the chromatic dispersion which has a little effect in the liquid radiators.

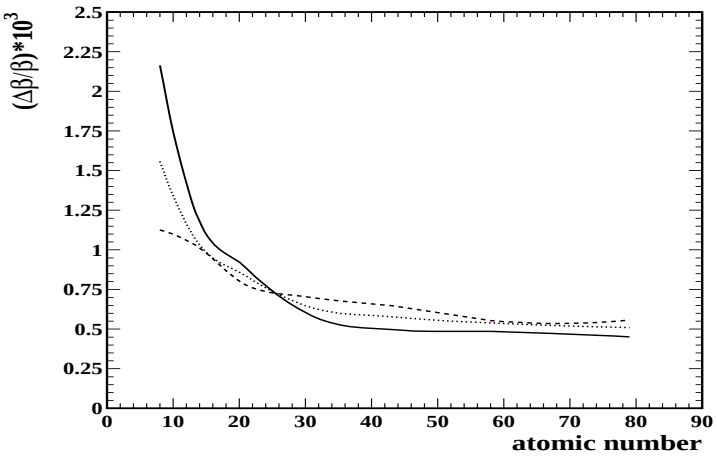

Figure 3.7: *Velocity resolution as a function of the charge of the projectile for several radiators: liquid C_6F_{14} (solid line) , solid MgF_2 (dashed line) and solid SiO_2 (dot line). The energy of the projectile was chosen to be 600 MeV/u. The thickness of the all the radiators was 2 mm except for the liquid C_6F_{14} radiator for which we considered 4 mm. The photon detector was situated 200 mm away from the radiator except for solid SiO_2 which was 100 mm.*

Kinetic energy of the incoming ions.

Expression 3.3 tell us that the number of generated photons in the radiator increases with the energy of the particle. Additionally, from expression 3.6 we conclude that the velocity resolution must improve with the number of detected photons. Several simulations have been made for the three radiators: liquid C_6F_{14}, solid MgF_2 and solid SiO_2 in order to confirm this statement. The results of the simulations are shown in figure 3.8.

As we expected, the velocity resolution improves with the kinetic energy of the incoming ion due to the combination of two effects: first, the larger number of generated photons and, two, the lower energy loss within the radiator. From figure 3.8 it can be observed that, as we explained in the last point, the velocity resolution achieved with the solid SiO_2 is better than the achieved with the solid MgF_2 due to the number of generated photons, overcoming the chromatic dispersion, higher in the SiO_2 radiator. For the same reasons, it is confirmed that the best velocity resolution is achieved for the liquid C_6F_{14} radiator although the number of generated photons is lower than in the solid radiators.

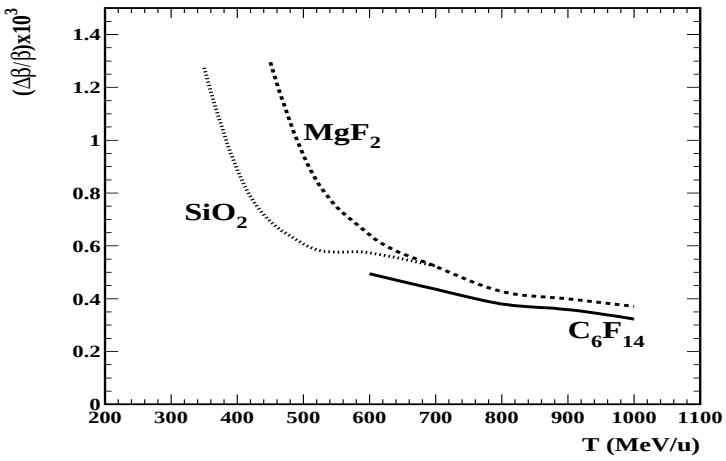

Figure 3.8: *Velocity resolution as a function of the kinetic energy for the nuclei* $^{96}Ru_{44}$. *Both solid radiators were chosen to be 2 mm thickness. The liquid* C_6F_{14} *radiator has 4 mm thickness and the photon detector was situated 200 mm away from the radiator except for solid* SiO_2 *which was 100 mm.*

Thickness of the radiator.

We have seen above that, in addition to the number of generated photons, the most important factors affecting the velocity resolution are the chromatic aberration and the energy loss in the radiator. Then, it would be interesting to analyze the dependence of the velocity uncertainty as a function of the radiator thickness, to see the competition between these effects, the energy loss and the photon generation. The results are given in the figure 3.9

We can observe that, for all the radiators, the number of generated photons cannot overcome the combined effect of energy loss in the radiator and the chromatic aberration. We have to say that we cannot work with very thin radiators due to the method we use to obtain the velocity measurements from the ring radii, which required a photon statistic larger than 100. For this reason we take into account radiator thicknesses which assure a photon statistic large enough.

Granularity of the photon detector.

As we mentioned before, we have not simulated the photon detector module. Any photon which impact in this module is supposed to be detected. The real transmission and quantum detection efficiency were imposed *"a priori"* in the simulation.

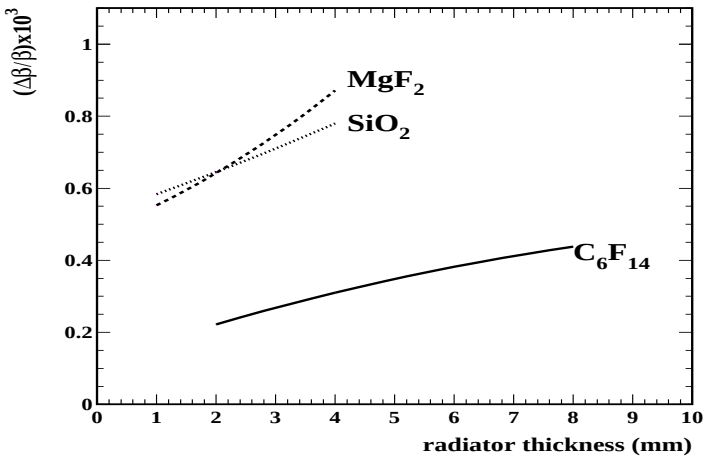

Figure 3.9: *Velocity resolution for several radiator thicknesses for solid SiO_2 (dot line) and MgF_2 (dashed line) and for the liquid C_6F_{14} (solid line) radiators. The projectile was a ^{96}Ru nuclei at 600 MeV/u for both solid radiators and at 1 GeV/u for the liquid one.*

In order to reproduce the results of the HIRICH built at the Munich Technical University, the same pixel size for the photon detector was chosen for our simulations (6 x 6 mm^2).

In figure 3.10 is shown how this pixel size affects to the velocity resolution. This resolution decreases when we increase the pixel size, as we expected, but this effect does not follow the same behavior for all the radiators. The velocity resolution depends strongly on the ring width, ΔR, given mainly by the chromatic aberration and the energy loss. The higher are these contributions, the lower is the influence of the pixel size in the velocity resolution. As an example, the ring width in the case of the C_6F_{14} radiator is $\Delta R \approx 5$ mm (FWHM) and then a granularity higher than this size will affect strongly the velocity resolution. However, for the solid SiO_2 radiator $\Delta R \approx 30$ mm (FWHM) and then the pixel size will not affect so strongly the velocity resolution. This is the reason why the velocity resolution for this case shows a nearly flat evolution with the pixel size.

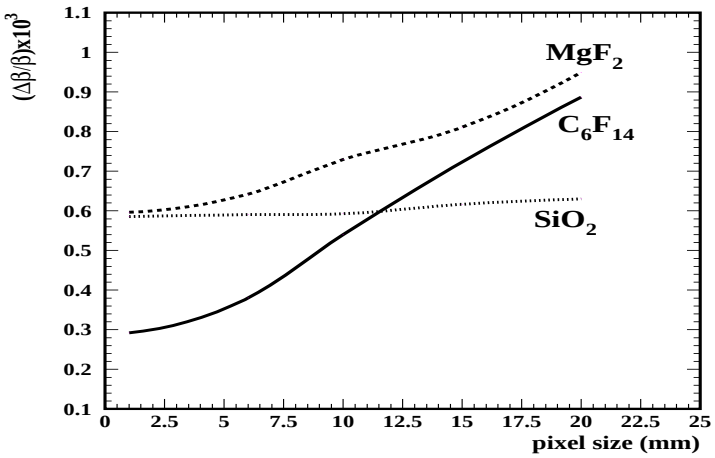

Figure 3.10: *Velocity resolution as a function of the photon detector pixel size. A* ^{96}*Ru projectile at 600 MeV/u was chosen (except for the liquid* C_6F_{14} *radiator, it was 800 MeV/u. All the radiators have a thickness of 2 mm and the photon detector was situated 200 mm away from it.*

Chapter 4

Simulation of key experiments and further improvements.

" He who breaks something has lost the way of wisdom. "

Gandalf to Saruman.

The aim of this chapter is to simulate some representative key experiments which require the use of the Cerenkov detector. These simulations will allow to determine the optimum characteristics of the detector for each case. In particular we are interested in the choice of the nature and thickness of the radiator. As we shown in the second chapter, the atomic interactions of the ions with the radiator will affect the final determination of their magnetic rigidity on the R^3B dipole and their kinetic energy. Consequently, we are interested in a radiator introducing the minimum possible modification of the momentum of the ion produced in the reaction.

For our simulations we have considered three representative experiments which require the identification of heavy ions with the Cerenkov detector. These experiments are: fission investigations with exotic nuclei, spallation reactions and fragmentation reactions with medium mass exotic nuclei. These experiments cover a large range of mass, kinetic energy and different experimental conditions as far as the target thickness is concerned. Consequently we will try to define the optimum radiator for each case.

As we will see, in some cases, the optimum radiator can be obtaining using the radiator in a total internal reflection mode. At the end of the chapter we will discuss the possibilities of this mode as well as possible improvements in the photon detector.

4.1 Fission reactions in inverse kinematics

Recent experiments have demonstrated that fission studies with radioactive beams are a powerful tool to investigate nuclear structure and dynamics [49]. These reactions studied at relativistic energies in inverse kinematics are characterized by the emission of two fission fragments in a back-to back configuration in the center-of-mass frame. The Coulomb repulsion between both fragments leads to the population of a sphere (center-of-mass)/ellipsoid (laboratory) in the velocity space. Consequently the reaction residues cover a large angular and velocity range. These requirements constitute a severe constraints for the dipole design and velocity measurements in order to have a full acceptance for the reaction products. The Cerenkov detector fulfill these conditions since it provides the required resolution in the velocity measurement and a large angular acceptance.

The additional difficulty inherent to these experiments is the fact that the fission residues will generate two rings at the same time in the RICH. Multiple ring patterns are shown in figure 4.1. To determine the ring radii from these events, the same assumption than in the single case has to be made: the ring centers are known. Taking this into account, all the active (x,y) points in the photon detection plane can be projected on two independent radii distributions, respect to both known centers. The results are shown in figure 4.2. With this method, the ion velocity can be determined with a negligible loss of accuracy as compared with a single ring event. However, some problems could appear if the fission is a back-to-back event emission in the beam axis. In this case, both rings would have the same center and patterns as shown in 4.2 would appear. In such cases the determination of the ring radius could be more complicated and could implicate a loss in accuracy.

To discuss these reactions we will take as an example several fragments from the fission reaction of $^{238}U_{92}$. We will analise some typical fission events covering the charge range of fission residues (Z$\sim$30-60):

- $^{238}U \longrightarrow ^{77}Zn + ^{161}Sm$ $\qquad$ $^{238}U \longrightarrow ^{90}Br + ^{148}La$
- $^{238}U \longrightarrow ^{103}Zr + ^{135}Te$ $\qquad$ $^{238}U \longrightarrow ^{116}Rh + ^{122}Ag$

Additionally these cases cover both, symmetric and asymmetric fission events. The energy of the Uranium beam has been chosen to be 600 MeV/u (a typical energy for secondary beam experiments).

The selection of the radiator to be used in the Cerenkov detector will be strongly influenced by the primary interactions of the heavy ions. Since these primary interactions are an important source of velocity uncertainty we have to select a radiator

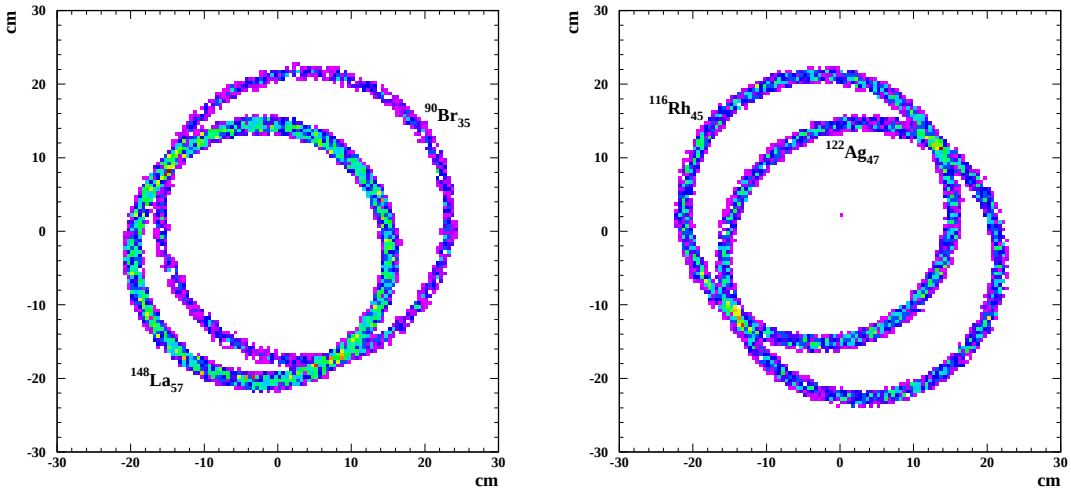

Figure 4.1: *Typical double-ring patterns from fission reactions.* ***(Left)*** *Double ring pattern for the residues* $^{90}Br_{35}$ *and* $^{148}La_{57}$ *out-coming from the fission of* $^{238}U_{92}$ *at 600 MeV/u. This event correspond to an asymmetric fission.* ***(Right)*** *Double ring pattern for the residues* $^{116}Rh_{45}$ *and* $^{122}Ag_{47}$ *out-coming from the fission of* $^{238}U_{92}$ *at 600 MeV/u. This event corresponds to a symmetric fission.*

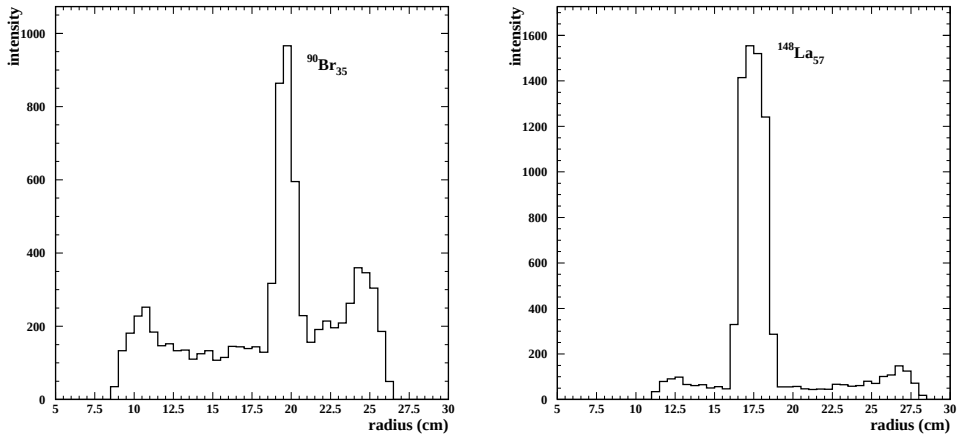

Figure 4.2: ***(Upper part)*** *Double ring pattern for the residues* $^{90}Br_{35}$ *and* $^{148}La_{57}$ *out-coming from the fission of* $^{238}U_{92}$ *at 600 MeV/u.* ***(Lower part)*** *Projected radii for both rings. The ring centers are supposed known in both cases, as can be observed, the photons from one ring are the "tail" in the other ring.*

with low values for energy straggling, angular straggling and nuclear interaction probabilities has to be selected. Additionally, the threshold energy for Cerenkov radiation is a limiting condition to take into account. The primary interactions for

a typical fission residue as $^{96}Ru_{44}$ have been simulated in both, liquid and solid radiators according with the codes described in Chapter 1. The results are shown in table 4.1.

Radiator	Energy loss (MeV/u)	Ω_E (MeV)	Ω_θ (mrad)	Reaction	T_{th} (MeV/u)
$C_6F_{14}(4mm)$	82.3	21.9	1.40	12.6 %	550
$MgF_2(4mm)$	58.8	19.1	1.25	9.5 %	370
$SiO_2(4mm)$	46.2	16.9	1.08	6.9 %	285

Table 4.1: *Simulated primary interaction of a typical fission residue ($^{96}Ru_{44}$). The energy loss, energy straggling (Ω_E), angular straggling (Ω_θ), reaction probability and radiation energy threshold (T_{th}) are shown for several radiators with 4 mm thickness. The 4 mm thickness liquid C_6F_{14} radiator has to be contained in a SiO_2 box with two windows of 2 mm each.*

According to the results shown in table 4.1, the best choice for the radiator to study fission reactions will be a solid SiO_2, not only for the low energy-loss, low energy straggling and low angular straggling values, but also because of the small Cerenkov emission threshold. For fission events we propose a solid SiO_2 radiator of 2 mm thickness working in the Ultra-Violet region of the spectrum with the photon detector situated at 100 mm from the radiator. A thinner radiator will not produce the required velocity resolution due to the low statistic of generated photons (in chapter 3 we concluded that we need at least 100 photons to obtain the velocity from a Cerenkov ring). The thickness of the radiator was chosen to be the one which assures the velocity resolution of 10^{-3} and, simultaneously, induces the minimum primary interactions as possible and the lower reaction probability. The velocity resolution for the residues produced in the fission of ^{208}U is shown in figure 4.3 as a function of the atomic number of the fission residues (upper figure) and their kinetic energy (lower figure). The range in charge covered by fission is indicated by the vertical lines in the upper figure. The energy of the fissioning $^{238}U_{92}$ nuclei was chosen to be a typical one for a secondary beam experiment, 600 MeV/u. We can observe that a 2 mm thickness of SiO_2 radiator provides the required velocity resolution for the fission residues down to an energy of 350 MeV/u. The range in energy for the fission fragments is also shown in figure 4.3, this range comes from the fact that the fragment emission in the center of mass frame in a fission reaction is isotropic, the limit case corresponds with a back-to-back emission in the beam line direction.

Once the radiator has been chosen, we have simulated the primary interactions for the fission residues within the secondary target and within the whole Cerenkov setup. In figure 4.4 we compare the energy-loss and energy straggling of the fission residues within the whole Cerenkov, compared with the energy loss and energy

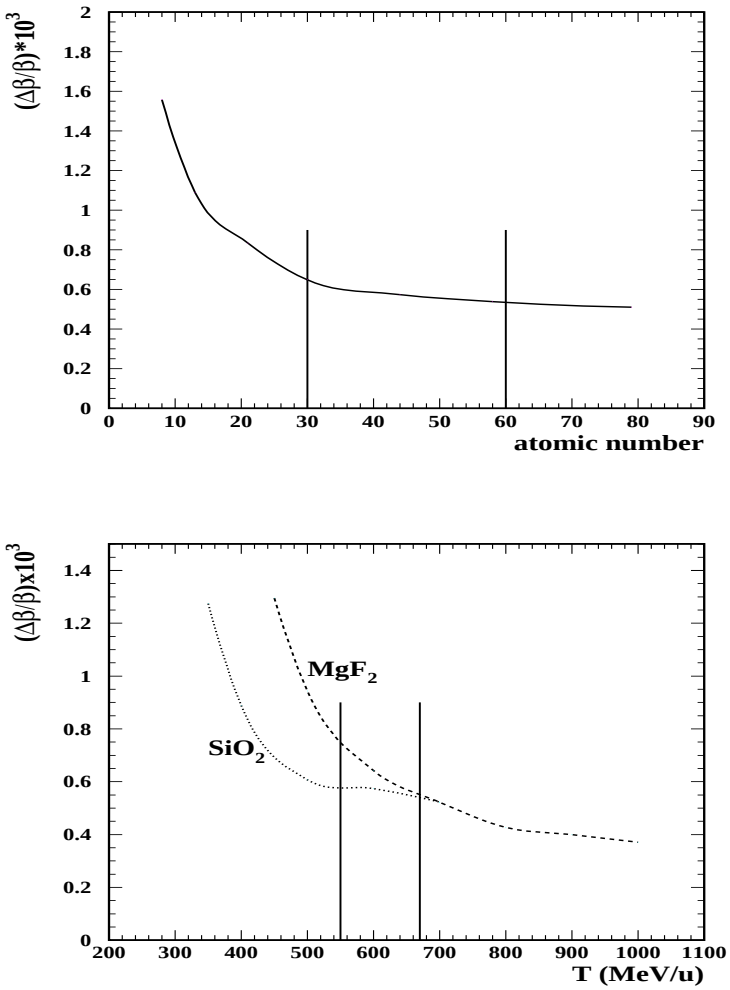

Figure 4.3: ***Upper part:*** *Velocity resolution obtained with a 2 mm thickness SiO_2 radiator as a function of the charge of the projectile. The range in charge covered by fission events is indicated by the vertical lines. The energy of the projectile was chosen to be 600 MeV/u.* ***Bottom picture:*** *velocity resolution as a function of the projectile energy. The projectile is a $^{96}Ru_{44}$ nucleus, chosen to be an intermediate fission residue. Both vertical lines denote the energy range covered by the fission residues. The detection plane is situated 100 mm away from the detector in both cases.*

straggling within the secondary lead target[1] (3 g/cm^2 thickness) are shown respectively. As can be observed in that figure, the energy loss and the energy straggling induced by the radiator are smaller, for all the fission residues, compared to the interactions with the target.

[1] The secondary target is used to induce the electromagnetic fission of the exotic primary beam.

The angular straggling values for the fission residues were also calculated for both the secondary lead target and the Cerenkov setup. The simulated values resulted to be nearly the same for all the fragments, being 0.7 mrad within the Cerenkov matter foils and 2.6 mrad within the secondary lead target.

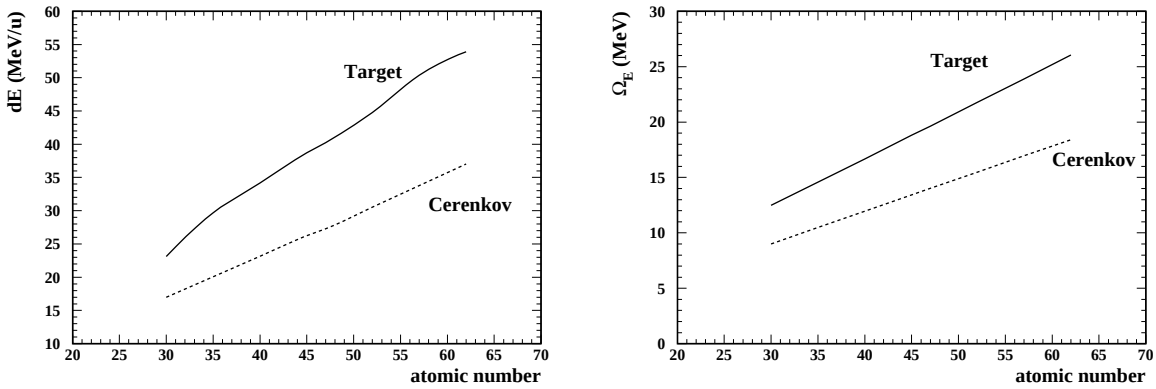

Figure 4.4: ***Left*** *Energy loss for the fission fragments as a function of the fragment atomic number in the target (solid line) and the Cerenkov (dashed line) detector.* ***Right*** *Energy straggling for the fission fragments as a function of the fragment atomic number. The energy-loss and angular straggling in 1.5 g/cm^2 of Lead target is compared with the energy-loss in the whole Cerenkov setup (2 mm SiO_2 radiator, nitrogen expansion gap and mirror).*

The reaction probabilities in this setup due to nuclear interaction and electromagnetic dissotiation were also computed as explained in chapter 2. The results are shown in table 4.2. As can be seen the reaction probabilities for all the nuclides in the Cerenkov detector are lower than 5 % even for the heaviest nuclides. However these values are larger than the reaction rates in the secondary lead target, and consequently, have to be taken into account.

Projectile	Energy	$Reaction_{Cerenkov}$	$Reaction_{Target}$
$^{77}Zn_{30}$	600	3.0 %	2.6 %
$^{103}Zr_{40}$	600	3.5 %	3.0 %
$^{135}Te_{52}$	600	4.0 %	3.5 %
$^{161}Sm_{62}$	600	4.4 %	4.0 %

Table 4.2: *The reaction probability for a 2 mm thickness SiO_2 radiator and for the half of 3 g/cm^2 secondary target thickness.*

The Cerenkov detector will also affect the measurement of the kinetic energy of the fission fragments. As mentioned in chapter 1, to better investigate the reaction

mechanism we need to determine the excitation energy of the fissioning nuclei. For this goal, we should be able to measure the kinetic energies of all the particles has to be measured according to expression:

$$E^{\star} = \sum_i m_i + \sum_i T_i + \sum_i \gamma_i - m_A \tag{4.1}$$

where $E^{\star}$ is the projectile excitation energy, m_A is the projectile mass, m_i and T_i are the mass and kinetic energy of all the particles out-coming the reaction and γ_i is the energy of all the photons produced in the reaction. We are interested now in the measurement of the kinetic energies (T_i) of all the particles involved in the reaction. The kinetic energies for the light particles as protons can be measured with a ToF and the kinetic energies for neutrons will be measured with the LAND detector. The measurement of the kinetic energies for the heavy fission residues will be achieved with the RICH detector. The expression which relates the kinetic energy with the velocity in the laboratory frame is:

$$T = \frac{1}{2}m^2 \left[\left(\frac{v - v_{cm}}{1 - v \cdot v_{cm}/c^2} \right)^2 + \left(\frac{1 - v_{cm}^2/c^2}{1 - v \cdot v_{cm}/c^2} \right)^2 \cdot \gamma^2 \cdot tan^2\theta \cdot v^2 \right] \tag{4.2}$$

where m is the fragment mass and, v is longitudinal velocity in the laboratory frame, v_{cm} is the velocity of the center of mass frame, which correspond to the velocity of the fissioning nuclei. β and γ are also referred to the fissioning nuclei and θ is the angle between the velocity vector of the residue and the beam trajectory. To simulate realistic events, the residue velocity and emission angle were obtained from a fission generator based on the Wilkins expression [50]:

$$TKE = 1.44 \cdot \frac{Z_1 \cdot Z_2}{D} \tag{4.3}$$

with

$$D = r_0 A_1^{1/3} \left(1 + \frac{2\beta_1}{3} \right) + r_0 A_2^{1/3} \left(1 + \frac{2\beta_2}{3} \right) + d \tag{4.4}$$

A_1, A_2, Z_1, Z_2 denote the mass and charge numbers of both fission fragments. The parameters (r_0=1.16 fm, d=2.0 fm and $\beta_1 = \beta_2 = 0.625$) were taken from Refs. [50] and [51]. The Wilkins expression provides the kinetic for both fission fragments

in the center of mass frame, from this we can extract the longitudinal velocity in the laboratory frame needed for expression 4.2.

The primary interactions of heavy ions with matter will influence this measurements because of the energy straggling and angular straggling. The first one will affect the fragment velocity (v) and the second one will affect the particle angle determination (θ) . This effects have to be determined precisely in order to give the uncertainty in the kinetic energy measurements. The energy straggling has to be taking into account in the second half of the secondary target and inside the radiator, however the angular straggling has to be taking into account in the secondary target, the radiator, the nitrogen expansion gap, the mirror, the helium inside the dipole and the position detectors. Keeping this in mind, kinetic energies have been calculated for some typical fission fragments and for two different radiator thicknesses. The results are shown in figure 4.5. The kinetic energy can be determined in both cases with an accuracy better than 20 %. In symmetric fission events, the simulated kinetic energy gives an accuracy better than 15 %. As can be observed, the reduction of the radiator thickness by a factor of 4, does not produce a great improvement in the kinetic energy resolution. This effect can be explained if we consider that the main contribution is due to the angular straggling in the secondary lead target. In addition, as we mentioned in the chapter 3, we need an statistic of 100 photons to assure the validity of the method to reconstruct velocities from the ring radii. This statistic cannot be achieved with 500 μm or 1 mm thickness radiators, this is the reason why we have chosen a 2 mm thickness radiator.

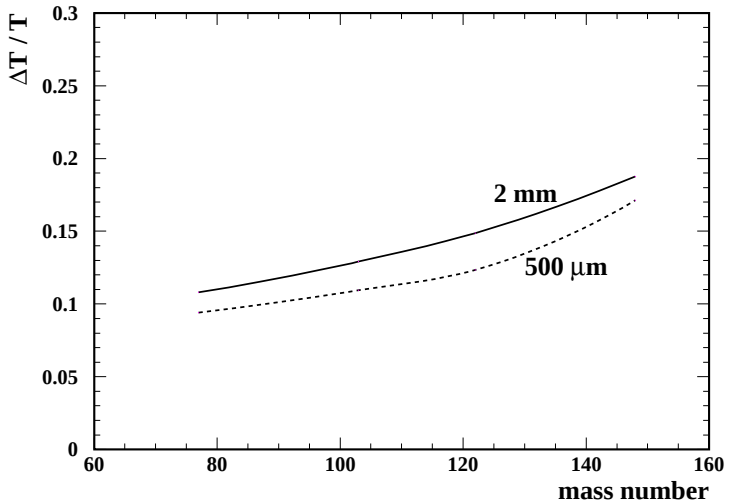

Figure 4.5: *Simulated kinetic energies for several fission residues from $^{238}U_{92}$ at 600 MeV/u. The radiator was chosen to be 2 mm thickness SiO_2.*

4.2 Fragmentation reactions in inverse kinematics.

The R^3B setup is also designed to investigate fragmentation reactions of heavy nuclei in inverse kinematics. These reactions allow to address a large experimental program covering different topics. Between others we can mentione spallation reactions or fragmentation reactions induced by medium-mass exotic nuclei. Many of these experiments require the detection of reactions residues covering a large range in mass and atomic number. However the angular range is smaller when compared with fission reactions.

For our simulations we have chosen three key experiments: spallation reaction induced by ^{208}Pb and ^{56}Fe between 1 GeV/u and 500 MeV/u on a thin liquid hydrogen target, and fragmentation reaction induced by ^{132}Sn at 600 MeV/u on a thick lead target. A typical residue production in spallation reaction is shown in figure 4.6.

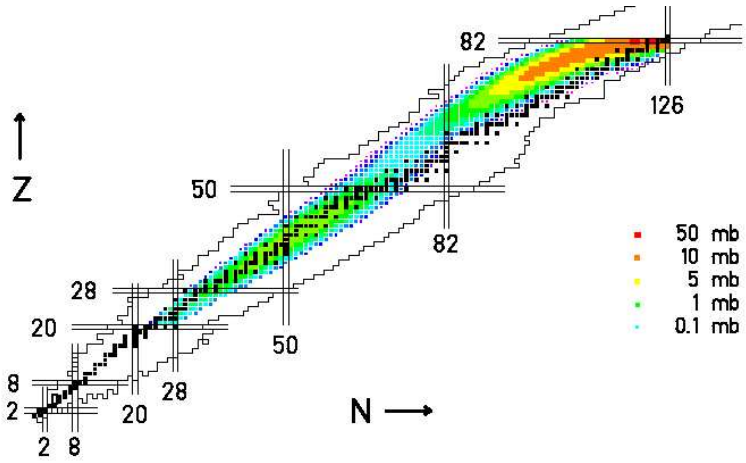

Figure 4.6: *Two-dimensional cluster plot of the isotopic production cross-sections obtained from the reaction ^{208}Pb + p at 1 GeV/u [52]. Full black squares correspond to the stable isotopes. Spallation and fission are separated by a minimum at Z=58.*

In a fragmentation event, the kinetic energy of the fragment can be calculated using the expression:

$$T = \frac{1}{2}m\left(v_{cm}^2 + 3 \cdot \sigma_{cm}^2\right) \tag{4.5}$$

where v is the longitudinal velocity in the laboratory frame, v_{cm} is the projectile

velocity and σ_{cm} is the velocity dispersion in the center of mass frame assumed to be Gaussian. As in the fission case, the primary interaction of heavy ions within the matter foils in the setup will affect the values of v and σ_{cm}. Morrisey systematics[2] [53] allows us to estimate the longitudinal velocity and the velocity dispersion for any spallation fragment. From this we can study how the experimental setup affects the kinetic energy measurements. We will make this study for the two examples written above.

4.2.1 Spallation reaction ^{208}Pb (600 MeV/u) + p

We will consider here the fragments out-coming this reaction with masses down to 150. This corresponds to most of the production, since the cross section of fragments with masses far from the projectile decreases very fast. For this reaction, we will propose the same radiator as in the fission case, 2 mm thickness of solid SiO_2 radiator, with the photon detector situated 100 mm away from the radiator. Other radiators could be used as solid MgF_2 but, as can be seen in figure 4.3 this radiator provides the required velocity only for energies above 500 MeV/u. The target used in this case is a 90 mg/cm^2 of liquid H_2.

The primary interactions for several residues out-coming the reaction were simulated. The residues taken as example were ^{200}Pb,^{190}Hg, ^{180}Ir,^{173}Re,^{160}Yb and ^{147}Tb. These residues were chosen to cover a large range in mass. In figure 4.7 we show the comparison between the energy loss and energy-straggling values within the hydrogen target and the Cerenkov setup. In this case, the energy-loss and the energy straggling values within the Cerenkov setup are larger than those suffered within the secondary target, consequently we can conclude that in spallation studies, the Cerenkov detector has to be taken into account as the higher error source for a later particle identification.

As in the fission cases, the angular straggling was also simulated for the residues produced in the reaction. These simulated values were observed to keep almost the same values for all the residues. These values were 0.11 mrad whiten the secondary hydrogen target and 0.80 mrad whiten the Cerenkov.

The reaction probabilities of the fragmentation residues were also calculated as explained in chapter 2, the results are shown in table 4.3. As can be seen, these reaction rates are always lower than 6 %, but higher in the Cerenkov than in the reaction target.

[2]Those are empirical expressions fit to experimental data from spallation. The expression gives the longitudinal momentum and the momentum dispersion of a spallation fragment.

Projectile	$Reaction_{target}$	$Reaction_{Cerenkov}$
$^{147}Tb_{65}$	3.7 %	4.9 %
$^{160}Yb_{70}$	3.9 %	5.1 %
$^{173}Re_{75}$	4.1 %	5.3 %
$^{180}Ir_{77}$	4.2 %	5.4 %
$^{190}Hg_{80}$	4.4 %	5.5 %
$^{200}Pb_{82}$	4.5 %	5.7 %

Table 4.3: *Reaction probabilities within 45 mg/cm^2 liquid hydrogen target and within 2 mm thickness SiO_2 radiator (502 mg/cm^2) for several fragmentation residues out-coming the reaction $^{208}Pb_{82}$ (600 MeV/u) + p.*

We calculate the kinetic energy of the fragments from expression 4.5. The kinetic energy resolution is shown in figure 4.8. The behavior of this resolution can be explained as follows: the Morrisey systematic gives the longitudinal velocity and its dispersion, this dispersion will be later affected by the experimental setup due to the energy straggling. The dispersion given by Morrisey is higher as larger is the mass difference between the projectile and the fragment and then, the dispersion induced by the Cerenkov matter foils is negligible as compared with those given by Morrisey. The effect of the Cerenkov matter foils can thus be only observed in fragments close to the projectile as deduced from figure 4.8. The kinetic energy uncertainty induced by the setup as always lower than 1 %.

4.2.2 Spallation reaction ^{208}Pb (1 GeV/u) + p

In this case we will study the same residues than in the reaction at 600 MeV/u, analised in section 1.2.1. The used target will be also a 90 mg/cm^2 thickness of liquid hydrogen, but, in this case we cannot use the solid SiO_2 radiator due the energy acceptance of this radiator. From energies above 750 MeV/u, no photon will exit the radiator due to total internal reflection. From this, we conclude that we must use a different radiator as could be the solid MgF_2 or introduce a new method to achieve the measurement of the ion velocity from a radiator working in internal reflection mode. This will be introduced in the next section. We will choose both radiators, solid MgF_2 working in normal mode and solid SiO_2 working in total internal reflection mode (this working mode will be explained in the next section). Due to the charge of the residues, 2 mm thickness for both radiators is sufficient to assure enough photon statistic to obtain the ion velocity with the required accuracy. The photon detector was situated 100 mm away from the radiator.

The primary interactions of selected residues within the Cerenkov setup were

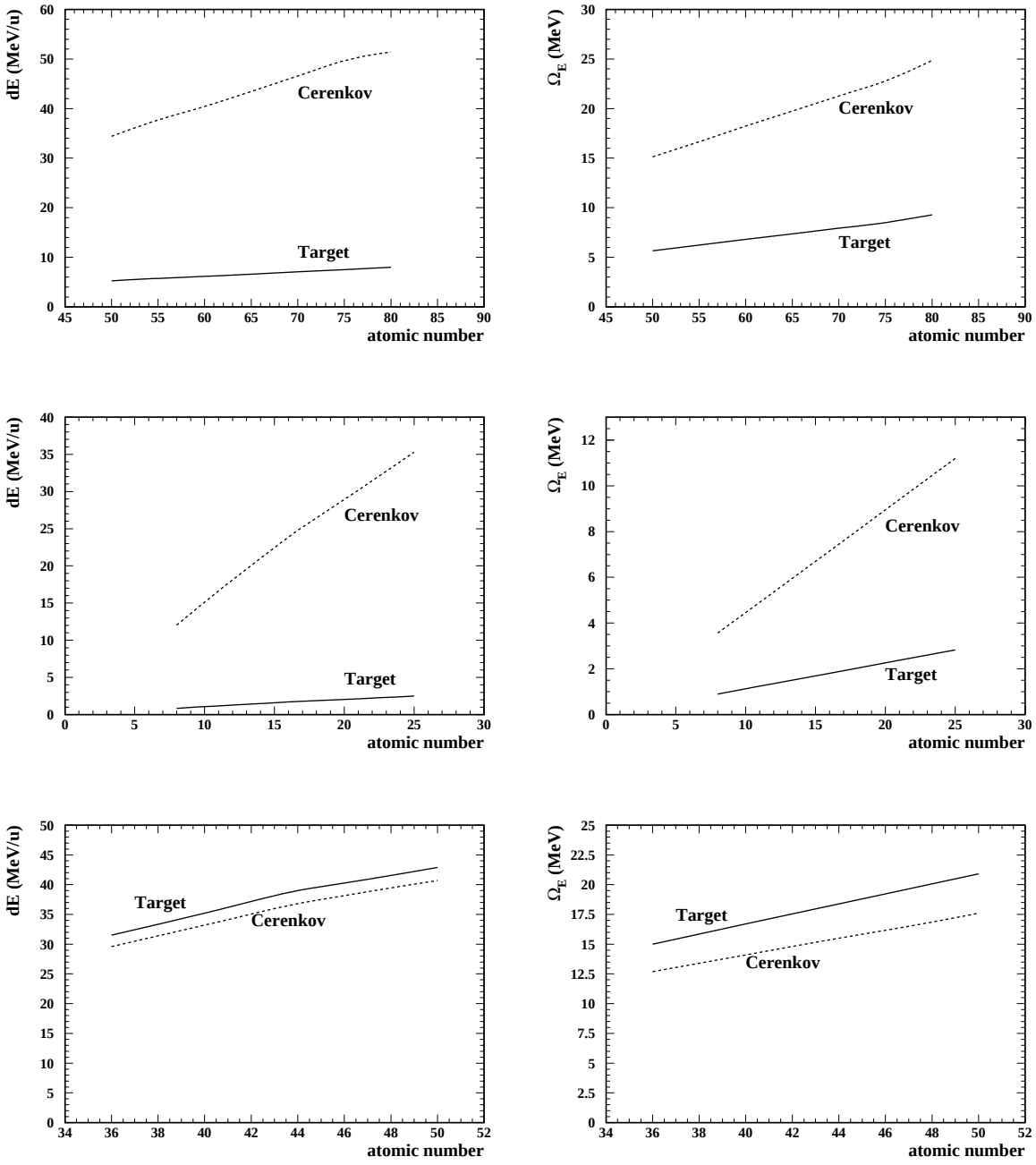

Figure 4.7: *Simulated values of the energy loss (left) and energy straggling (right) with the Cerenkov matter foils (dashed line) and with the secondary target (solid line). The upper part correspond to the reaction ^{208}Pb (600 MeV/u) + p, the middle part corresponds to the reaction ^{56}Fe (600 MeV/u) + p and the bottom part corresponds to the reaction ^{132}Sn (600 MeV/u) + Pb.*

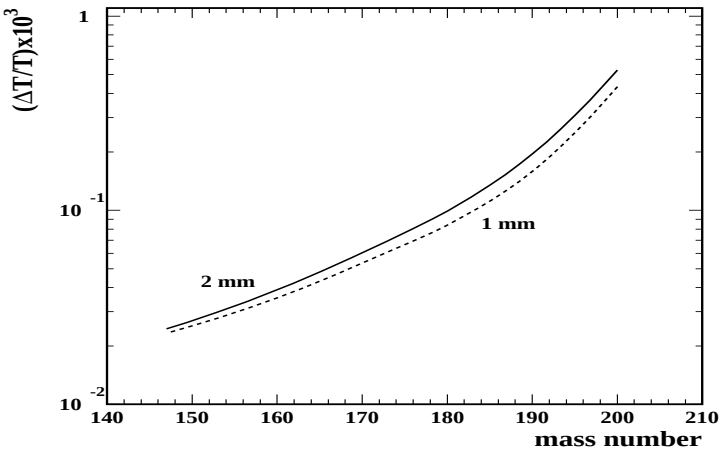

Figure 4.8: *Kinetic energy resolution for the residues produced in the spallation of the ^{208}Pb nuclei. The kinetic energy resolution has been simulated for two radiator thicknesses, 1 mm (dashed line) and 2 mm (solid line).The influence of the Cerenkov matter foils in the kinetic energy resolution can be observed only for fragments close to the projectile.*

calculated and are shown in figure 4.9. As can be observed, the effect is the same than in other spallation reactions, the most important source of energy loss and energy straggling is the Cerenkov setup. The angular straggling values were simulated for all the residues taken into account within both radiators, these values were observed to keep nearly constant for all the fragments. The angular straggling induced by the secondary target was 0.07 mrad. The angular straggling induced by the Cerenkov setup was 0.54 mrad for the MgF_2 radiator and 0.45 mrad for the SiO_2 radiator.

The reaction probabilities of the selected residues in the Cerenkov matter foils and in the secondary target were also calculated as explained in chapter 2. The obtained values are shown in table 4.4

The kinetic energies of the fragments have been calculated as indicated in expression 1.5. The kinetic energy resolution for the selected residues is shown in figure 4.10. As can be observed, the relative difference between Morrisey and simulated predictions is always better than 1 %. This resolution is slightly better for the SiO_2 radiator due to the lower primary interactions values of the ions with this radiator. As can be observed in that figure the relative differences in kinetic energy are larger as closer to the projectile mass.

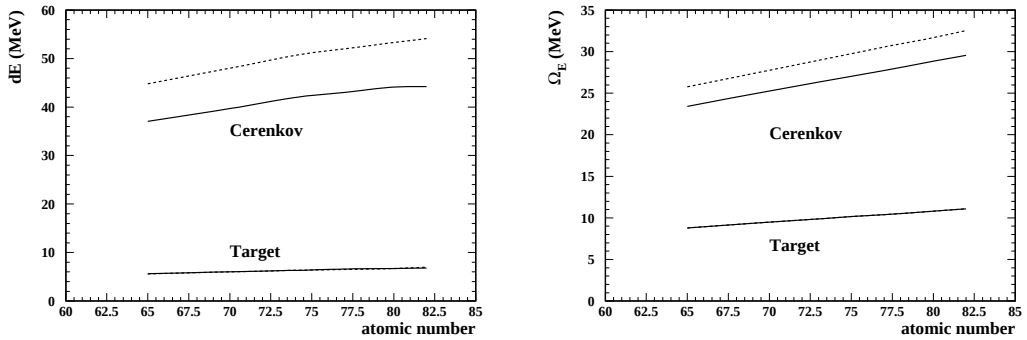

Figure 4.9: *Simulated values of the energy loss (left) and energy straggling (right) with the secondary target and with the Cerenkov matter foils for two different radiators: solid MgF_2 (dashed line) and solid SiO_2 working in total internal reflection mode (solid line).*

Projectile	$Reaction_{target}$	$Reaction_{MgF_2}$	$Reaction_{SiO_2}$
$^{147}Tb_{65}$	3.7 %	6.1 %	5.1 %
$^{160}Yb_{70}$	4.0 %	6.2 %	5.3 %
$^{173}Re_{75}$	4.2 %	6.6 %	5.5 %
$^{180}Ir_{77}$	4.4 %	6.7 %	5.6 %
$^{190}Hg_{80}$	4.5 %	6.8 %	5.7 %
$^{200}Pb_{82}$	4.7 %	7.0 %	5.9 %

Table 4.4: *Reaction probabilities within 1.5 g/cm^2 lead target and within 3 mm thickness SiO_2 radiator (753 mg/cm^2) for several fragmentation residues out-coming the reaction ^{132}Sn (600 MeV/u) + Pb.*

4.2.3 Spallation reaction ^{56}Fe (600 MeV/u) + p

In this case, the fragments have a lower charge than in the ^{208}Pb fragmentation. The number of photons generated in 2 mm of SiO_2 is not enough to apply our method to extract the ion velocity from the ring radius. We will propose then a new radiator, 5 mm thickness of solid SiO_2 radiator, with the light detector situated 100 mm away from the radiator. The velocity resolution of 10^{-3} is not necessary for these light fragments. Making and analog development as made in chapter 1 to obtain the needed accuracy in velocity we get that, in order to separate the nuclei ^{56}Fe from its neighbor ^{55}Fe, a precision of 6×10^{-3} is sufficient. If we want to develop experiments at energies close to 1GeV/u we have to use the solid SiO_2 radiator working in total internal reflection mode or use a solid MgF_2 radiator with 3 mm thickness.

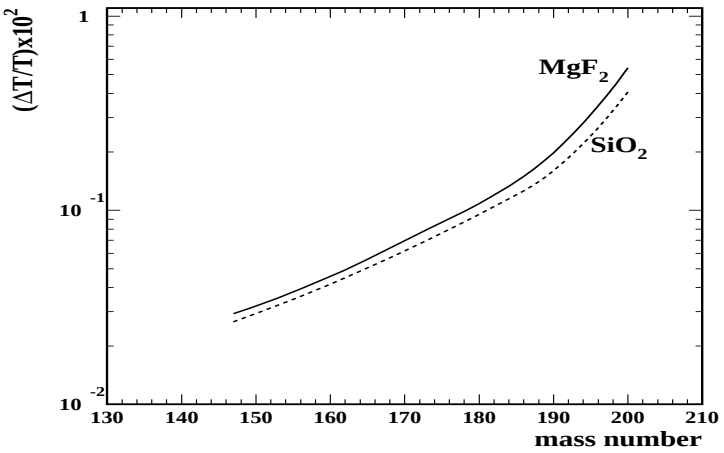

Figure 4.10: *Kinetic energy resolution for the residues produced in the spallation of the ^{208}Pb nuclei at 1 GeV/u. The kinetic energy resolution has been simulated for two radiators: solid MgF_2 (solid line) and solid SiO_2 working in total internal reflection mode (dashed line).*

The primary interactions for these fragments whit the experimental setup were also calculated and are shown in figure 4.7. As can be observed in that figure, the effect is the same than in the spallation of the ^{208}Pb, the influence of the reaction target is negligible as compared with those suffered in the Cerenkov setup.

The reaction probabilities for all the residues in the Cerenkov matter foils and in the secondary hydrogen target were also calculated as explained in chapter 2, the obtained values are shown in table 4.5. As can be seen in this table, the reaction rates are always lower than 8 %, but higher in the Cerenkov than in the reaction target.

Projectile	$Reaction_{target}$	$Reaction_{Cerenkov}$
$^{55}Mn_{25}$	1.9 %	7.3 %
$^{45}Sc_{21}$	1.6 %	6.9 %
$^{35}Cl_{17}$	1.3 %	6.2 %
$^{25}Mg_{12}$	1.1 %	5.5 %
$^{16}O_8$	0.8 %	4.8 %

Table 4.5: *Reaction probabilities within 45 mg/cm^2 liquid hydrogen target and within 5 mm thickness SiO_2 radiator (1255 mg/cm^2) for several fragmentation residues out-coming the reaction ^{56}Fe (600 MeV/u) + p.*

The kinetic energy of the fragments have been calculated following expression

4.5. The kinetic energy resolution for the residues is shown in figure 4.11. As can be observed, the relative difference between Morrisey and simulated predictions is always smaller than 1 %. This difference, as in the spallation of the ^{208}Pb nuclei, becomes negligible for fragments far from the projectile for the reasons already discussed and the influence of the matter foils of the Cerenkov detector increases for fragments close to the projectile.

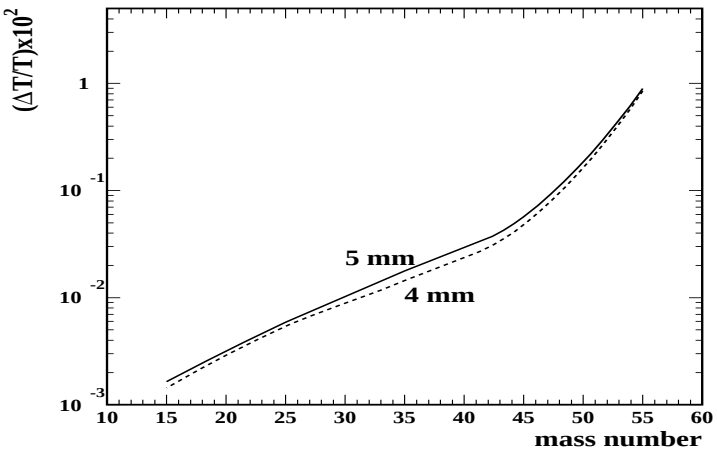

Figure 4.11: *Kinetic energy resolution for the residues produced in the spallation of the ^{56}Fe nuclei. The kinetic energy resolution has been simulated for two radiator thicknesses, 5 mm (dashed line) and 4 mm (solid line). The influence of the Cerenkov matter foils in the kinetic energy resolution can be observed only for fragments close to the projectile.*

4.2.4 Fragmentation reaction of medium-mass exotic nuclei ^{132}Sn (600 MeV/u) + Pb

In this case we will study the residues from a fragmentation reaction induced by a thick target. We will study the fragmentation of the doubly magic ^{132}Sn. The selection of the radiator thickness and nature is given by the same considerations than in the last cases. We can not use the solid MgF_2 radiator because it provides the required accuracy only for fragments with energies above 500 MeV/u. We should use then the solid SiO_2 radiator. The thickness of this radiator has to be fixed to that which provides enough number of photons even for the lighter fragments. For this reason the thickness was chosen to be 3 mm. The photon detector is situated at 100 mm from the radiator. The target used in this case has been a 3 g/cm^2 ^{208}Pb. With this reaction we expect to study the influence of a heavy secondary target in the kinetic energy resolution of the residues from the reaction.

The primary interactions for several residues out-coming the reaction were simulated. The residues taken as example were ^{130}Sn, ^{120}Ag, ^{110}Ru, ^{100}Zr, ^{90}Kr. In figure 4.7 we show the comparison between the energy loss and energy straggling values within the lead target and the Cerenkov setup. In this case, the values calculated for the lead target are comparable to those calculated for the Cerenkov setup, this should lead to an effective loss in the accuracy to determine the kinetic energy of the residues. As above, the angular straggling was also simulated for these residues and these values were observed to keep almost the same values for all the residues. These values were 0.90 mrad within the Cerenkov setup and 2.65 mrad within the lead secondary target.

The reaction probabilities of the residues in the Cerenkov matter and in the secondary target were also calculated as explained in chapter 2, the obtained values are shown in table 4.6. As can be observed, the reaction rates are always lower than 6 %, but higher in the Cerenkov than in the reaction target.

Projectile	$Reaction_{target}$	$Reaction_{Cerenkov}$
$^{130}Sn_{50}$	3.4 %	6.0 %
$^{120}Ag_{47}$	3.3 %	5.8 %
$^{110}Ru_{44}$	3.1 %	5.6 %
$^{100}Zr_{40}$	2.9 %	5.4 %
$^{90}Kr_{36}$	2.8 %	5.1 %

Table 4.6: *Reaction probabilities within 1.5 g/cm^2 lead target and within 3 mm thickness SiO_2 radiator (753 mg/cm^2) for several fragmentation residues out-coming the reaction ^{132}Sn (600 MeV/u) + Pb.*

We have calculated the kinetic energy resolution of the residues from expression 4.5. The results are shown in figure 4.12. As we expected, the nature of the secondary target has a large influence in the kinetic energy resolution. The resolution for fragments close to the projectile reach the 4 %, notably larger than those cases where the secondary target is hydrogen. It can be also observed in the figure 4.12 that the most important influence to the kinetic energy resolution is the energy straggling in the secondary lead target, this resolution is shown in that figure for two different thickness of the radiator. Both cases give to similar kinetic energy resolutions.

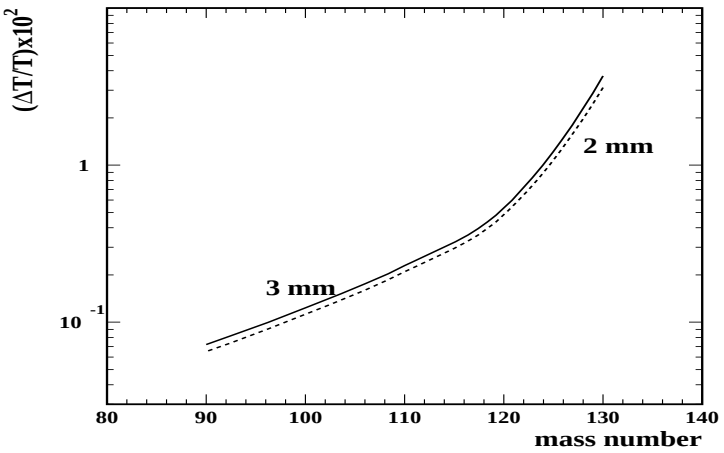

Figure 4.12: *Kinetic energy resolution for the residues produced in the spallation of the ^{132}Sn nuclei. The kinetic energy resolution has been simulated for two radiator thicknesses for SiO_2, 4 mm (dashed line) and 3 mm (solid line).The influence of the Cerenkov matter foils in the kinetic energy resolution can be observed only for fragments close to the projectile.*

4.3 Total Internal Reflection Mode

In the last section we have used the solid SiO_2 radiator working in total internal reflection mode in the simulation of the spallation reaction $^{208}Pb + p$ at 1 GeV/u. In this section we will introduce the total internal reflection mode.

In the Chapter 3, we used a expression to get the velocity uncertainty from the measurement of the ring radius (equation 3.6). The Snellius law was needed to obtain that expression (see Appendix E). In that case, we disgard the possibility when the law of refraction $sin\theta_1 = \frac{n_2}{n_1} sin\theta_2$ does not give a real value for the angle of refraction θ_2. We will now examine this case. It occurs when light is propagated from an optical medium into one which is optically less dense, i.e, when $\frac{n_2}{n_1} < 1$ provided that the angle of incidence θ_1 exceeds the critical value $\bar{\theta}_1$ given by:

$$sin\bar{\theta}_1 = \frac{n_2}{n_1} \tag{4.6}$$

When $\theta_1 = \bar{\theta}_1$ the light emerges in a direction tangent to the boundary. If θ_1 exceeds that limiting value, no light enters the second medium, being reflected into the first medium and we speak of total reflection. We will take advantage of this

effect in order to use a radiator working in this mode. The interest of working in this mode is to extend the energy range of the SiO_2 radiator which, as we mentioned, can be used in the range between 300 MeV/u and 700 MeV/u. With this use of the radiator, the energy range can be extended to any desired energy.

We will simulate a radiator with a truncated cone shape in order to allow the photons exit the radiator from the side. In figure 4.13 we can observe the operation mode of this kind of radiators, the Cerenkov emitted photons are reflected continuously until the radiator tilted edge. The radiator edge is profiled so that the light is not reflected again when reaching the it due to the tilt angle and is able to escape from the radiator at that point (see figure 4.13). Operating in this way, at the light detector plane a ring is also observed. The principal difference of this mode is that the Cerenkov emission angle is determined from the expression:

$$\theta_C = \arctan\left(\frac{d}{r_1 - r_2}\right) - \arcsin\left[\frac{n_2}{n_1}\left(\sin\left[\arctan\left(\frac{d}{r_1 - r_2}\right) - \arctan\left(\frac{R - \bar{r}}{L}\right)\right]\right)\right] \tag{4.7}$$

where R is the ring radius, $\bar{r}$ is the mean radiator radius, L is the distance from the radiator to the detector, r_1 and r_2 are the bottom and top radii of the radiator, respectively, d is its thickness, n_1 and n_2 the refractive index of the radiator and the expansion gap medium respectively. For the derivation of this equation see Appendix E.

The choice of the radiator material depends on the incident particle energy range wanted to be detected, that is, depending on the refractive index the critical angle given by expression 4.6 takes different values. We calculated the energy threshold to operate on internal reflection mode for the typical materials we have used up to now to compose the radiators. The results are shown in table 4.7

According to the calculated values shown in table 4.7 and taking into account the energy range we want to detect for fission and fragmentation (up to 700 MeV/u approx.) the only possible choice is the solid SiO_2 radiator. In figure 4.14 we can observe the results of the simulations made for an $^{36}Ar_{18}$ nuclei as a function of the kinetic energy. The resolution improves as higher is the projectile energy, as expected, but is can be observed that the velocity resolution is worse than in a direct detection not based on the internal reflection effect.

One problem of this operation mode is the photon losses at the radiator edge due to the photons incidence angle. Every photon which reach the edge from "up" to "down" will not be able to exit the radiator (see figure 4.15). This problem could be avoided with a more complicated shape (see figure 4.15), of course, this would

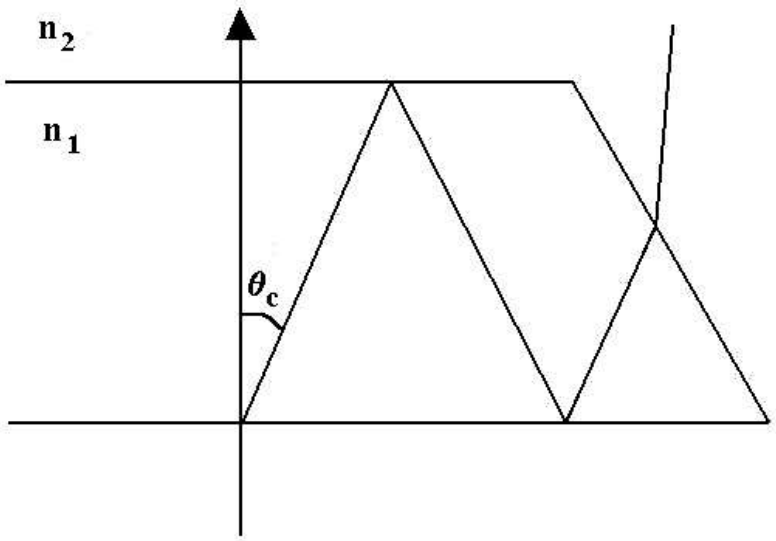

Figure 4.13: *Operation mode of a total internal reflection radiator. The photons generated by the heavy ion passing through the radiator go rebounding by total reflection till the edge.*

Material	$\bar{n}$	$\theta_{th}(degrees)$	β	T (MeV/u)
C_6F_{14}	1.2862	51.1	> 1.0	$\nexists$
MgF_2	1.4263	44.8	0.984	4300
SiO_2	1.557	40.2	0.841	790

Table 4.7: *Energy thresholds to work in total reflection mode for typical radiator materials. $\bar{n}$ is the mean refractive index in the wavelength operation range, θ_{th} is the critical Cerenkov emission angle and β and T are the threshold velocity and energy of the incident particle, respectively. For our intentions we will choose the solid SiO_2 radiator due to the energy range we want to study. Notice that for the liquid C_6F_{14} radiator there is no exists internal reflection.*

translate in a more expensive cost for the radiator.

4.4 Alternative RICH photon detectors

As we mentioned in Chapter 3, no simulation was made about the photon detector in the HIRICH. Every photon reaching the detection plane was supposed to be detected in the simulation and the detection quantum efficiency was imposed "a

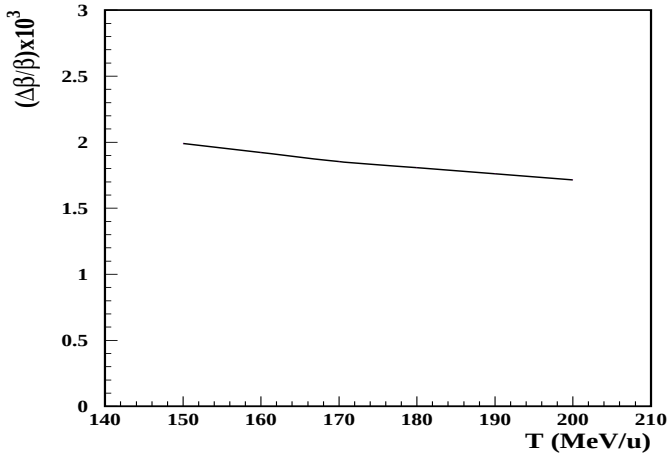

Figure 4.14: *Simulated velocity resolution for a radiator working in total internal reflection mode for a radiator thickness of cm and a projectile of* ^{96}Ru.

priori" in the tracking (see figure 3.3 in Chapter 3). In this section we will discuss about the possibility of optimize this detection plane with different kinds of photon detectors.

A great improvement for the Cerenkov detector would be the implementation of new photon detectors with a higher quantum detection efficiency in the range of the spectrum we are working. For this goal we will suggest photon detectors of recent development as Hybrid Photon Detector (HPD) and Micro-Avalanche Photo Diodes (μAPD).

Hybrid Photon Detectors (HPDs) combine in a single device vacuum photo-cathode technology with solid-state technology. A photo-electron, released from the conversion in a photo-cathode of an incident photon, is accelerated by an applied high voltage of 12 to 20 kV onto a reverse-biased silicon detector. This kinetic energy is then dissipated near the silicon surface, which results in the creation of 3000 to 5000 electron-hole pairs. Peak quantum efficiencies achieved with these detectors reach 30 % at 200 nm wavelength. The light pattern incident on the photo-cathode is imaged onto the silicon detector by an electrostatic or proximity-focusing electron optics with collection efficiencies close to 100 %. One disadvantage of these detectors is that the electron focusing cannot work near a magnetic field.

Avalanche Photo-Diodes (APDs) An avalanche photodiode is a silicon-based semiconductor containing a p-n junction consisting of a positively doped p region and a negatively doped n region sandwiching an area of neutral charge called the depletion region. These diodes provide gain by the generation of electron-hole pairs

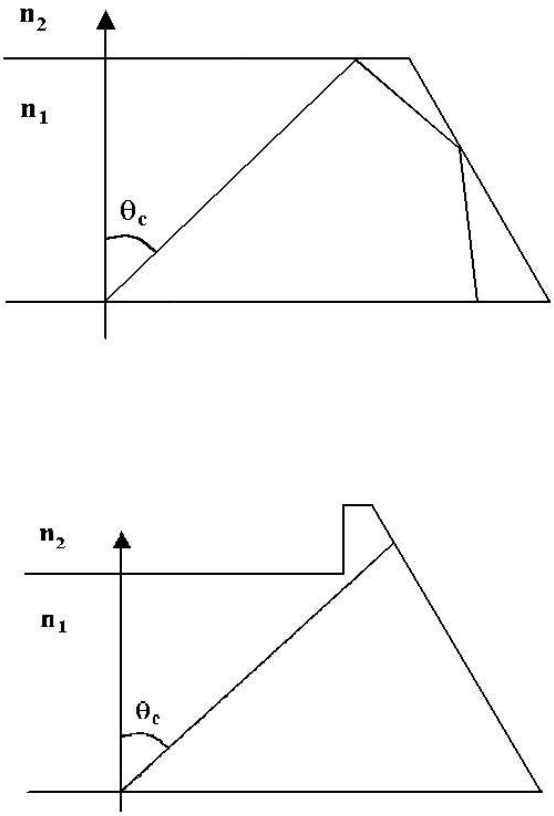

Figure 4.15: *Photon intensity loss at the edge of the radiator due to the photon incident angle (top part). This problem can be avoided with a new radiator shape (bottom part).*

from an energetic electron that creates an "avalanche" of electrons in the substrate due to multiple collisions with the crystalline silicon lattice. This "avalanche" of electrons eventually results in electron multiplication that is analogous to the process occurring in one of the dynodes of a photomultiplier tube. These detectors are compact and immune to magnetic fields, are difficult to overload, and have a high quantum efficiency that can reach 90 % at 200 nm.

These detectors would improve the detection quantum efficiency in the Ultra-Violet range of the spectrum. This effect will lead to a higher number of detected photons, highly improving the resolution on the velocity measurements. This would allow to reduce the radiator thickness, avoiding effects relationated with energy-loss, energy-straggling, angular-straggling and transmission probabilities, improving then the later identification with the spectrometer. The implementation of such kind of detectors could be a subject of further studies in the close future.

Conclusions

" In the end, one really has to do everything oneself in order to be on top of the things; so, there is a lot of work to be done."

Friedrich Nietzche.

The goal of this work was to simulate and optimize a Heavy Ion Ring Imaging Cerenkov Detector (HIRICH). This detector will be used to measure the velocities of heavy ions within the frame of the R^3B project, that will take place at GSI-Darmstadt (Germany) in a close future. The simulations of the Cerenkov detector were made with the code GEANT 3.21 because of the adecuated frame of this code. GEANT 3.21, developed at CERN, is well suited to simulate the detector setup proposed for R^3B. This is a powerful Monte-Carlo code which allows to describe the geometry of the detector, to track the particles through the different layers of matter, to describe the atomic interactions of these particles and to simulate the generation and propagation of Cerenkov radiation.

Since the Cerenkov detector (radiator + mirror) represents a non negligible layer of matter traversed by the ions in the R^3B setup, the final identification of these ions can suffer from their interactions with these layers of matter. To investigate this problematic we analised systematically the primary interactions of ions with matter, mainly: energy loss, energy straggling and angular straggling. We investigated several codes in order to determine the most realistic description of these interactions. These codes were ATIMA, AMADEUS, GEANT 3.21 and SRIM 2000. From these studies we concluded that the codes SRIM 2000 and GEANT 3.21 are not suited to compute energy losses and energy straggling for heavy ions in the energy range that we are interested. Consequently, GEANT 3.21 had to be modified and external subroutines were implemented for this goal. In contrast, the angular straggling values provided by GEANT 3.21 were in a good agreement with the experimental data. The reaction probabilities within the setup were also studied taking into account the cross sections for nuclear interaction and electromagnetic dissotiation.

The code GEANT 3.21 provides several internal packages for the treatment of

Cerenkov radiation. These packages allow to make the tracking of Cerenkov photons through the experimental setup, taking into account transmission effects, the dispersion law of the radiator, etc. A complete simulation of a Cerenkov detector was made taking into account these parameters. The response of the photon detector was also simulated by introducing in the code the detection quantum efficiency and the detector granularity. A comprehensive analysis of the performances of different radiators was made by changing several technical aspects of three radiators: liquid C_6F_{14}, solid MgF_2 and solid SiO_2. These systematic simulations were developed for the considered radiators as a function of the charge of the incoming ion, its kinetic energy, the radiator thickness and the photon detector granularity. It was observed that the velocity resolution improves with the charge of the incoming ion but, at charges higher than Z=25-30 this improvement is compensated by the energy loss in the radiator. The velocity resolution also improves with the kinetic energy of the incoming ion due to the higher number of emitted photons and the lower energy loss in the radiator. The expected improvement in the velocity resolution with the radiator thickness due to the enhancement of the photon emission was observed to be not only compensated, but even dominated by the energy loss in the radiator and the dispersion law. The effect of the granularity of the photon detector was observed from the simulations to be a non-determinant factor in the velocity resolution.

The last part of this work was dedicated to the simulation of some hey experiments in order to choose the best option for the nature and thickness of the radiator to achieve the required velocity resolution, but minimizing the nuclear and atomic interactions. Some representative cases were selected: the fission of ^{238}U at 600 MeV/u, the spallations ^{56}Fe + p 600 MeV/u, ^{208}Pb + p 1 GeV/u and the fragmentation ^{132}Sn + Pb 600 MeV/u in inverse kinematics.

In fission reactions we had to deal with multiple-ring pattern events due to the simultaneously emission of both fission residues. The atomic and nuclear interactions of some representative residues passing through the different radiators were compared with those suffered in the secondary target in order to choose the best option for the radiator. These interaction rates together with the energy range of the different radiators was used to determine the optimum radiator. The solid MgF_2 radiator provides the required velocity accuracy only for energies above 500 MeV/u. Due to the energy range covered by the fission fragments, the reaction could give residues with an energy below 500 MeV/u or fission experiments at lower energies than 600 MeV/u could be developed and then the achieved resolution will not be sufficient to identify them with the MgF_2 radiator. For these reasons, finally it was proposed, for fission studies, a 2 mm thickness solid SiO_2 radiator. The kinetic energy uncertainty induced by the setup was also simulated. We concluded that this uncertainty depends mostly on the atomic interactions in the lead target. The selection of the radiator thus, will not strongly affect the accuracy in the kinetic energy measurements.

In spallation reactions the same features than in the fission case were simulated for different reactions. The selection of the radiator was given by the same considerations than in the fission case, the reaction rates and the energy range of the reaction residues. At low energies the proposed radiators were: 2 mm thickness of solid SiO_2 for the spallation of the ^{208}Pb nuclei, and 5 mm thickness of solid SiO_2 radiator for the spallation of the ^{56}Fe nuclei due to the lower charge of the spallation residues. At higher energies, for the spallation of the ^{208}Pb nuclei at 1 GeV/u two radiators were proposed: a 2 mm thickness solid MgF_2 or a 2 mm thickness solid SiO_2 radiator, but working in total internal reflection mode. The discussion of this operation mode was also developed in the last chapter of this work. The uncertainty in the kinetic energy induced by the matter foils in the setup was also simulated for typical spallation residues of each reaction. In this case, the influence of the secondary hydrogen target in the kinetic energy determination is negligible compared with the uncertainty induced by the Cerenkov radiator.

The same simulations were done in the case of the fragmentation of the ^{132}Sn in a heavy target. In this case the proposed radiator was a 3 mm thickness solid SiO_2 radiator in order to get a high velocity resolution even for the lightest residues from this reaction. The uncertainty in the kinetic energy measurements induced by the Cerenkov matter foils was simulated as in the previous cases. The atomic interactions of the fragmentation residues in the secondary lead target were also the main uncertainty sources as in the fission case. Consequently, the resolution in this measurement will not be highly conditioned by the radiator selection.

Finally we over viewed new photon detectors of recent development in order to discuss possible the improvements in the velocity resolution with the implementation of these new detectors.

Appendix A

Algorithm for energy-loss calculations used in the code AMADEUS

In the second Chapter we have described how several codes under study cimputed the energy losses for heavy ions. In this appendix the method used by the code AMADEUS is explained in detail.

The basic idea was to parameterise the range of ions in any material by using an analytical function that can be inverted. Then the energy loss in a layer of matter with thickness d can be obtained as:

$$\Delta E(d) = E_i - E_f \tag{A.1}$$

where E_i is the initial energy of the ion and E_f is the remaining energy of the ion after traversing the layer of matter that can easily be calculated from the residual ranges before and behind the layer, $r(E_i)$ and $r(E_f)$, since

$$r(E_f) = r(E_i) - d \tag{A.2}$$

and the function $r(E)$ can be inverted.

To determine the function $r(E)$, first we calculated the range of a number of different projectile-stopper combinations by numerical integration of the stopping-power expressions presented in the appendix of Ref. [7]. Then we fitted the values

Table A.1: Parameters p_1 to p_{10} which provide the range of any ion with energy between 100 and 200 A MeV in Be, C and Al according to the expression A.3.

in Be (Z = 4)	in C (Z = 6)	in Al (Z = 13)
$p_1 = -1.28428 \cdot 10^{-4}$	$6.67801 \cdot 10^{-4}$	$-6.68659 \cdot 10^{-5}$
$p_2 = -1.73612 \cdot 10^{-6}$	$-3.92137 \cdot 10^{-6}$	$-1.85311 \cdot 10^{-6}$
$p_3 = 8.89892 \cdot 10^{-8}$	$1.36917 \cdot 10^{-7}$	$8.73192 \cdot 10^{-8}$
$p_4 = -7.05115 \cdot 10^{-10}$	$-9.72996 \cdot 10^{-10}$	$-6.90141 \cdot 10^{-10}$
$p_5 = -0.553492$	-0.490202	-0.530758
$p_6 = 9.12049 \cdot 10^{-3}$	$7.51599 \cdot 10^{-3}$	$8.98953 \cdot 10^{-3}$
$p_7 = 2.68184$	2.61390	2.68916
$p_8 = -0.210108 \cdot 10^{-3}$	$-6.00822 \cdot 10^{-3}$	$-5.33772 \cdot 10^{-3}$
$p_9 = 7.74360 \cdot 10^{-4}$	$-0.199549 \cdot 10^{-4}$	-0.214131
$p_{10} = -1.28428 \cdot 10^{-4}$	$7.31880 \cdot 10^{-4}$	$7.73008 \cdot 10^{-4}$

in an energy range between 100 A MeV and 2 A GeV with the least squares method to the function:

$$r(Z_p, A_p, E/A_p) = k \, \frac{A_p}{Z_p^2} \, 10^{\kappa} \qquad mg/cm^2 \tag{A.3}$$

where

$$\begin{aligned} \kappa = (1 + p_1 Z_p + p_2 Z_p^2 + p_3 Z_p^3 + p_4 Z_p^4) \cdot [(p_5 + p_6 Z_p) \\ + (p_7 + p_8 Z_p) log_{10}(E/A_p) + (p_9 + p_{10} Z_p) log_{10}^2(E/A_p)] \end{aligned} \tag{A.4}$$

with A_p and Z_p the mass and atomic number of the ion, respectively, and E/A_p its energy in A MeV.

The set of parameters p_1 to p_{10} resulting from the fit are listed in table A.1 for Be, C and Al and in table A.2 for Sn, Ta and Pb. The different sets of parameters were adjusted separately to each stopper material but simultaneously for 21 projectiles from $Z_p = 3$ to $Z_p = 92$ and for all energies between E/A = 100 MeV and 2 GeV.

The factor k in equation A.3 allows to interpolate the calculation of the range

Table A.2: Parameters p_1 to p_{10} which provide the range of any ion with energy between 100 and 200 A MeV in Sn, Ta and Pb according to the expression A.3.

in Sn (Z = 50)	in Ta (Z = 73)	in Pb (Z = 82)
$p_1 = 1.23639 \cdot 10^{-3}$	$-1.99249 \cdot 10^{-5}$	$-3.75861 \cdot 10^{-4}$
$p_2 = -6.13893 \cdot 10^{-6}$	$-2.27944 \cdot 10^{-6}$	$-3.73902 \cdot 10^{-6}$
$p_3 = 1.84116 \cdot 10^{-7}$	$1.05063 \cdot 10^{-7}$	$1.48861 \cdot 10^{-7}$
$p_4 = -1.20551 \cdot 10^{-9}$	$-8.29122 \cdot 10^{-10}$	$-1.12159 \cdot 10^{-9}$
$p_5 = -0.263421$	-0.325062	-0.166220
$p_6 = 6.34349 \cdot 10^{-3}$	$9.75017 \cdot 10^{-3}$	$1.26920 \cdot 10^{-2}$
$p_7 = 2.61081$	2.68814	2.59061
$p_8 = -6.38315 \cdot 10^{-3}$	$-6.07419 \cdot 10^{-3}$	$-7.25322 \cdot 10^{-3}$
$p_9 = -0.204813$	-0.218986	$-0.202004 \cdot 10^{-4}$
$p_{10} = 6.63267 \cdot 10^{-4}$	$8.69283 \cdot 10^{-4}$	$1.17942 \cdot 10^{-3}$

to other stopping materials than those used for the fit. This factor can be obtained from the following relations:

$$
\begin{aligned}
0 < Z_t \leq 5: &\quad k = A_t/9.012 \cdot (4/Z_t)^{0.98} \\
5 < Z_t \leq 9: &\quad k = A_t/12.011 \cdot (6/Z_t)^{0.98} \\
9 < Z_t \leq 32: &\quad k = A_t/26.982 \cdot (13/Z_t)^{0.90} \\
32 < Z_t \leq 64: &\quad k = A_t/118.69 \cdot (50/Z_t)^{0.88} \\
64 < Z_t \leq 72: &\quad k = A_t/180.95 \cdot (73/Z_t)^{0.88} \\
72 < Z_t \leq 92: &\quad k = A_t/207.20 \cdot (82/Z_t)^{0.80}
\end{aligned}
$$

where A_t and Z_t represent the mass and the atomic numbers of the stopping material, respectively. When the stopping material is a mixture of different isotopes, the mean mass number has to be used for A_t.

A more accurate determination of the range can be obtained by applying the correction factor F_{corr} to the equation A.3:

$$
r(Z_p, A_p, E/A_p) = k \frac{A_p}{Z_p^2} 10^{\kappa} \cdot F_{corr} \qquad mg/cm^2 \tag{A.5}
$$

with

$$F_{corr} = 1/(0.965735686 + 9.79114E-03 \cdot R + 3.17099E-03 \cdot R^2 \\ -6.71227E-04 \cdot R^3 + 2.28409E-05 \cdot R^4) \tag{A.6}$$

where $R = Z_p^2/1000$

This analytical range-energy relation (A.5) can be inverted according to the following equation:

$$E(Z_p, A_p, r) = 10^{\frac{-(p_7+p_8 Z_p)}{2(p_9+p_{10} Z_p)}} - \sqrt{\left(\frac{(p_7+p_8 Z_p)}{2(p_9+p_{10} Z_p)}\right)^2 - \frac{p_5+p_6 Z_p}{p_9+p_{10} Z_p}} \\ + \frac{log_{10}(\frac{r/F_{corr}}{kZ^2/A})}{(1+p_1 Z_p + p_2 Z_p^2 + p_3 Z_p^3 + p_4 Z_p^4)(p_9+p_{10} Z_p)} \tag{A.7}$$

Expressions A.5 and A.7 allow us to calculate analytically the range and energy of any ion traversing any stopping material, and together with equations A.1 and A.2 we can determine their energy loss. Therefore, these analytical range-energy relations constitute a very fast algorithm for energy-loss calculations, well suited for technical applications.

The analytical range-energy relations provide another important advantage: The fact that the functions A.5 and A.7 are the exact inverse functions of each other avoids systematical inconsistencies which could occur if tabulated range values are interpolated.

Appendix B

Energy Losses Tables

Experimental measured data for several projectile-target combinations. Light and heavy projectiles passing trough light and heavy targets data were measured. Several energies are also printed. The same projectile-target combinations were simulated with all the codes under study in order to compare the results.

Projectile(MeV/u)	Target	Data	AMADEUS	ATIMA	GEANT	SIRM
^{197}Au(115.3)	Be	30.34(1.0)	-2.6	-2.5	11.9	1.7
(257.7)	Be	19.54(0.7)	-0.2	-0.3	0.0	-1.4
(117.0)	Al	29.56(1.0)	-4.7	-4.7	7.6	-0.9
(255.7)	Al	19.49(0.7)	-1.9	-2.2	-2.5	-3.9
(286.7)	Al	18.36(3.3)	-1.3	-1.6	-2.6	-4.0
(110.9)	Cu	25.56(1.3)	-1.3	-2.5	10.54	0.4
(263.4)	Cu	16.62(1.1)	-1.6	-1.5	-2.7	-4.6
(117.6)	Pb	18.11(1.3)	-2.1	-0.5	11.4	2.1
(255.5)	Pb	12.75(0.9)	-1.1	-0.9	-2.1	-4.1
^{208}Pb(130.7)	Be	30.35(1.0)	-2.7	-2.5	8.6	1.0
(201.8)	Be	23.79(0.5)	-1.2	-0.7	2.8	-0.0
(120.4)	Al	31.02(0.6)	-4.8	-4.4	8.0	-0.7
(202.6)	Al	23.45(0.6)	-3.3	-2.4	0.5	-2.4
(193.3)	Cu	20.64(0.6)	-1.3	-1.6	1.3	-2.7
(132.2)	Ta	19.12(1.3)	-2.1	-0.3	9.3	1.0
(201.8)	Ta	15.56(0.6)	-1.0	0.8	2.6	-1.0

Table B.1: Comparison between codes and experimental data [22] The values of different codes are showed as relative values to the experimental data in percent.

Projectile(MeV/u)	Target	Data	AMADEUS	ATIMA	GEANT	SIRM
^{209}Bi(168.8)	Be	26.84(0.8)	-1.9	-1.4	5.5	0.4
264.0	Be	21.27(1.2)	0.2	-0.4	0.2	-1.6
525.1	Be	15.81(0.8)	1.8	0.4	-4.4	-4.8
879.6	Be	13.73(0.6)	0.4	-0.4	-7.0	-7.4
157	Al	27.41(3.5)	-3.6	-3.2	-3.8	-1.4
162.8	Al	27.03(0.7)	-2.6	-3.6	3.1	-2.0
171.0	Al	26.04(2.5)	-0.5	-2.3	4.0	-1.1
183.0	Al	25.01(2.5)	-2.2	-1.6	3.6	-1.0
269.6	Al	21.18(1.5)	-3.3	-3.4	-3.6	-5.4
498.6	Al	16.42(0.5)	-2.0	-2.9	-8.6	-8.4
866.7	Al	13.78(0.5)	-1.4	-0.6	-8.6	-9.0
163.3	Cu	22.82(0.9)	-1.1	-1.3	4.6	-1.1
258.8	Cu	18.38(1.1)	-1.1	-1.2	-2.0	-4.2
495.2	Cu	14.36(0.6)	-1.0	-2.5	-8.8	-8.8
874.7	Cu	12.17(0.6)	-2.1	-1.6	-9.7	-10.0
185.6	Ta	16.67(1.1)	-1.0	0.0	3.7	-1.3
166.5	Ag	20.39(0.9)	-3.7	-1.0	4.4	-1.3
261.6	Ag	16.58(1.2)	-3.0	-1.1	-2.2	-4.5
500.1	Ag	12.81(0.5)	-0.5	-0.6	-7.4	-7.3
873.4	Ag	11.11(0.5)	-0.9	-0.8	-9.6	-9.9
165.8	Au	17.25(0.8)	-0.6	-0.5	4.9	-0.8
260.4	Au	14.12(1.1)	0.6	-0.5	-1.8	-4.0
492.3	Au	11.03(0.5)	2.3	0.3	-7.0	-6.7
851.6	Au	9.66(0.4)	-0.5	-0.4	-9.7	-9.7
186.4	Pb	16.12(1.2)	-1.5	-1.0	3.0	-2.0

Table B.2: Comparison between codes and experimental data [22]. The values of different codes are showed as relative values to the experimental data in percent.

Projectile(MeV/u)	Target	Data	AMADEUS	ATIMA	GEANT	SIRM
$^{18}O(690)$	Be	0.125(1.6)	0.0	0.8	1.6	1.6
	C	0.138(2.9)	0.7	0.0	1.4	1.4
	Al	0.123(3.2)	0.0	0.8	1.6	0.8
$^{40}Ar(985)$	Be	0.587(2.7)	-0.5	1.2	0.7	0.7
	C	0.640(2.9)	-0.5	0.1	0.2	0.2
	Al	0.584(3.2)	-2.6	-0.5	-1.8	-1.7
	Cu	0.494(3.2)	0.6	2.2	1.6	1.6
	Pb	0.389(3.1)	0.0	1.5	0.7	0.7
$^{58}Ni(260)$	Be	2.477(2.5)	-2.3	-0.5	-1.4	-1.1
(430)	Be	1.904(2.0)	0.3	-0.3	-1.4	-1.5
$^{86}Kr(420)$	Be	3.206(1.5)	0.5	-0.5	-2.2	-2.2
(900)	Be	2.432(1.5)	0.7	0.2	-1.8	-2.2
$^{136}Xe(780)$	Be	5.861(1.3)	0.3	-0.9	-4.9	-5.1
	C	6.524(1.3)	-0.4	-2.3	-5.9	-6.1
	Al	5.806(2.1)	-0.3	-0.8	-5.8	-5.8
	Cu	5.077(1.3)	0.3	-0.8	-5.9	-6.0
	Pb	3.959(1.6)	0.0	-0.5	-6.4	-6.2
$^{197}Au(950)$	Be	12.124(1.0)	0.0	0.2	-6.5	-6.7
	C	13.256(1.2)	1.0	0.6	-5.8	-6.0
	Al	12.086(1.3)	-0.5	0.4	-7.8	-7.8
	Cu	10.572(1.2)	-0.6	0.5	-7.6	-7.9
	Pb	8.332(1.2)	-1.6	0.8	-8.6	-8.8
$^{209}Bi(157)$	Al	27.406(3.5)	-3.6	-3.2	-3.8	-1.4
$^{238}U(900)$	Be	16.648(1.1)	1.1	1.1	-6.3	-6.7
	C	18.470(1.5)	0.7	0.1	-6.9	-7.4
	Al	16.739(1.0)	-0.2	0.5	-8.4	-8.7
	Ti	15.739(1.5)	-1.9	0.4	-8.6	-8.8
	Cu	14.703(1.1)	-0.8	0.4	-8.7	-9.1
	Au	11.728(1.5)	1.4	0.8	-9.6	-9.6
	Pb	1.533(1.8)	0.7	1.1	-9.4	-9.7

Table B.3: Comparison between codes and experimental data [**?**] The values of different codes are showed as relative values to the experimental data in percent.

Appendix C

Deduction of the geometrical factor Γ.

We will derive the geometrical factor in expression 3.6.

From 3.1 is easy to get

$$\Delta\beta = \frac{1}{n_1 cos^2\theta} sin\theta\Delta\theta \Longrightarrow \Delta\beta = \beta tan\theta\Delta\theta \Longrightarrow \Delta\beta = tan\theta\Delta\theta \tag{C.1}$$

that is equation 3.5

Using Snellius Law we have:

$$n_1 sin\theta = n_2 sin\varphi \Longrightarrow n_1 cos\theta\Delta\theta = n_2 cos\varphi\Delta\varphi \Longrightarrow \Delta\theta = \frac{n_2}{n_1} tan\theta \frac{cos\varphi}{cos\theta}\Delta\varphi \tag{C.2}$$

Then, we can rewrite expresion C.1 as

$$\Delta\beta = \frac{n_2}{n_1} tan\theta \frac{cos\varphi}{cos\theta}\Delta\varphi \tag{C.3}$$

Looking at the figure 3.2 we can see

$$tan\varphi = \frac{R}{L} \Longrightarrow \frac{cos^2\varphi + sin^2\varphi}{cos^2\varphi}\Delta\varphi = \frac{\Delta R}{L} \Longrightarrow \Delta\varphi = \frac{\Delta R}{L}\frac{1}{1 + tan^2\varphi} \tag{C.4}$$

Substituting this into C.3, manipulating,using again the Snellius Law and weigthing the result with the number of detected photoelectrons we obtain, finally

$$\frac{\Delta\beta}{\beta} = \frac{1}{\sqrt{N}} \frac{\Delta R}{R} \frac{tan^2\theta}{1 + tan^2\varphi} \tag{C.5}$$

From here, we conclude that the geometrical factor Γ is given by:

$$\Gamma = \frac{tan^2\theta}{1 + tan^2\varphi} \tag{C.6}$$

Appendix D

Simulation of Cerenkov photons with GEANT 3.21

When a charged particle cross a dielectric medium with a velocity higher than the group velocity of light in the material GEANT code call to the GGCKOV routine which generates a number of Cerenkov photons according to the Frank-Tamm relation (equation 3.2) whenever the user had defined the dielectric medium as a radiator by calling the routine GSCKOV. This photons are stored in the JSTAK stack for further tracking. To define a dielectric medium as a radiator, the user has to provide the refractive index and the radiation length of the material as a function of the wavelength.

The generated Cerenkov photons are tracked in the routine GTCKOV. The photons to be tracked are defined by two vectors, the photon momentum ($\vec{p} = \hbar\vec{k}$) and the photon polarisation ($\vec{e}$). By convention the direction of the polarisation vector is that of the electric field. The photon is tracked taking into account processes as *in flight* absortion or *boundary action*. Whenever a photon reaches a medium boundary, the behaviour of the photon at the surface boundary is determined by three quantities:

- Refraction or reflection angle, this represents the kinematic of the effect.
- Amplitude of the reflected and refracted waves, this is the dynamic of the effect.
- Probability of the photon to be refracted or reflected, this is the quantum mechanical effect which we have to take into account if we want to describe the photon as a particle and not as a wave.

GEANT distinguish between three kinds of boundary action, dielectric-black material, dielectric-metal and dielectric-dielectric. The first case is trivial in the sense that the photon is inmediately absorbed. The second case is also simple because the photon can not be transmitted, so the probability for the photon to be absorbed is estimated and, if the photon is not absorbed, then is reflected. The remaining case is more complicated and is extensively described in the GEANT Manual[3], section PHYS260.

In our simulation, the photons are tracked untill they reach the detection plane defined by the user. During the tracking, the photon absortion probabilities calculated by GEANT have been desactivated and new absortion probabilities have to be introduced by the user because the default values given by GEANT were not in good agreement with those measured in the Munich Technical University [41].

Appendix E

Velocity determination in total internal reflection mode.

We will derive here the expression which allow us to determine the velocity of the particle passing through the radiator from the direct measurement of the ring radius in total reflexion mode. In the total reflexion mode we can determine directly the Cerenkov emission angle.

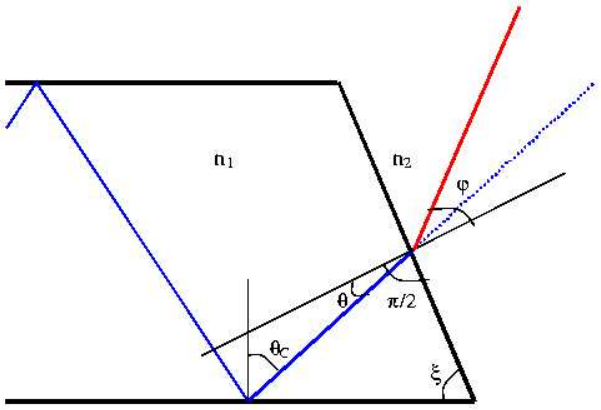

Figure E.1:

This will be a pure geometrical problem. Looking at figure E.1 we have find a relation between Cerenkov angle θ_C and the angle ξ, which is determined by the radiator radii:

$$\xi + \left(\frac{\pi}{2} - \theta\right) + \left(\frac{\pi}{2} - \theta_C\right) = \pi \tag{E.1}$$

then:

$$\theta_C = \xi - \theta \tag{E.2}$$

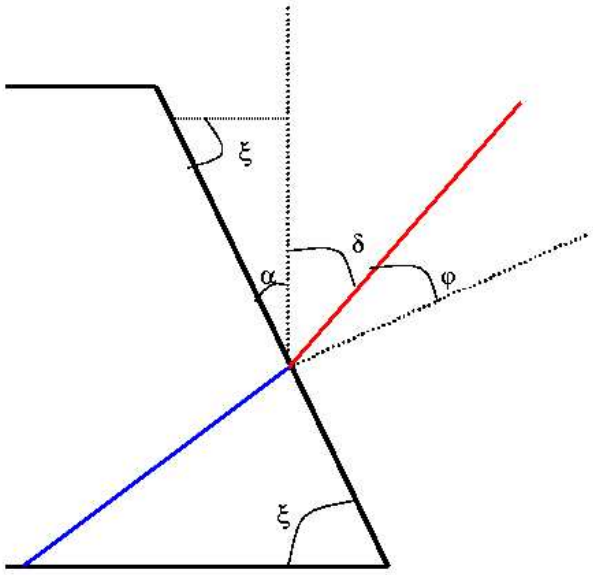

Figure E.2:

Additionally, the different refractive index of the radiator and the gap expansion medium induce the refraction of the photon at the boundary. Looking at figure E.2 we can find an expression which relates the refracted angle ϕ with the angle fixed by the radiator shape ξ:

$$\frac{\pi}{2} + \xi + \alpha = \pi \Longrightarrow \alpha = \frac{\pi}{2} - \xi \tag{E.3}$$

the remaining angles follow the relationship:

$$\alpha + \phi + \delta = \frac{\pi}{2} \Longrightarrow \phi = \xi - \delta \tag{E.4}$$

We are already close to the solution because the angle δ in fig F.2 is the one we measure from the raing radii, as it is shown in the figure E.3. From this, we can derive:

$$\delta = \arctan\left(\frac{R-\bar{r}}{L}\right) \tag{E.5}$$

$$\xi = \arctan\left(\frac{d}{r_1 - r_2}\right) \tag{E.6}$$

where R is the ring radius, $\bar{r}$ is the mean radiator radius, L is the distance from the radiator to the detector, r_1 and r_2 are the bottom and top radii of the radiator, respectively, and d is its thickness.

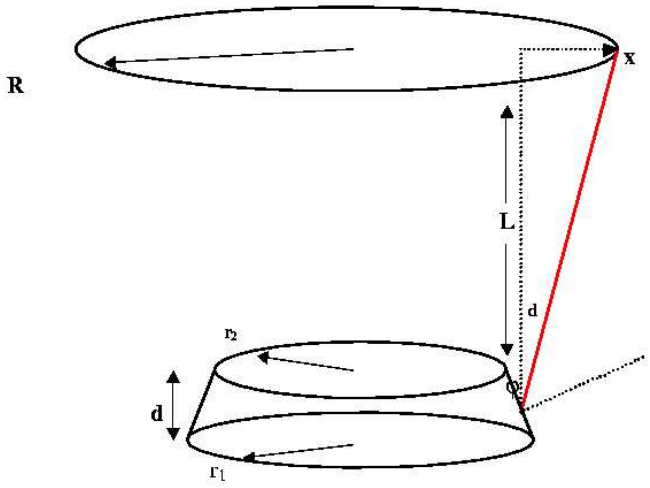

Figure E.3:

From this expression we can give the ϕ angle (expression E.4) as follows:

$$\phi = \arctan\left(\frac{d}{r_1 - r_2}\right) - \arctan\left(\frac{R-\bar{r}}{L}\right) \tag{E.7}$$

Finally, making use of the Snellius law we obtain:

$$\theta = \arcsin\left[\frac{n_2}{n_1}\sin\phi\right] \tag{E.8}$$

being n_1 and n_2 the refractive index of the radiator and the expansion gap medium respectively.

The reader must notice that this θ angle is not the Cerenkov angle, but the incident angle to the normal of the radiator boundary. Remembering the realationship between this angle and the Cerenkov angle (expression E.2) we can finally deduce the following expression for the Cerenkov angle:

$$\theta_C = \arctan\left(\frac{d}{r_1 - r_2}\right) - \arcsin\left[\frac{n_2}{n_1}\left(\sin\left[\arctan\left(\frac{d}{r_1 - r_2}\right) - \arctan\left(\frac{R - \bar{r}}{L}\right)\right]\right)\right] \tag{E.9}$$

In the same way than in the second chapter, we have to make the assumption that the photon is emited in the middle of the radiator. The distande L from the radiator to the detector has to be taken from the radiator half height.

Bibliography

[1] M.Pfützner, H.Geissel, G.Münzenberg, F.Nickel, Ch.Scheidenberger, K.-H-Schmidt, K.Sümmerer, T.Brohm, B.Voss and H.Bichsel, Nucl. Instr. and Methods B 86 (1994) 213-218.

[2] Th.Blaich, Th.W.Elze, H.Emling, K.Grimm, W.Henning, R.Holzmann, G.Ickert, J.G.Keller, H.Klingler, W.Kneissl, R.König, R.Kulessa, J.V.Kratz, D.Lambrecht, J.S.Lange, Y.Leifels, E.Lubkiewicz, M.Proft, W.Prokopowicz, C.Schütter, R.Schmidt, H.Spies, K.Stelzer, J.Stroth, W.Walus, E.Wajda, H.J.Wollersheim, M.Zinser, E.Zude, Nucl. Instr. and Methods A 314 (1992) 136-154.

[3] GEANT 3.21 Manual - Detector Description and Simulation Tool. CERN, Geneve (1993).

[4] http://www-aix.gsi.de/scheid/ATIMA1.html

[5] http://www.research.ibm.com/ionbeams/

[6] J.F.Ziegler, J.P.Biersack and U.Littmark, Pergamon Press, New York (1996).

[7] K.-H. Schmidt, E. Hanelt, H. Geissel, G. Muenzenberg, J.-P. Dufour, Nucl. Instrum. and Methods A260 (1987) 287-303.

[8] S.P.Ahlen, Rev. Mod. Phys., 52, 121, 1980.

[9] Linhard and Sorensen, Phys. Rev. A53, 4 (1996) 2443.

[10] Hans Bethe, Annalen der Physik, 5, 325, 1930.

[11] U.Fano, Ann. Rev. of Nuclear Science, 13, 1, 1963.

[12] S.P.Ahlen, Phys. Rev. A, 25, 1856, 1982.

[13] T.E.Pierce and M.Blann, Phys. Rev. 173, 390, 1968.

[14] W.H.Barkas and M.J.Berger, Natl. Acad. of Science, NRC1133, 1964.

[15] E.Fermi, Phys. Rev. 57 (1940) 485.

[16] N.F.Mott, Proc. Roy. Soc. London A 124 (1929) 425.

[17] N.F.Mott, Proc. Roy. Soc. London A 135 (1932) 429.

[18] F.Bloch, Ann. Phys. (Leipzig) 16, 285, 1933.

[19] C.Scheidenberger, H.Geissel, H.H.Mikkelsen, F.Nickel, T.Brohm, H.Folger, H.Irnich, A.Magel, M.F.Mohar, G.Münzenberg, M.Pfützner, E.Roeckl, I.Schall, D.Schardt, K.-H.Schmidt, W.Schwab, M.Steiner, Th.Stöhlker, K.Sümmerer, D.J.Vieira, B.Voss and M.Weber. *Phys. Rev. Lett.* 73 (1994) 50.

[20] H.H.Andersen and J.F.Ziegler, Hydrogen stopping powers and ranges in all elements. Pergamon Press, 1977.

[21] K.-H.Schmidt, E.Hanelt, H.Geissel, G.Münzenberg, J.-P-Dufour, Nucl. Instr. and Methods A 260 (1987) 287.

[22] Helmut Weick Thesis.

[23] C.Scheidenberger et al. Phys. Rev. Lett. 77 (1996) 3987

[24] H.Geissel and C.Scheidenberger, Nucl. Instr. and Meth. B 136 (1998) 114.

[25] C.Scheidenberger and H.Geissel, Nucl. Instr. and Meth. B 135 (1998) 25.

[26] N.Bohr, Dan. Mat. Fys. Medd. 18 (8) (1948)

[27] M.S.Livingston, H.A.Bethe, Rev. Mod. Phys. 9 (1937) 245.

[28] B.Rossi, *High Energy Particles*, Prentice-Hall Inc., Englewood Cliffs, NJ, 1952.

[29] L.Landau, J. Phys (USSR) 8, 201 (1944).

[30] P.V.Vavilov, Sov.Phys. JETP 5, 749 (1957).

[31] E.Hanelt, PhD. Thesis, Institut fur Kernphysik, TH Darmstadt, 1992

[32] W.T.Scott, Rev. Mod. Phys. 35, 231 (1963).

[33] V.Highland, Nucl. Instrum. and Methods A, 129(1975) 497 and Nucl.Instrum.Methods 161, 171 (1979).

[34] N.Iwasa, H.Geissel, G.Münzenberg, C.Scheidenberger, Th.Schwab, H.Wollnik, Nucl. Instr. and Meth. B, 126 (1997) 284-289.

[35] L.Mallet, Compte Rendu 188 (1929) 445.

[36] G.R.Lynch and O.I.Dahl, Nucl. Instrum. and Methods B58, 6 (1991).

[37] P.J.Karol, Phys. Rev. C 11 (1975) 1203.

[38] T.Brohm, K.-H. Schmidt, Nucl. Phys. A 569 (1994) 821

[39] Th.Rubehn et al., Z. Phys. A 353 (1995) 197

[40] K.-H.Schmidt et al., Nucl. Phys. A 665 (2000) 221.

[41] R.Gernhäuser et al., Nucl. Instr. and Methods A 433 (1999) 217-221.

[42] J.Seguinot and T.Ypsilantis, Nucl. Instr. and Methods 142 (1977) 377.

[43] G.Poelz and R.Reithmuller, Nucl. Instr. and Methods 195 (1982) 491.

[44] http://r.home.cern.ch/r/richrd26/www/hmpid/richsim.html

[45] M.J.Tobar-Vidal Thesis, University of Santiago de Compostela, 1999.

[46] H.Snell, Nuclear Instruments and Their Uses. John Wiley and Sons, 1962..

[47] T.Ypsilantis, J.Seguinot, Nucl. Instr. and Methods A 343 (1994) 1-30.

[48] R,Gernhäuser PhD Thesis, Technische Universität München, March 1998.

[49] K.-H.Schmidt, S.Steinhäuser, C.Böckstiegel,A.Grewe, A.Heinz,A.R.Junghans, J.Benlliure, H.-G.Clerc, M.DeJong, J.Müeller, M.Pfützner, B.Voss, Nucl. Phys. A 665 (2000) 221-267.

[50] B.D.Wilkins, E.P.Steinberg, R.R.Chasman, Phys. Rev. C14 (1976) 1832.

[51] C.Böckstiegel, S.Steinhäuser, J.Benlliure, H.-G.Clerc, A.Grewe, A.Heinz, M.DeJong, A.R.Junghans, J.Müeller, K.-H.Schmidt, Phys. Lett.B 398 (1997) 259.

[52] T.Enqvist, W.Wlazlo, P.Armbruster, J.Benlliure, M.Bernas, A.Boudard, S.Czajkowski, R.Legrain, S.Leray, B.Mustapha, M.Pravikoff, F.Rejmund, K.-H.Schmidt, C.Stephan, J.Taieb, L.Tassan-Got, C.Volant, Nucl. Phys. A 686 (2001) 481-524.

[53] D.J.Morrisey, Phys. Rev. C 39 2 (1989) 460.